Long, High-Gradient Magnetic Atom Guide and Progress Towards an Atom Laser

by

Spencer E. Olson

A dissertation submitted in partial fulfillment
of the requirements for the degree of
Doctor of Philosophy
(Physics)
in The University of Michigan
2006

Doctoral Committee:

Professor Georg A. Raithel, Chair
Professor Christopher R. Monroe
Professor J. Keith Riles
Assistant Professor Luming Duan
Assistant Professor Andrew J. Christlieb

This work is dedicated to Renée, Wesley, Micah, and Tobias.

ACKNOWLEDGEMENTS

I would like to acknowledge the many people who have supported me and given me encouragement for this work. First, I would like to thank Georg Raithel for his patience, wisdom, and the funding that he provided for me throughout the duration of my research at the University of Michigan. I would like to thank Kevin Teo and Jeff Guest for the mentoring they gave and the expertise that they both shared with me early on in my work. Jeff has been and continues to be a valued friend and mentor. It has been a pleasure to have worked with several of the members of Georg's research group: Jeffrey Guest, Kevin Teo, David Feldbaum, Alisa Walz-Flannigan, Natalya Morrow, Tara Cubel, Jae-Hoon Choi, Rui Zhang, Aaron Reinhard, Brenton Knuffman, and Rachel Sapiro. I would specifically like to thank Rahul for the large role which he played in the project on which I worked. Much of the success and achievement of this project would not have been possible without his effort, dedication, and partnership.

Andrew Christlieb has provided much insight and direction with the simulations of the evaporative process. I also want to thank him for his friendship and encouragement for my career goals. I also want to thank Quanhua Sun for computational results against which my own simulations were validated.

Thanks also to Michael Busha and Gus Evrard for the much appreciated use of the Opus cluster. Also many thanks to Lynn Zhang for the many many hours of CPU time on the LSA Obsidian cluster.

Lastly and most significantly, I want to thank Renée for the encouragement, constant love and support she has given me through these past several years. She has done an incredible job with the nearly impossible task of reigning our young stripling boys towards good.

This work was supported by the Army Research Office (ARO) and the Office of Naval Research (ONR), the Chemical Sciences, Geosciences, and Biosciences Division of the Office of Basic Energy Sciences, Office of Science, U.S. Department of Energy, the National Science Foundation, the Michigan Center for Theoretical Physics (MCTP), the Office of Air Force Research (OAFR), and the National Science Foundation center for Frontiers in Optical Coherent and Ultrafast Science (FOCUS).

TABLE OF CONTENTS

LIST OF TABLES

Table

LIST OF FIGURES

Figure

LIST OF APPENDICES

Appendix

ABSTRACT

The continuous injection and propagation of a cold atomic beam in a 1.7 m long high-gradient (up to 2.7 kG/cm) magnetic guide is demonstrated. Continuous injection is accomplished by side-loading a magnetic guide with atoms from a sequence of two modified magneto-optical traps. In the high-gradient portion of the guide, the guided atomic beam has a transverse temperature of 420 μK ± 40 μK, a longitudinal temperature of 1 mK, and an average velocity of order 1 m/s.

Essential for the characterization of this steady-state atomic beam, imaging methods compatible with the high field-gradients associated with this magnetic guide have been investigated and developed. By utilizing a probe laser tuned to an open transition, the fluorescence yield per atom is largely fixed throughout the trap volume, independent of the trapping field. This enables a reliable conversion of fluorescence images into atomic-density profiles.

Using a fixed radio-frequency (ν_{rf}) current coupled directly onto the guide wires, continuous and selective removal of atoms with a transverse energy exceeding $h\nu_{\mathrm{rf}}$ is demonstrated. This removal scheme is the essence of an rf filter, where the number of modes occupied by the atomic flow is reduced. Through sufficient rf-filtering, a near-single-mode guided atomic beam should be achievable, enabling basic atom-interferometric experiments. The extension of this fixed-frequency removal of atoms for continuous position-resolved evaporative cooling in a long magnetic guide is outlined.

Employing an innovative gridless technique for performing Direct Simulation of rarefied gas dynamics via Monte Carlo (DSMC), the evaporative cooling process in a guided atomic beam has been simulated. Both fixed-frequency as well as variable-frequency evaporative cooling layouts have been explored and the results of these simulations are presented. The implementation of this gridless technique is presented and its benefits are briefly outlined.

In parallel with the development of a continuous-wave atom laser, tools suited to manipulate cold atomic beams in atom guides have been explored. An atomic guide with a tunable aspect ratio, using rf-dressed state potentials, is presented.

CHAPTER I

Introduction

One of the greatest success stories of atomic physics has been the modern development and implementation of laser cooling and trapping. Developed first for ions [1, 2], this has now been extended to neutral atoms [3] and is being extended to molecular [4, 5] systems. Because cold particles exhibit enhanced quantum properties, cold particles lend themselves well to applications where quantum mechanics is required. Hand in hand with the good amount of funding and opportunities [1] that the success of cold particle physics has provided to atomic and chemical physicists, a large number of practical applications has been envisioned and proposed. These practical applications include quantum computing architectures as well as sensory instrumentation.

Because of the small de Broglie wavelength of atoms, it is envisioned that useful atom interferometric devices could be implemented. The sensitivity associated with atomic interferometers is orders of magnitude greater than that of analogous optical interferometers (using optical lasers currently available). In addition, because atoms have mass, atom interferometric devices would enable measurements to study the terrestrial environment which have never before been possible. In terms of practical

---

[1] Even though there has been a distressing trend to decrease the funding in atomic physics in the past few years in the U.S., there have been many good years, and we hope for better in the future.

use, there are several key milestones that are currently being planned. One of these would be the impressive mapping of the Earth's local gravitational field. Such a tool would enable geophysicists to study plate-tectonics, sub-subterranean observations, and other phenomena in a way never before imagined. Instead of needing to drill, take core samples, or observing sound waves, a new type of in situ/vivo (so to say) measurement would be possible. [2]

The work described in this thesis concerns the guiding of cold atomic beams, which is foundational to the development of atom interferometric devices. This, the first chapter, will concern itself with the general motivation of developing a cold atomic beam in a high-gradient magnetic guide as well as basic concepts needed for discussions in the later chapters. The atom laser will be first discussed with reference to the optical laser, following which the conversion of the time-sequential process of a pulsed atom laser into a space-sequential process of a purely continuous-wave (cw) atom laser will be outlined. After the development of the atom laser discussion, concepts for important experimental components will be introduced, including the magneto-optical trap (MOT), the low-velocity-intense source (LVIS), magnetic guiding, and lastly evaporative cooling.

1.1 Bose-Einstein Condensate and the Atom Laser

One of the most exciting experimental results of the last decade has been the realization of the Bose-Einstein condensate (BEC) [6–8]. As a macroscopic occupation of a single quantum state by a system of particles, BEC has offered avenues for new insight into the quantum mechanical world. Though Fermionic particles are forbidden to occupy the same state, Bosonic particles may indeed collect in a com-

---

[2] I will not delve into more diverse purposes for wanting to measure local fluctuations of gravity, due to things such as underground bunkers, um. . . oil beds, um. . . subterranean geological structures.

mon state. The basic requirement for BEC is that the wavefunctions of the Bosonic particles begin to overlap. This occurs when $n\lambda_{\mathrm{th}}^3$ becomes of order 1, where n is the local number density and λ_{th} is the thermal de Broglie wavelength. λ_{th} is given by

$$\lambda_{\mathrm{th}} = \sqrt{\frac{2\pi\hbar^2}{Mk_{\mathrm{B}}T}} \tag{1.1}$$

where m is the mass, k_{B} is the Boltzmann constant, and T is the temperature of the ensemble. For specific trap geometries (or lack thereof) the phase-space condition can be calculated exactly:

$$\begin{aligned} n{\lambda_{\mathrm{th}}}^3 &\geq 2.612 \qquad \text{(free space)}, \\ n{\lambda_{\mathrm{th}}}^3 &\geq 1.202 \qquad (3\!-\!\text{D harmonic trap})\,. \end{aligned} \tag{1.2}$$

Even before its realization, BEC inspired interest in the development of what is currently known as an "atom laser". To paraphrase Wolfgang Ketterle [9], although the phrase atom laser is a misnomer (because the word laser is actually an acronym that refers to light and not atoms) and although there have been many attempts to create a new name (Boser [10], baser, beamer, CSAASSA [3] , etc. [4]) a more appropriate name will not become commonly used until the atom laser sees more common use. The same observation was also true of the (optical) laser, which was formerly known as the optical maser (maser being the acronym for microwave amplification of stimulated emission of radiation). Like the (optical) laser, the atom laser will not receive more common usage until the development of a continuous-wave atom laser. While the prefix optical, when referring to a laser, is not necessary, for the sake of this thesis, this prefix will be used to avoid confusion with the misnomered atom

---

[3] Suggested by Dan Kleppner, "CSAASSA" means coherent state atom amplification by stimulated scattering of atoms. [11]

[4] My favorite would be "phaser", reminiscent of the Star Trek years. Please insert your own meaning for the acronym.

	Optical Laser	Atom Laser
Quanta	Photons	Atoms
Cavity	Mirrors	Magnetic/Optical Traps (not magneto-optical)
Gain	Stimulated emission	Stimulated scattering into ground state

Table 1.1: Comparison between components of an optical laser and an atom laser.

laser. The remainder of this section defines the atom laser by analogy to the optical laser.

Loosely speaking, a laser is a source of coherent particle-waves, created by output-coupling a storage of stimulated build-up of the occupation of a resonant cavity mode. For a simple optical laser, the photon plays the part of the output particle-wave and laser-cavity quanta, mirrors form the resonant cavity, and gain is provided by stimulated emission into the resonant laser cavity (see Table 1.1). As the matter-analogy of an optical laser, an atom laser provides output in the form of a matter-wave. In this case, the quanta of the system are atoms, and the cavity is created by an atom trap (magnetic or optical). Table 1.1 tabulates these comparisons.

1.1.1 Build-up by Stimulated Scattering

To understand the atom-laser pump mechanism, it is helpful to consider a three-level system, as shown in Fig. 1.1, where level three is above an evaporation threshold, such that any level-three atoms are immediately removed from the system. As indicated, two atoms in state 2 might collide, such that one atom is shifted into the ground state and the other atom is shifted into state 3. This provides for population to accumulate into the ground state. This process is irreversible because the level 3 atoms are immediately removed from the system. Analogous to the optical laser, there are two mechanisms for atoms to be transferred via this collision process into the atom laser cavity mode (i.e. BEC). The first of these, random or spontaneous

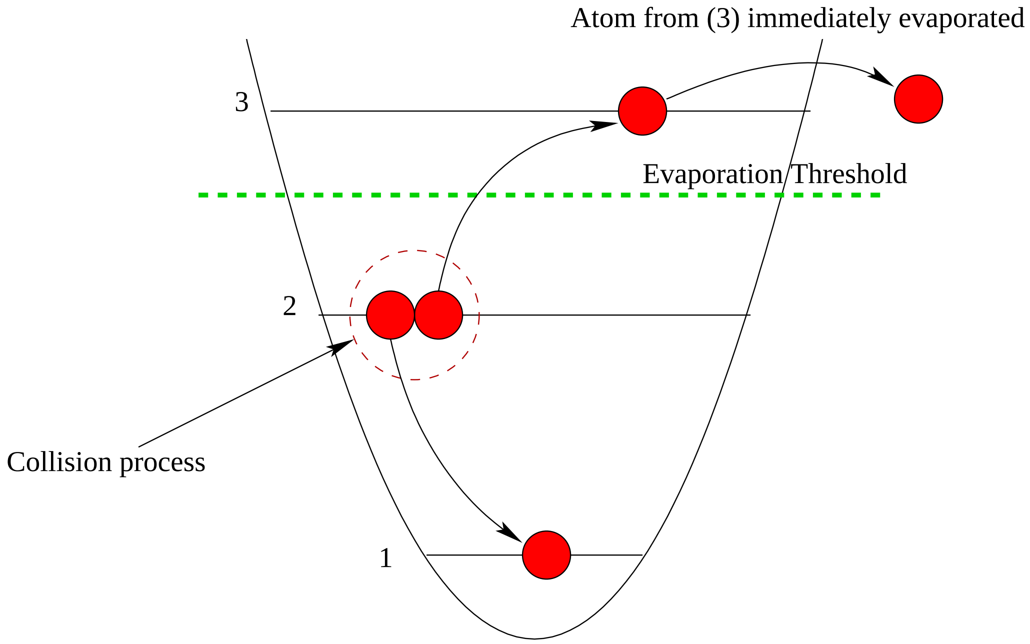

Figure 1.1: Simplified model of ground-state populating collisions. Shown explicitly here is the random scattering of an atom into the ground state. This is known as spontaneous scattering. Though it can result in atoms entering the ground state, it does not tend to dramatically increase the ground-state population. Once the BEC begins to form, the cross-section of the scattering type shown here is enhanced and the BEC grows more rapidly.

scattering, will not tend to dramatically increase the BEC population, whereas the second, or stimulated scattering, will tend to dramatically increase the BEC population.

Under the assumption that the thermal component (i.e. collection of non-BEC particles in the lower lying excited states) in the trap is not yet depleted, Gardiner et al. [10] showed that the rate of change of BEC population $\mathcal{N}$ could be approximated by

$$\dot{\mathcal{N}} = \sqrt{2}\,\gamma_{\text{coll}}\,C\left(\mathcal{N}\right)\left\{\left(1-\exp\left[\frac{\mu_{\mathcal{N}}-\mu_{\text{th}}}{k_{\text{B}}T}\right]\right)\mathcal{N}+1\right\} \tag{1.3}$$

where γ_{coll} is the elastic collision rate and $\mu_{\mathcal{N}}$ and μ_{th} are the chemical potentials of the BEC and thermal component respectively. $C\left(\mathcal{N}\right)$ is weakly dependent on $\mathcal{N}$

and for $\{\mu_{\mathrm{th}}, \mu_{\mathcal{N}}\} \ll k_{\mathrm{B}}T$ can be approximated by

$$\begin{aligned} C(\mathcal{N}) &\approx \zeta(3/2)\sqrt{2} \\ &= 2.612\,\sqrt{2} \end{aligned} \tag{1.4}$$

where $\zeta(t)$ is the Riemann zeta function. (See also [12].) The second term in Eq. 1.3 (+1) corresponds to spontaneous scattering while the first term corresponds to stimulated scattering. Examining this first term, we see that when the chemical potentials of the BEC and the thermal components differ, there is effectively an enhanced scattering rate.

1.1.2 Output Coupling

For the simple optical laser, the output is created by allowing photons to tunnel through one of the mirrors in the cavity. Likewise, BEC atoms coupled to the outside of a trap can provide the atom laser beam. There are several different mechanisms that can be used to output-couple BEC atoms from the trap. These include, but are not limited to, weak microwave coupling of trapped to untrapped states [13, 14], stimulated Raman transfer [15], as well as coherent tunneling through a trap barrier (this will be discussed briefly in Ch. II).

1.1.3 Differences and the Real Motivation

While there are many similarities between the two laser analogs, there are clear differences. The foremost among these are that atoms have mass and charge, whereas photons are massless and chargeless. Atoms are thus susceptible to accelerations produced by gravitational-, rotational-, electric-, and magnetic-fields. A tool that generates coherent matter waves thus opens up a whole genre of experimental studies and applications: gravitometry, precision navigation, and generic field-sensing (magnetic, electric, and other acceleration fields).

Another clear difference between photons and atoms is that atoms can interact with each other, whereas photons do not. In terms of an atom laser, this means that while optical lasers can easily propagate through gaseous media (the air), atom lasers will not (i.e. you will not be shooting anyone with these). Furthermore, the atoms within the atom-lasing beam interact with each other producing effects that are commonly treated using field-theory techniques.

1.1.4 Pulsed and Continuous Atom Lasers

The simplest form of a pulsed atom laser was first created by Mewes et al. [13] by periodically allowing a portion of BEC to drop out of a magnetic trap. Several groups have reported using such a pulsed atom laser for performing atom interferometry [16–19, and others]. One drawback of pulsed atom lasers is the limited supply of output. The finite sized BEC (further limited by loss mechanisms, such as collisions with background gas) must be replenished from time to time. In order to continue an interferometric experiment, new batches of BEC must thus be created, during which time the interferometer is either inoperable or greatly disturbed.

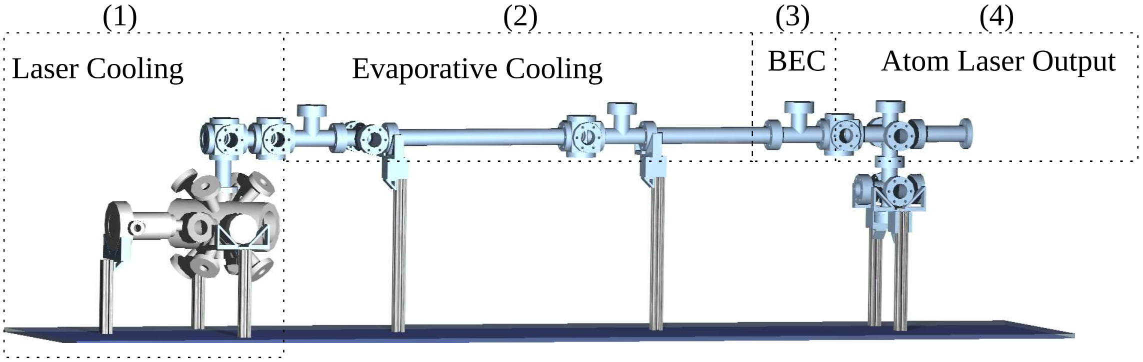

Figure 1.2: Space sequential configuration for BEC generation, intended to drive continuous production of BEC and further continuous-wave atom laser output. Steps (1-4) indicated are typically part of a time sequential process for creating BEC and pulsed atom laser output.

If, on the other hand, BEC is created as the result of a steady-state process, a continuous output of coherent matter waves would be possible [20]. Contrary to the pulsed atom-laser system, wherein all steps typically happen in the same spatial location as a function of time, the continuous atom laser must use a sequence of spatially separated processes, static in time. Fig. 1.2 shows such a scheme where the typical steps of (1) laser cooling, (2) evaporative cooling, (3) BEC formation, and (4) output coupling are spread across the length of an optical table.

1.2 The Magneto-Optical Trap

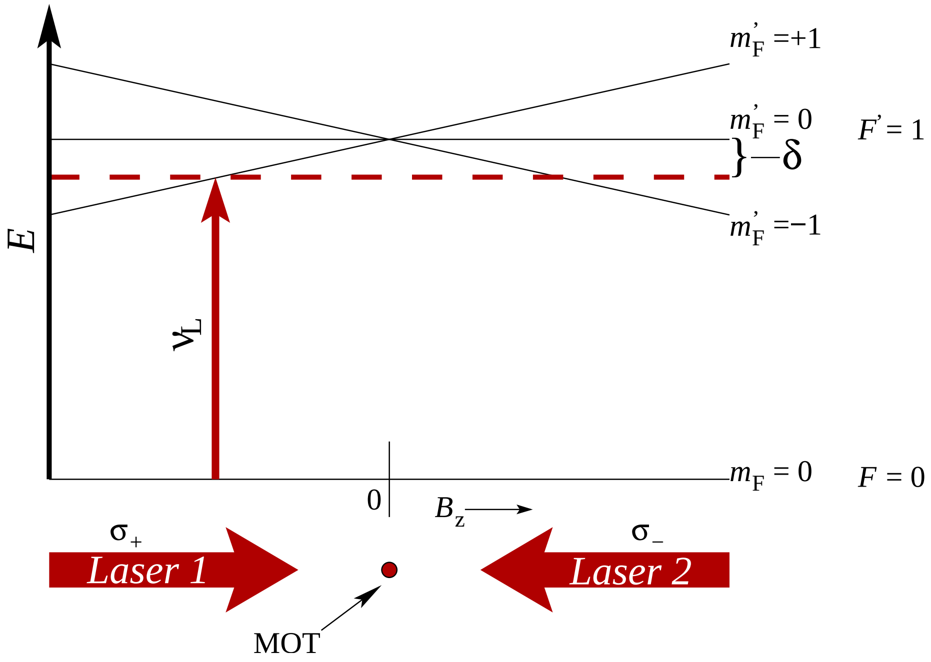

Figure 1.3: Schematic of a 1-D magneto-optical trap (MOT). A MOT is comprised of an inhomogeneous magnetic field and properly detuned and polarized counterpropagating lasers.

With the development of the optical laser, it became possible to access atomic transitions via optical radiation. As the diode laser emerged, the cost of using lasers decreased and the diode laser system became (and still is) ubiquitous throughout the atomic physics community. The magneto-optical trap (MOT) was thus developed into a common workhorse for a plethora of atomic physics experiments.

The principle behind laser cooling is the Doppler-shift enhanced resonant scattering of light. Consider an atomic sample in a region with no magnetic field impinged upon by two counter propagating laser beams, as depicted in the lower portion of Fig. 1.3 (ignore the E vs. B_z plot in the figure for now). If the laser frequency is set just below (red-detuned from) the atomic resonance, an atom traveling towards one laser (and away from the other) will be Doppler-shifted into resonance with that laser (Doppler-shifted out of resonance with the other laser). This will result in the atom preferentially scattering photons from the head-on laser and decelerating until it “sees” the same Doppler-shifted laser frequency from both lasers. If the frequencies of the opposing laser beams are the same in the lab frame, the center of mass of the atomic sample will be slowed to zero velocity. By using two counter-propagating beams for each direction, the sample is slowed in all directions and this creates what is called an *optical molasses* (the atoms appear to be moving through some very viscous medium, such as molasses). Though the atoms are cooled (slowed), they are not trapped and are free to move (under Brownian motion) outside of the optical molasses.

By superposing a quadrupole magnetic field with the optical molasses, the polarization of the laser light becomes significant. For simplicity, let us assume a two level atom with an $F = 0 \rightarrow F' = 1$ transition. In this type of a transition, it is possible for $\sigma_\pm$ light to optically pump atoms to the extreme m_F states. Thus by having counter propagating beams with opposite polarization, as depicted Fig. 1.3, it is possible to create a spatially dependent resonance condition. On one side of the field zero, one of the beams optically pumps the atoms into resonance, while the other quickly optically pumps them out of resonance. This results in atoms being driven towards the zero of the magnetic field. Combining this spatially dependent resonance condition (by using a spatially dependent Zeeman shift) with the

Doppler-shifted resonance, the atomic sample becomes both cooled and trapped.

1.3 Low Velocity Intense Source (LVIS)

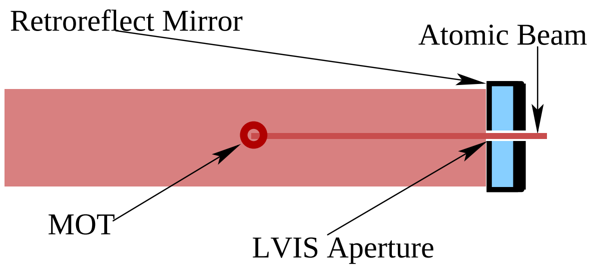

Figure 1.4: Extraction hole in retroreflecting mirror for LVIS function. For clarity, only one retroreflecting beam is shown, rather than three.

It is very common for a MOT to cool and collect atoms from a high-pressure background room temperature gas. Though this is easy to set up, it is prohibitive for experiments which require a low background vapor pressure. Hot background atoms can collide with colder trapped atoms and thus create a loss mechanism for the trap. It is therefore often necessary to use a double-MOT setup, with a high-pressure primary MOT and a low-pressure secondary MOT. The primary MOT is used to initially cool and collect atoms from a hot background vapor that are then transferred into the secondary MOT, where low-pressure experimental work is possible.

A common technique to transfer atoms from a primary MOT to a secondary MOT is shown in Fig. 1.4. By drilling a very small hole in one of the retroreflecting MOT mirrors, a radiation pressure imbalance accelerates the MOT atoms through the small hole in the form of a cold atomic beam. This type of setup is known as an low velocity intense source (LVIS). [21]

1.3.1 Pyramidal LVIS

An alternative form of the LVIS can be created by using a pyramidal MOT (PMOT). The PMOT, as shown in Fig. 1.5, uses the inside surface of a pyramid

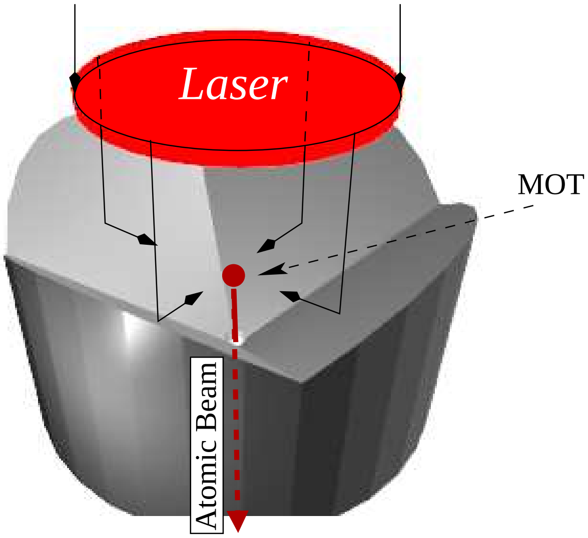

Figure 1.5: Pyramidal MOT used in LVIS mode.

to generate each of the counter propagating beams of the MOT from a single laser beam. [22] A metallic mirror surface ensures the correct $\sigma_{\pm}$ polarization on each of the beams. One of the primary advantages of using a PMOT is that only one MOT laser is required in the setup.

A small aperture at the apex of the pyramid, as shown in Fig. 1.5, provides a radiation imbalance, causing atoms to be pushed through this aperture to the outside of the PMOT. Typical properties of an PMOT-LVIS are a beam divergence of 30 mrad and a longitudinal velocity of 10 m/s $\pm$ 3 m/s. [21]

1.4 Magnetic Trapping and Guiding

Magnetic trapping of neutral atoms, proposed by Pritchard [23] and first realized by Migdall et al. [24], has proven very useful for studying both ground-state atoms (especially for the formation of BEC) as well as Rydberg atoms. [25] Consider a system with a total angular momentum $\mathbf{F}$ with an associated magnetic dipole moment $\boldsymbol{\mu} = \gamma\mathbf{F}$ where γ is called the gyromagnetic ratio of the particular state in question. The torque $\boldsymbol{\tau}$ on the system in the presence of an external magnetic field $\mathbf{B}$ is given

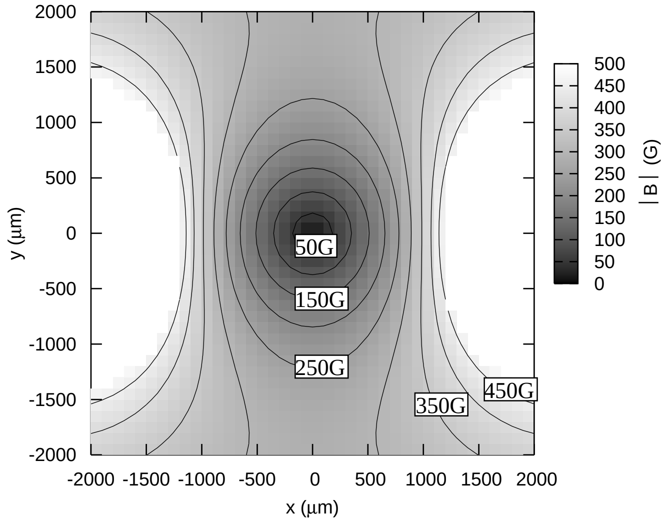

Figure 1.6: Contour of magnetic guiding field between two high current carrying wires. The wires are separated by 4.175 mm and carry parallel currents of 300 A.

by

$$\boldsymbol{\tau} = \dot{\mathbf{F}} = \boldsymbol{\mu} \times \mathbf{B} \tag{1.5}$$

or rather

$$\dot{\boldsymbol{\mu}} = \gamma \boldsymbol{\mu} \times \mathbf{B} \ . \tag{1.6}$$

Taking the time derivative of the magnitude of $\boldsymbol{\mu} \cdot \boldsymbol{\mu}$ as

$$\frac{d}{dt} \left(\boldsymbol{\mu} \cdot \boldsymbol{\mu} \right) = 2 \dot{\boldsymbol{\mu}} \cdot \boldsymbol{\mu} = 2 \left(\gamma \boldsymbol{\mu} \times \mathbf{B} \right) \cdot \boldsymbol{\mu} = 0 \tag{1.7}$$

we find that magnitude of the magnetic moment does not change. Further, by taking the time derivative of $\boldsymbol{\mu} \cdot \mathbf{B}$ as

$$\frac{d}{dt} \left(\boldsymbol{\mu} \cdot \mathbf{B} \right) = \dot{\boldsymbol{\mu}} \cdot \mathbf{B} = \left(\gamma \boldsymbol{\mu} \times \mathbf{B} \right) \cdot \mathbf{B} = 0 \tag{1.8}$$

we find that the angle between the magnetic moment and the external magnetic field is constant. While the magnitude of $\boldsymbol{\mu}$ and its projection onto the $\mathbf{B}$ direction remain constant, the time derivatives of the transverse components do not. Taking the time derivative of Eq. 1.6 yields

$$\ddot{\mu}_\perp = -\gamma \left|\mathbf{B}\right| \mu_\perp \tag{1.9}$$

where $\mu_\perp$ is for each of the transverse directions. Because $|\boldsymbol{\mu}|$ is fixed, this describes a system where the magnetic dipole moment precesses about the direction of the external field with the Larmor frequency ν_0 given by

$$\nu_0 = \frac{\gamma \left|\mathbf{B}\right|}{2\pi} \ . \tag{1.10}$$

By spatially varying the magnitude of the magnetic field, the energy associated with this precession, $h\nu_0$, varies in a conservative manner, with a conservative potential energy V_B given by

$$V_\mathrm{B} = -\boldsymbol{\mu} \cdot \mathbf{B} \ . \tag{1.11}$$

Thus, it is possible to trap a neutral particle with a magnetic field containing a local minimum as long as $\boldsymbol{\mu}$ and $\mathbf{B}$ are anti-aligned. Such a magnetic field geometry can easily be created by using long segments of parallel current-carrying wires. Figs. 1.6 and 1.7 show contours of the magnetic field magnitude with using either two or four wires for such a trap. For both of the these figures, the contour plane is transverse to the wires. Rather than creating a three-dimensional minimum, this field geometry creates something more like a long pipe, through which a stream of neutral atoms can be guided.

In the regions for $B \lesssim 150$ G the atom-guide cross-sections shown in Figs. 1.6 and 1.7 are very similar. The primary difference between the two guide types (at least for the central guiding region) lies in practicality. Assuming wires of 1/8 inch diameter, the separation between the wires for the two cases shown is made such that the minimum aperture, through which observations might be made, is limited

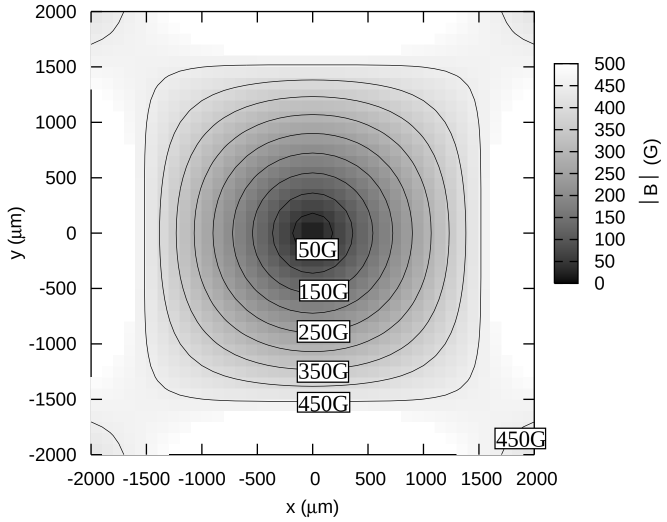

Figure 1.7: Contour of magnetic guiding field between four high current carrying wires. Adjacent wires are separated by 4.175 mm and carry anti-parallel currents of 300 A.

to 1 mm. Because of this limitation, it can be much more convenient to use only two wires to create a guide with a specified magnetic field gradient (i.e. trap frequencies).

1.4.1 Adiabatic Following Criterion

The remaining requirement to fulfill to trap neutral particles is the adiabatic following criterion. This specifies that the precession frequency must be high enough such that changes in the magnetic field direction are easily and smoothly followed. Quantum-mechanically speaking, this means that the magnetic spin quantum number is a good quantum number. In other words, the eigenstates of the adiabatic system are $|F, m_\mathrm{F}\rangle$, where the z-axis of the quantization frame is given by the direction of the local magnetic field vector. Non-adiabatic evolution involves a change of state with respect to this quantization axis, or a flip of the spin state. This is known as a Majorana spin flip. Mathematically, the adiabatic criterion for a static field can be expressed as

$$\nu_0 \gg \frac{v}{h\nu_0}\left|\frac{dV_{\mathrm{B}}}{dx}\right| \tag{1.12}$$

where v is the velocity of an atom in the field in the x-direction. For a harmonic trap with trap oscillation frequency ν_{trap}, Eq. 1.12 averages to

$$\nu_0 \gg \nu_{\mathrm{trap}}\ . \tag{1.13}$$

1.5 Evaporative Cooling

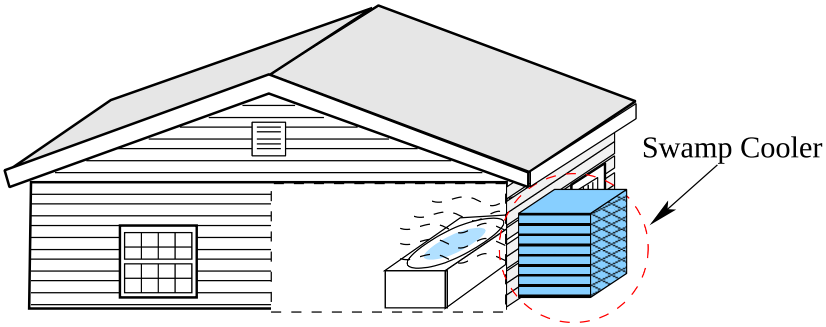

Figure 1.8: Evaporative cooling accounts for the primary heat loss of both bathtubs and swamp-coolers. The swamp-cooler, used primarily in dry regions such as the southwestern United States (circled for those less familiar with such), employs evaporative cooling to cool air which is then blown indoors. (See footnote 5.)

A very commonly observed physical process is that a hot body of water with an open surface, such as with a bathtub (see Fig. 1.8), cools quickly to near room temperature, regardless of the insulation of the container. This observed cooling is primarily due to water molecules leaving the liquid-body by transitioning into free molecules in the gas phase. The process of transitioning trapped liquid molecules into the gas phase is called evaporation and requires a large amount of energy. The remaining molecules must reduce their thermal energy to provide for this evaporation, and are thus cooled in the process. This process continues until the evaporation threshold is reached (this is, thankfully, the reason why bath-water does not freeze due to evaporation). Though the level in the bathtub decreases, enough water molecules are evaporated to cool the bath-water to a unpleasant luke-warm temperature. This is also the process by which swamp-coolers provide cool air to a house, as is pictured in Fig. 1.8. [5]

1.5.1 Forced Evaporation

If it were possible to arbitrarily lower the threshold of evaporation for bath-water, it would also be possible to remove enough energy such that freezing did occur. Threshold lowering, better known as forced evaporative cooling, is precisely the tool commonly used to cool ensembles of particles to temperatures otherwise unachievable (via cryogenics or laser cooling for example). The procedure involves (1) lowering the evaporation threshold and thus truncating the highest energy end of the thermal distribution, (2) allowing time for elastic collisions between the remaining atoms to rethermalize the population to again form a Boltzmann distribution at a lower temperature, and (3) repeating this process until the desired temperature is met or the collision process breaks down.

One way that the rethermalization process becomes ineffective is when the density decreases such that the elastic collision rate γ_{coll}, given by

$$\gamma_{\mathrm{coll}} = 4n\sigma_{\mathrm{T}}\sqrt{\frac{k_{\mathrm{B}}T}{\pi m}}\,, \tag{1.14}$$

is of the same order as the rate at which the atoms collide with background gas. To diminish this effect, it is often necessary to boost the collision frequency by tightening the trap or compressing the atoms as the evaporation threshold is lowered.

---

[5] Note that a health-conscious person would actually not place the swamp-cooler just above the bathtub, though the added wind would help in observing the evaporation process in the bathtub.

1.5.2 rf Induced Removal of Atoms

For magnetically trapped atoms, it is possible to use transitions between internal spin states to perform evaporation. In this experiment, ^{87}Rb atoms in the $5S_{1/2}\ F = 1$ ground state are used in a magnetic guide. This is a triplet state, where $m_{\mathrm{F}} = -1$ is a low-field-seeking substate, $m_{\mathrm{F}} = 1$ is a high-field seeking substate, and $m_{\mathrm{F}} = 0$ is impervious to magnetic fields. The separation between each of these states is in the radio-frequency (rf) domain, and usually on the order of MHz. By matching the rf radiation frequency ν_{rf} with the Larmor frequency ν_0, $m_{\mathrm{F}} = -1$ atoms are trapped in a field-minimum cusp and effectively become evaporated by transitioning into the anti-trapped state with $m_{\mathrm{F}} = 1$ (via the $m_{\mathrm{F}} = 0$ state). Fig. 1.9 depicts evaporation that occurs for atoms with $\nu_0 = \nu_{\mathrm{rf}}$.

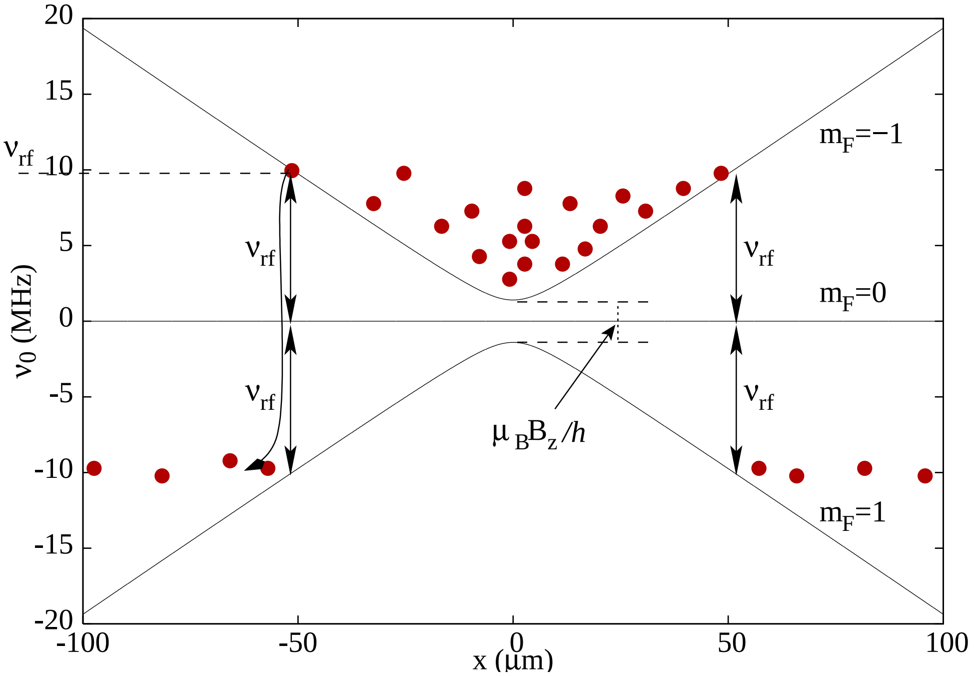

Figure 1.9: The rf "knife" edge in a two-dimensional cross section of atoms in a linear magnetic potential. The rf field couples the magnetically trapped state $|F = 1, m_{\mathrm{F}} = -1\rangle$ to the untrapped state $|F = 1, m_{\mathrm{F}} = 1\rangle$ through a two-photon process. This expels all atoms with energies higher than $h\nu_{\mathrm{rf}}$ (10 hMHz shown here) from the trap. A longitudinal magnetic field, B_z prevents trap losses due to Majorana spin flip at the center of the trap.

The Hamiltonian for an atom in a field composed of an rf component and a static component is given by

$$H = H_0 + H_{\mathrm{B}} = \frac{p^2}{2M} - \boldsymbol{\mu} \cdot (\mathbf{B}_0 + \mathbf{B}_{\mathrm{rf}}(t)) \tag{1.15}$$

where p is the linear momentum, M is the mass, $\mathbf{B}_0$ is a static magnetic field, $\mathbf{B}_{\mathrm{rf}}(t)$ is the time dependent rf magnetic field with a magnitude of $B_{\mathrm{rf}} \cos(2\pi\nu_{\mathrm{rf}} t)$, and $\boldsymbol{\mu}$ is the magnetic dipole moment operator given by

$$\boldsymbol{\mu} = g_{\mathrm{F}} \mu_{\mathrm{B}} \mathbf{F} \tag{1.16}$$

where $\mathbf{F}$ is the total angular-momentum spin operator. Because of the adiabatic following of the spin with the static magnetic field $\mathbf{B}_0$, the $-\boldsymbol{\mu} \cdot \mathbf{B}_0$ term in Eq. 1.15 becomes $h\nu_0 F_{\mathrm{z}}$. For the $-\boldsymbol{\mu} \cdot \mathbf{B}_{\mathrm{rf}}$ term, the component of the rf field parallel to $\mathbf{B}_0$, $\mathbf{B}_{\mathrm{rf},\parallel}$, is negligible because it averages to zero as compared with $h\nu_0$. We will thus assume an x-polarized rf magnetic field denoted by $\mathbf{B}_{\mathrm{rf,x}}$. This leaves

$$\begin{aligned} \boldsymbol{\mu} \cdot \mathbf{B}_{\mathrm{rf,x}}(t) &= g_{\mathrm{F}} \mu_{\mathrm{B}} B_{\mathrm{rf}} F_{\mathrm{x}} \cos(2\pi\nu_{\mathrm{rf}} t) \\ &= h\chi_{\mathrm{rf}} F_{\mathrm{x}} \cos(2\pi\nu_{\mathrm{rf}} t) \\ &= \frac{h\chi_{\mathrm{rf}}}{\sqrt{2}} (F_+ + F_-) \cos(2\pi\nu_{\mathrm{rf}} t) \end{aligned} \tag{1.17}$$

where χ_{rf} is defined to be is the Rabi frequency of the (perpendicular component of the) rf field and where $F_\pm$ are the raising and lowering angular momentum operators defined by

$$F_\pm = \frac{1}{\sqrt{2}} (F_{\mathrm{x}} \pm i F_{\mathrm{y}}) \ . \tag{1.18}$$

The Hamiltonian in Eq. 1.15 can thus be written as

$$H = -h\nu_0 F_{\mathrm{z}} - \frac{h\chi_{\mathrm{rf}}}{\sqrt{2}} (F_+ + F_-) \cos(2\pi\nu_{\mathrm{rf}} t) \ . \tag{1.19}$$

The terms with F_- and F_+ couple atoms in the trapped state with the non-trapped state. For a three level system, with states $|F = 1, m_\mathrm{F} = [-1, 0, 1]\rangle$, and using the usual rotating wave approximation, the Hamiltonian in Eq. 1.19 is written in matrix form as

$$H = h\begin{pmatrix} \Delta & 0 & 0 \\ 0 & 0 & 0 \\ 0 & 0 & -\Delta \end{pmatrix} - \frac{h}{\sqrt{2}}\begin{pmatrix} 0 & \chi_\mathrm{rf} & 0 \\ \chi_\mathrm{rf} & 0 & \chi_\mathrm{rf} \\ 0 & \chi_\mathrm{rf} & 0 \end{pmatrix} \tag{1.20}$$

where Δ is defined as the rf detuning from the Larmor frequency $(\nu_\mathrm{rf} - \nu_0)$. Diagonalizing this Hamiltonian gives the following eigenenergies

$$E_{m_\mathrm{F}} = \begin{cases} h\sqrt{\Delta^2 + \chi_\mathrm{rf}{}^2} \\ 0 \\ -h\sqrt{\Delta^2 + \chi_\mathrm{rf}{}^2} \end{cases} . \tag{1.21}$$

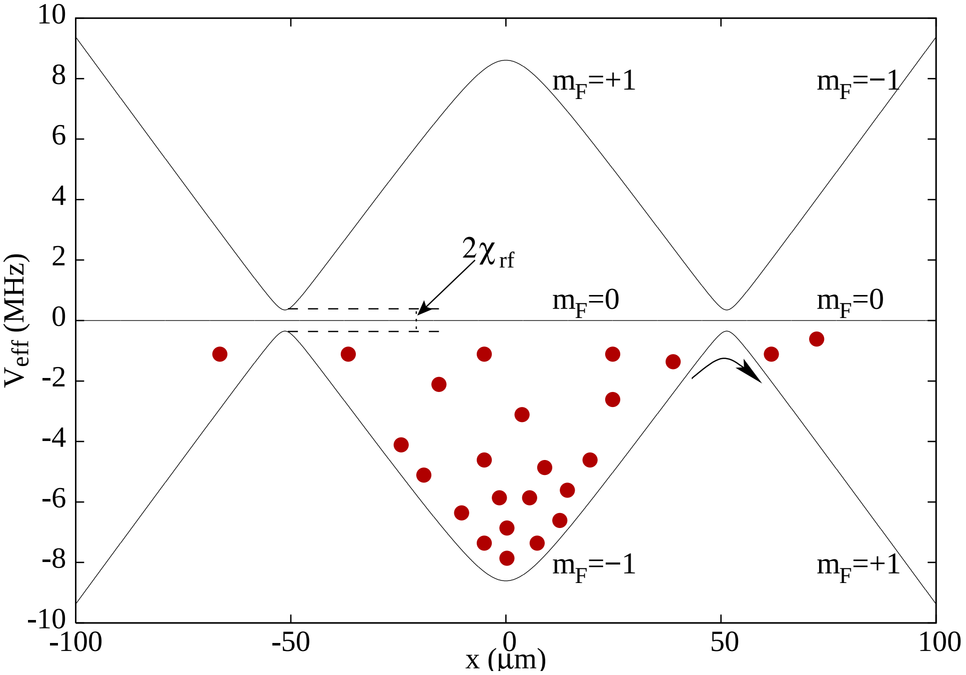

Figure 1.10: Effective potentials of rf-dressed atoms, as a function of position in the static, inhomogeneous magnetic field. In this picture, the effective trapping potential looks more like a standard container, where the edges of the container are specified by the frequency of the rf radiation ν_rf.

Plotting the eigenenergies in the rotating frame, as shown in Fig. 1.10, one can see an effective potential that adiabatically transfers atoms from one internal state to another. In this picture, the central trap (the lower line) looks more like a bucket where the edge of the bucket is adjustable (via ν_{rf}) such that more or fewer atoms are allowed to escape. Forced evaporation is performed experimentally by lowering ν_{rf} until only a very cold and spatially small sample is left.

1.5.3 Evaporation Example

As an example of how fast one might cool using this method, sodium at 200 μK with a density of 10^{11} cm^{-3} has a collision rate of 20 Hz. Using a continuously lowered truncation point of $h\nu_{\mathrm{rf}} = 6k_{\mathrm{B}}T$, on average the density will decrease 0.8% per collision (about 5 collisions per atom are needed to refill the thermal distribution) [26]. This will lead to a average phase space density increase of 2.3% per collision, resulting in obtaining a BEC in about 600 collisions per atom with only 1% of the original population. (See [27] for more on this.)

1.5.4 Lowest Temperature

The lower bound temperature that can be reached via evaporative cooling is limited by the inelastic processes of the sample. The inelastic scattering rate of the sample is given by

$$\gamma_{\mathrm{coll,\,inel}} = nk_{\mathrm{inel}} \tag{1.22}$$

where k is a velocity-independent rate with units of [m^{3}s^{-1}]. The limiting temperature is found when γ_{coll} and $\gamma_{\mathrm{coll,\,inel}}$ are of the same order [28]. This gives

$$T_{\mathrm{limit}} = k_{\mathrm{inel}}^2 \frac{\pi m}{16k_{\mathrm{B}}\sigma_{\mathrm{T}}{}^2} \tag{1.23}$$

as the lower bound of the temperature that can be reached via evaporative cooling[6]. For alkali atoms, $T_{\text{limit}} \sim 1$ nK (within an order of magnitude), far beneath the temperature needed to obtain a BEC, allowing evaporative cooling to play a major role in the BEC preparation process.

---

[6] In real situations, the limit is around $100T_{\text{limit}}$ [28].

CHAPTER II

Experimental Setup

As mentioned in Ch. I, the goal of this work is to establish a continuous-wave atom laser. This entails, as described earlier, the transformation of the time-sequential BEC preparation into a space-sequential method. For convenience, we reproduce the schematic of the time-sequential method in Fig. 2.1.

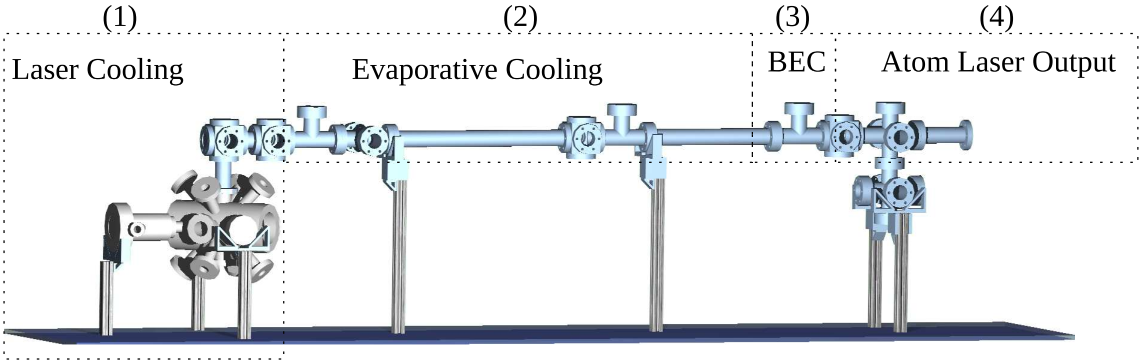

Figure 2.1: Space sequential configuration for BEC generation, intended to drive continuous production of BEC and further continuous-wave atom laser output.

In this chapter, we will discuss in more detail the purpose and parameters of each section in the atom guide. We will begin where the atoms are collected and initially cooled in the "Laser Cooling" component indicated in Fig. 2.1. We will discuss the injection scheme of the unguided atoms into the magnetic guide. The rf-induced removal of atoms and intended evaporation scheme in the "Evaporative Cooling" component indicated in Fig. 2.1 will then be discussed. This chapter will end with a brief outline of the anticipated BEC instantiation and atom-laser startup sequence.

2.1 Overview

Our experimental setup consists of two laser-cooling stages that feed atoms into a high-gradient magnetic guide stage. Atoms, first collected in a vapor-cell pyramidal magneto-optical trap (PMOT in Fig. 2.2) as described in Sec. 1.2, are transferred into and recaptured by a secondary MOT (MMOT in Fig. 2.2). This MMOT then injects the atoms into a 1.7 m long magnetic atom guide with a tunable velocity. As shown in Fig. 2.2, the guide is comprised of a vertical injection/launch section (about 0.2 m height) and a horizontal section (1.5 m length) in which rf-induced transitions are employed to selectively remove the most energetic atoms from the guided atomic flow.

The magnetic atom guide consists of a pair of in-vacuum hollow copper tubes with an outer diameter of 3.18 mm and a center-to-center separation as low as 4.18 mm. The copper tubes are introduced into the vacuum chamber through Swage-Lok feedthroughs with Teflon ferrules and are precision-mounted in the vacuum on a steel rail using alumina, aluminum spacers, and polyimide foil (see inset of Fig. 2.2). The mounts are designed such that a well-defined tube separation is achieved as a function of the longitudinal position in the magnetic guide. The aluminum-polyimide mounts are sufficiently loose so as to allow the tubes to slide longitudinally. This is necessary to provide relief for thermal expansion, which can be up to ~ 1 mm under normal operating conditions. The steel rail on which the guide tubes are mounted provides stability and rigidness to the structure. Long, periodic slots in this steel rail allow optical access to the region between the guide tubes. A precision machined

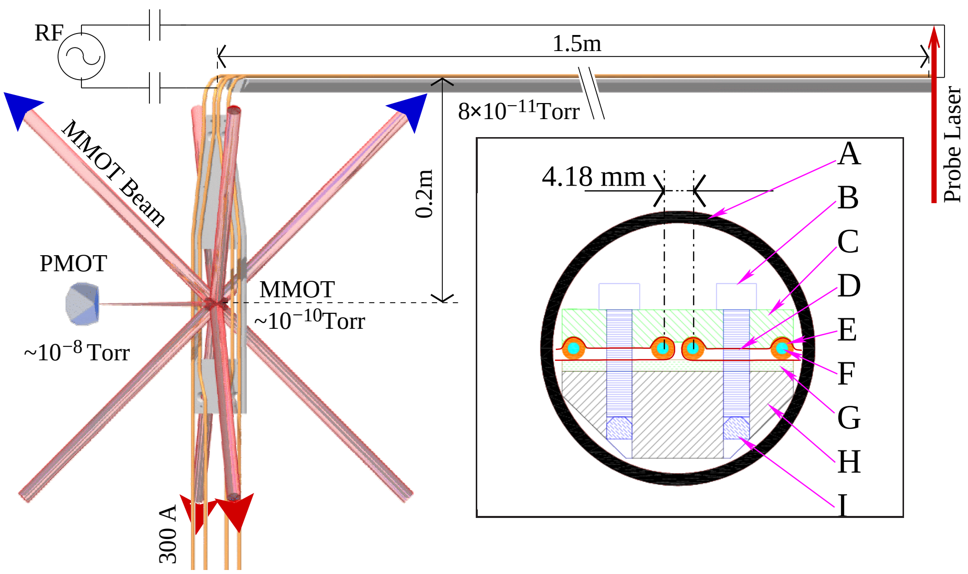

Figure 2.2: Sketch of the experimental setup. Atoms are injected from a pyramidal magneto-optical trap (PMOT) via a “Moving MOT” (MMOT) into the vertical injection/launch section of a magnetic atom guide. As the injected atomic flow rises upward, it slows under in the influence of gravity and becomes magnetically compressed. The flow then propagates into a long horizontal guide section. A radio-frequency current coupled into the horizontal guide section is used to remove the most energetic atoms from the guided atomic flow. The system has three differentially pumped vacuum regions, the pressure values of which are shown here. The inset on the right shows a cross section through the horizontal section of the guide. (A) Vacuum chamber, (B) mounting screws, (C) aluminum spacers, (D) insulating polyimide film, (E) guide wires, (F) coolant, (G) alumina spacers, (H) guide rail, (I) lock screws.

rail surface minimizes washboard-like gravitational bumps along the length of the guide. The hollow guide tubes are cooled using a closed-circuit, high-pressure water flow. At a current of 300 A, the magnetic-field gradient reaches values of 2.7 kG/cm, generating accelerations of 90 g on ^{87}Rb atoms in the state $|F = 1, m_{\mathrm{F}} = -1\rangle$. The system is routinely operated using the continuous-mode parameters listed in Tab. 2.1.

2.2 Atomic-flow Injection

2.2.1 Primary Atomic Beam: Side-loading the Moving MOT

The primary atomic beam used to load the atom guide is generated by the PMOT [29], a fluorescence image of which is shown in Fig. 2.3. Our PMOT, operated with a single laser beam with a bandwidth of <2 MHz full width at half

Guide current	300 A
Field gradient (end of guide)	2.7 kG/cm
Dissipated power	3.2 kW
Cooling water pressure	120 PSI
Water inlet temperature	16°C
Water temperature differential	30°C
Vacuum pressure (horizontal guide region)	8×10^{-11} Torr

Table 2.1: Parameters of continuous-mode operation of the magnetic atom guide.

maximum (FWHM) and 100 mW power, is a version of the MOT [30] that emits a cold atomic beam through a hole in the apex of a pyramidal mirror [22]. This is similar to a Low-Velocity Intense Source of atoms (LVIS [21]). To initiate the atomic beam from the PMOT, the atom cloud in Fig. 2.3 is centered over the apex of the pyramid using a tunable bias magnetic field. The resultant imbalance in radiation pressure causes the atoms to be extracted through the indicated exit hole in the form of a freely propagating atomic beam.

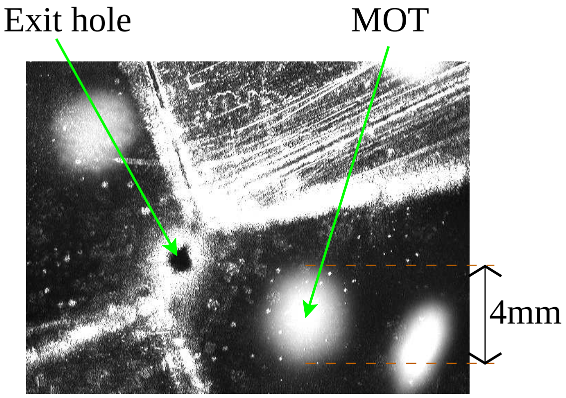

Figure 2.3: Primary pyramidal MOT (PMOT). The image shows the actual atom cloud and multiple reflections thereof in the pyramidal mirror.

2.2.2 Injection into the Magnetic Guide

The atomic beam emitted by the PMOT propagates into the differentially pumped ultra-high vacuum ($\sim 10^{-10}$ Torr) section of the setup that contains the vertical portion of the atom guide. As seen in Fig. 2.2, the horizontal atomic beam emitted by the PMOT side-loads the vertical injection/launch section of the atom guide at a right angle. The injection into the guide is accomplished using a “moving MOT” (MMOT [31, 32]). As shown in Fig. 2.2, the four coplanar copper tubes that provide the magnetic guiding fields throughout most of the apparatus also create the two-dimensional magnetic quadrupole field necessary for the MMOT. In the MMOT region, the inner tubes are spaced at a center-to-center distance $a_1 = 3.7$ cm and carry parallel currents, while the outer tubes are spaced at a distance $a_2 = 5.7$ cm and provide the current return-path. For a current of $\mathcal{I} = 300$ A, the radially symmetric field gradient near the guide axis,

$$\frac{\partial B}{\partial \rho} = \frac{4\mu_0 \mathcal{I}}{\pi} \left[\frac{1}{{a_2}^2} - \frac{1}{{a_1}^2} \right] \quad , \tag{2.1}$$

is about 20 G/cm at the location of the MMOT. Four laser beams are directed at the intersection point of the atomic beam incident from the PMOT with the vertical launch section of the guide. All beams are aligned at an angle of 45° relative to the vertical guide axis. As Fig. 2.2 shows, the four MMOT beams consist of a pair with upward and a pair with downward directions. The planes defined by these beam pairs are orthogonal to each other and their intersection defines the vertical axis. The beams with downward direction are operated at a slightly lower frequency than those with upward direction. The MMOT beams are red detuned from the ^{87}Rb $5S_{1/2}\ F = 2 \ \rightarrow \ 5P_{3/2}\ F' = 3$ transition by an amount $\delta_{\mathrm{MMOT}} \approx 2\Gamma$ as indicated in Fig. 2.4. The beams are circularly polarized in a suitable manner and have intensities of about 5 mW/cm^2. This configuration of magnetic fields and laser beams results in a two-dimensional MMOT that compresses the divergent atomic beam emitted by the PMOT into a small-diameter cylindrical region ($\sim 200\ \mu$m) around the guide axis (which is vertical in the launch section). The average velocity, or launch velocity, of the atoms leaving the MMOT, v_{MMOT}, is parallel to the guide axis and can be tuned by varying the frequency difference between the up-going and down-going MMOT beams. In the frame of reference of atoms moving upward along the guide axis, the frequencies of the MMOT are Doppler-shifted such that all beams appear at the same frequency. Thus, $v_{\mathrm{MMOT}} = \epsilon\lambda/\cos(\theta)$, where ϵ is half the frequency difference between the up-going and down-going beams, λ is the wavelength of the atomic transition (780.244 nm) and $\theta = 45°$ is the angle between the MMOT beams and the vertical. Typically, the relative detuning is adjusted such that the MMOT launches the atoms at $v_{\mathrm{MMOT}} = 2.2$ m/s, which is within the range of velocities where MMOTs have proven to operate well [33–37].

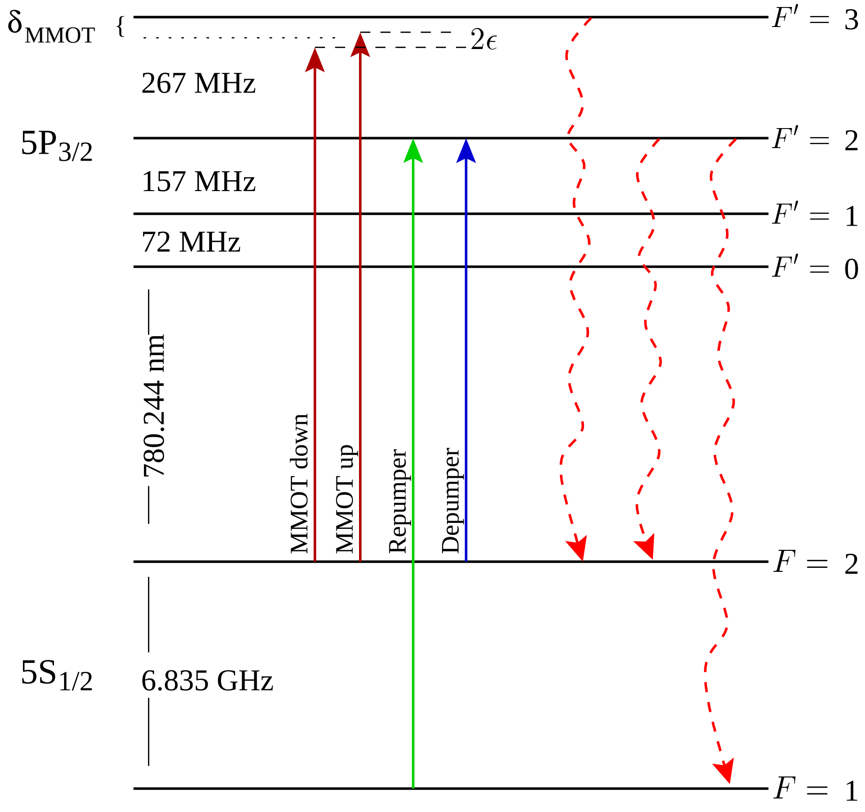

Figure 2.4: Level diagram for ^{87}Rb transition used to cool and trap atoms. The solid red lines indicate the MMOT cooling lasers with a frequency difference of 2ϵ. The green and blue lines indicate the repumping and depumping channels respectively. The relevant spontaneous decay channels are also drawn. Note that this level diagram is not to scale.

2.2.3 Dark-state Extraction

Each atom emerging from the MMOT must traverse through the fringe fields of the four MMOT laser beams. This fact poses a problem because accurate control of beam shapes and intensities in the fringe-field regions of the four MMOT beams is virtually impossible. Therefore, any extracted atom would experience strong, random differential radiation pressures in the fringe fields of the MMOT beams, causing the velocity to change in an erratic manner. The solution to this problem is dark-state extraction, i.e. optical pumping of the atoms into a "dark state" that does not scatter any MMOT photons. The optical pumping into the dark state needs to occur inside the MMOT volume, *before* the atoms reach the fringe fields of the MMOT laser beams. As explained in [38], the location of optical pumping into the dark state is defined through a layered arrangement of a MMOT repumper beam with a well-defined upper knife-edge and a depumper beam with a well-defined lower knife-edge. Any overlap between the repumper and the depumper beams needs to be avoided, while a small gap is allowable. The knife-edge planes are oriented orthogonal to the vertical guide axis. The MMOT repumper beam is resonant with the ^{87}Rb $5S_{1/2}\ F = 1 \ \rightarrow\ 5P_{3/2}\ F' = 2$ transition, while the depumper is resonant with the $5\mathrm{S}_{1/2}\ F = 2 \ \rightarrow\ 5P_{3/2}\ F' = 2$ transition, as depicted in Fig. 2.4. This arrangement ensures that all atoms are transferred into the dark state $F = 1$ after traversal of the depumper knife-edge. Statistically, approximately one-third of the dark-state atoms will exit the MMOT in the magnetically guided sublevel $|F = 1, m_{\mathrm{F}} = -1\rangle$.

Fluorescence images of the MMOT in launch-mode show a characteristic narrowing shape, indicated by the dotted lines in Fig. 2.5. As the atoms travel upward along the extraction trajectory, their transverse excursions away from the guide axis diminish. The narrowing reflects the progression of laser cooling into the moving

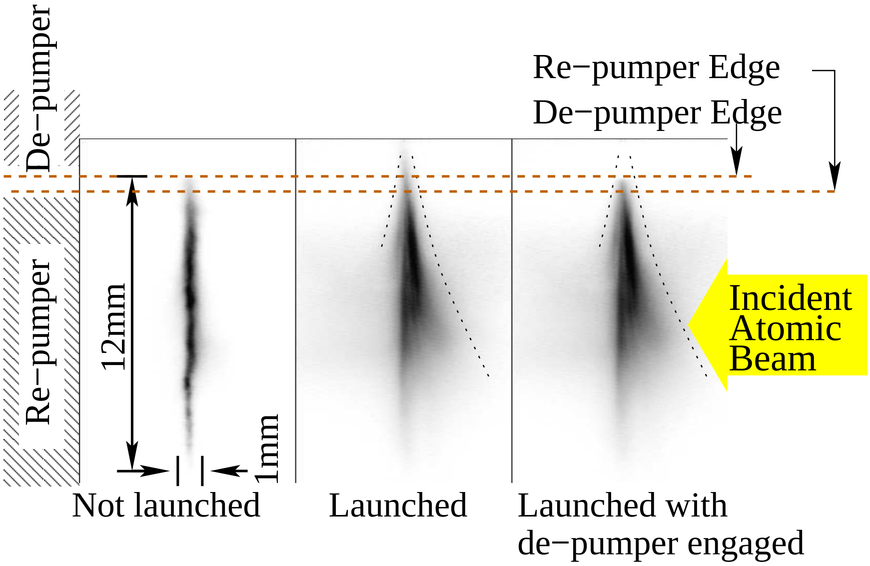

Figure 2.5: Fluorescence images of the MMOT (guide-axis vertical). The exposure times are chosen such that the images do not saturate. Left: Launch velocity $v_{\mathrm{MMOT}} = 0$ m/s. The fluorescence rapidly diminishes above the repumper knife-edge. Middle: Launch velocity $v_{\mathrm{MMOT}} = 1.6$ m/s and depumping beam blocked. Atoms are transported upward out of the range of the MMOT, leaving a thin trail of fluorescence along the guide axis above the repumper edge. Right: Launch velocity $v_{\mathrm{MMOT}} = 1.6$ m/s and depumping beam active. The fluorescence abruptly diminishes above the depumper edge, as the depumper optically pumps all atoms into the dark state $F = 1$. The dotted lines in the middle and right images outline a narrowing of the MMOT fluorescence as a function of height.

reference frame of the MMOT as a function of height in the guide. Thus, optimal operation of the MMOT shows a chevron-like pattern where the tip is completely narrowed, indicating optimal cooling in the transverse directions at the extraction point.

It is also characteristic of these images that fluorescence is absent (left image) or diminished (middle image) above the repumper cutoff. This reflects off-resonant optical pumping (by the cooling beams) of the atoms into the dark extraction state $F = 1$ once they have left the range of the repumper beam. We have found that a small fraction of the atoms can be extracted from the MMOT in the dark state $F = 1$ just by ensuring that the upper edge of the repumping region is located well within the MMOT region, as in the middle image. The flux of atoms extracted in the dark state is drastically improved by employing the depumper beam, as in the right image of Fig. 2.5. The sharp fluorescence cutoff at the lower edge of the depumper beam, seen in the right image, shows that all atoms still reaching the depumper region in the bright $F = 2$ state are transferred into the $F = 1$ dark extraction state by rapid, on-resonant optical pumping. We have found experimentally that the presence of the depumping beam increases the yield of guided atoms by at least a factor of five over the yield obtained in the absence of the depumper (this contrast is relevant in Fig. IV.4.6).

2.3 Gravitational Slowing and Magnetic Compression

The vertical launch section of the guide has a height of 0.2 m from the depumper knife-edge to the top end of the 90° bend. In the launch section, the atoms are slowed down by gravity as they travel upward. Using the MMOT laser frequencies as a velocity tuning parameter, the MMOT extraction velocity v_{MMOT} is adjusted such that the atomic flow has a reasonably low velocity at the top of the launch section while maintaining a high atomic flux. We have found a useful extraction velocity range of $2.2 \text{ m/s} \leq v_{\mathrm{MMOT}} \leq 2.8 \text{ m/s}$, corresponding to a velocity range $1 \text{ m/s} \leq v \leq 2 \text{ m/s}$ near the top end of the 90° bend.

The atom guide is tapered [39, 40], i. e. the center-to-center distance between the inner pair of guide tubes decreases from about 3.7 cm at the location where cold atoms are transferred from the MMOT into the guide down to 5.17 mm in the 90° bend. Taking the fields of both the inner and outer tube pairs into account, from Eq. 2.1 it follows that the field gradient increases from about 20 G/cm at the MMOT to 1.7 kG/cm in the 90° bend. A crucial benefit of the gradient increase is that the atomic distribution becomes magnetically compressed in the transverse directions as the atoms propagate through the tapered region. The compression enhances the collision rate and will thus, in the future, facilitate evaporative cooling.

In the absence of collisions, the action of the transverse motion of the magnetically guided atoms, $S_\perp = \oint \mathbf{p}_\perp \cdot \mathbf{dq}_\perp$, is adiabatically conserved [39, 40]. The adiabatic invariance entails a partial conversion of forward kinetic energy into transverse energy in the magnetic-compression region. Consequently, atoms in the vertical launch section of the guide are decelerated due to gravity and an additional retarding force that grows with increasing transverse energy. Simulations show that due to this effect about half the atoms in the magnetically guided state $|F = 1, m_\mathrm{F} = -1\rangle$ are reflected backward. The reflected atoms are partially re-cycled, because they fall back into the MMOT. It is also noted that an increased collision rate will break the adiabatic conservation of the transverse action, and therefore reduce the fraction of reflected atoms.

Once in the narrow region of the vertical guide section (5.17 mm center-to-center wire separation), additional velocity filtering occurs due to gravity and the 90° bend. The fastest atoms overshoot the bend and the slowest atoms fall back into the MMOT. From simulations, we expect this filtering to further reduce the flux by about 15%.

The total coupling efficiency from the MMOT into the horizontal guide section is given by the fraction of atoms that exit the MMOT in the magnetic sublevel $m_\mathrm{F} = -1$ (33%) times the probability that an atom does not fall back in the vertical guide section or overshoot in the bend (40%-50%). Thus, an initial estimate of the flux into the horizontal guide section is $\Phi_\mathrm{Hor} = 0.15\Phi_\mathrm{MMOT} = 8 \times 10^7\ \mathrm{s}^{-1}$.

2.4 The Bend

Atoms in the correct velocity class will enter the horizontal guiding section 20 cm above the MMOT extraction point via the 90° bend. One of the most important features provided by this bend is the optical shielding of the stray light from the MMOT region. Atoms traveling in the magnetic guide can be quickly transferred into magnetically anti-trapped states through scattering of spontaneous photons. It is therefore necessary to eliminate all possible stray light sources from the magnetic guiding region. As described in Sec. 2.2.3, atoms passing into the horizontal guide are already transferred into a state which is dark with respect to the cycling transition of the MMOT. Thus, stray repumper light from the MMOT is the primary source from which the magnetic guide region must be shielded.

In addition to optical shielding, the 90° bend allows for natural apertures required for differentially-pumped vacuum stages between the MMOT and the horizontal guide. With this differential vacuum, we indeed have pressures low enough such that it should be possible to maintain a BEC in the horizontal guide region.

2.5 rf Knife Edge

2.5.1 Optimal rf Coupling: TEM Mode of rf Waveguide

It is typical for rf radiation in evaporative cooling experiments to come from auxiliary antennas that are aligned such that maximal rf power is coupled into the trapping region. It is often possible, for example, to have a coil antenna shine rf power into a sample of trapped atoms. For the case of the atom guide, the use of conventional rf antennas becomes problematic. The large grounding surfaces within a short distance of the atomic beam provide excellent magnetic shielding. This makes it difficult for external rf radiation to penetrate into the guide region.

Rather than rely on additional antennas outside of the magnetic guide, we use the DC current carrying wires of the guide in the form of an rf waveguide. By coupling an AC component onto the wires, we are able to efficiently irradiate the atomic beam with rf-power. Fig. 2.6 shows a calculation of the rf magnetic field, B_{rf}, projected into the direction perpendicular to the local DC magnetic field vector (thus, the plotted data is proportional to the Rabi frequency of the rf coupling field). This figure shows that indeed a large portion of the rf power is concentrated in the region where the atomic beam travels. Thus, we are able to provide rf power in the atomic beam region in an efficient manner.

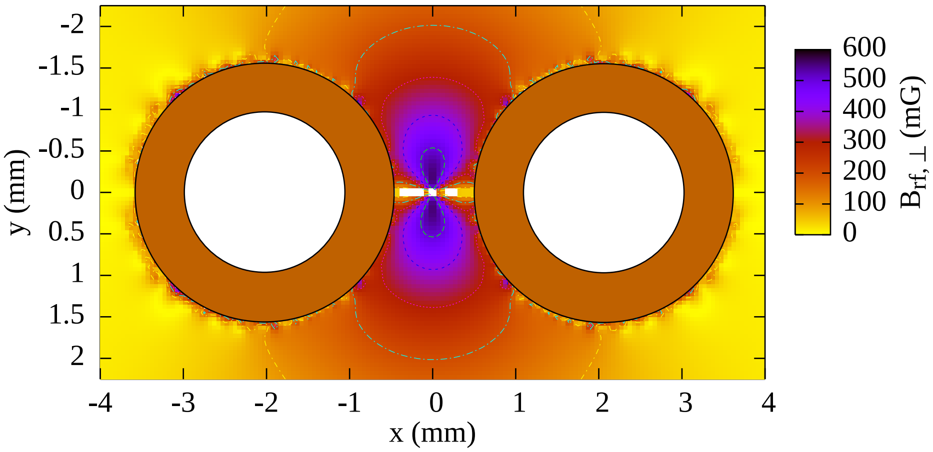

Figure 2.6: rf electromagnetic waveguide using the magnetic atomic guide wires. The power of this rf waveguide is transmitted in the TEM mode. This figure shows the magnitude of the rf magnetic field, B_{rf}, projected into the direction perpendicular to the local DC magnetic field (denoted as $B_{\mathrm{rf}\perp}$ in the key of the plot). Assuming an electrostatic condition, B_{rf} is given by $\sqrt{\mu\epsilon}\,\mathbf{z}\times\mathbf{E}$, where $\mathbf{E} = -\nabla\Phi$, where Φ is determined by an over-relaxation algorithm. In this calculation, an rf-current of 3 A in the each of the wires is 180° out of phase with the other.

2.5.2 Avoiding rf Crosstalk: Segmented rf Waveguides

In conventional BEC experiments, the evaporation threshold is lowered by changing the rf frequency. Applying this idea to the cw atom laser design described in this thesis, it would be necessary to change the rf frequency as a function of longitudinal position along the length of the guide. This scheme poses a second and even more detrimental problem for external rf sources (such as rf coils wrapped around the outside of the guide wires as described in [41]). External rf sources will radiate large regions of the guide with rf power of the given frequency. For performing longitudinal evaporative cooling, it is important that rf radiation of lower frequency not propagate into regions with higher frequency. If such crosstalk is present, the thermal distribution of the upstream atomic beam will be truncated at a rate higher than intended. This will significantly deplete the atomic beam and stall the evaporative cooling process.

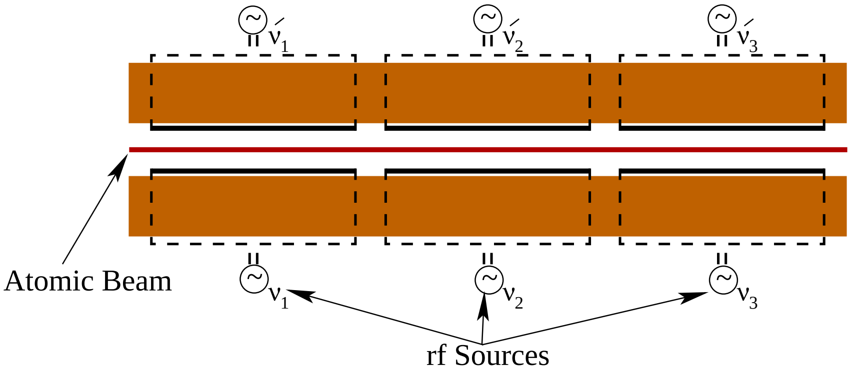

Figure 2.7: Segmented rf frequency ramp. Using the auxiliary rf wires, the rf frequency can be changed in a discretized manner along the length of the atom guide. By using an rf waveguide as the antennas, upstream propagation of rf radiation can be minimized.

Taking the rf-waveguide notion a step further, it is also possible to achieve optimal coupling into the atomic beam while minimizing the amount of crosstalk between regions of different rf frequency. This can be done along the length of the atom guide by using several pairs of rf antennas on the *inside* of the atom guide wires, such as shown in Fig. 2.7. Each pair of rf antennas creates a small segment of an rf waveguide (supporting the TEM mode only). Fig. 2.8 shows a calculation of the rf magnetic field, B_{rf}, projected into the direction perpendicular to the local DC magnetic field vector (again, the plotted data is proportional to the Rabi frequency of the rf coupling field). [1] In this case, the current density is kept the same as in Fig. 2.6. By using an rf waveguide to irradiate the atoms with rf power, the radiation is concentrated within the waveguide, thus minimizing crosstalk between regions of different rf frequencies.

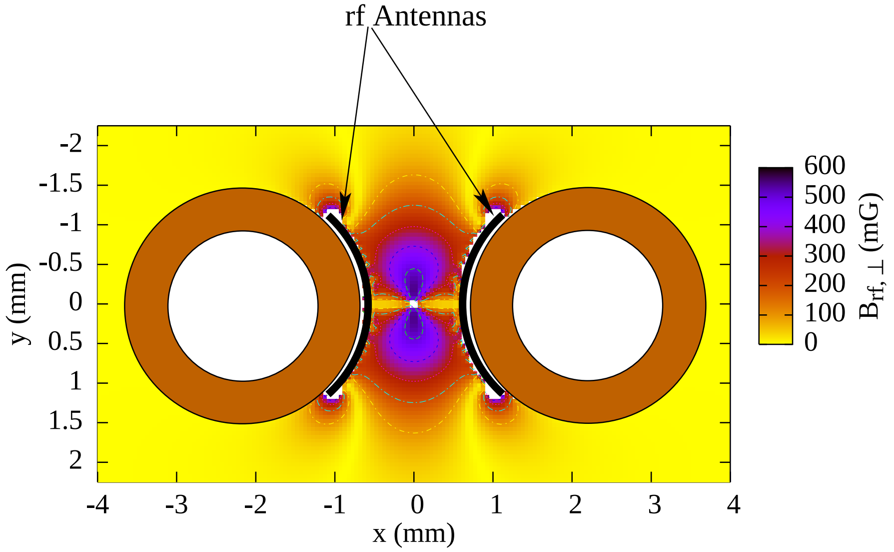

Figure 2.8: rf electromagnetic waveguide using auxiliary rf wires. Shown here is the magnitude of the rf magnetic field, B_{rf}, projected into the direction perpendicular to the local DC magnetic field (denoted as $B_{\mathrm{rf}\perp}$ in the key of the plot). Contrary to the rf guide in Fig. 2.6, a pair of auxiliary rf antennas carries the rf current. The current density in the antennas is kept the same as in Fig. 2.6. By using auxiliary antennas, various rf frequencies could be applied as a function longitudinal position in the atom guide. Similar to Fig. 2.6, an rf-current of 0.75 A in the each of the antenna wires is 180° out of phase with the other.

---

[1] It should be noted that in practice, it should only be necessary to use a single rf source for each frequency (i.e. not using two sources, 180° out of phase with each other).

2.5.3 Other Methods of Altering the Evaporation Threshold

It may also prove helpful to use alternative methods of lowering the evaporation threshold. One such method could be the variation of the longitudinal magnetic field. In this case, a fixed rf frequency would be coupled directly to the DC wires. This technique would force evaporative removal by pushing up the bottom of the guide such that the contents spill over the fixed edge. To avoid acceleration along the guide it will also be necessary to change the gravitational potential (by tilting the guide). The efficacy of these parameters for modifying the evaporation threshold will be discussed in Ch. VI.

2.6 Three-Dimensional Trap for BEC

As evaporatively cooled atoms reach the end of the magnetic guide, it will be necessary to establish a three-dimensional trapping field wherein the BEC can form. With such a trap implanted in the atom guide, it is only necessary to provide additional trapping in the longitudinal directions, as the atom guide provides ample trapping in the transverse directions. For the longitudinal trapping, there are a variety of tools that can be used in combination to form the correct trap. For the end of the trap, a high-power, blue-detuned (670 nm) sheet of light will be used to form a repulsive light-shift induced barrier. The main body of the trap could be created by either electric potentials (using the Stark shift), or perhaps by just tilting the table such that a microgravity trap occurs just before the light-shift barrier.

2.7 Anticipated Atom Laser Startup

As the guide fills up with a gas of cold atoms, collisions will increase and evaporative cooling will become more efficient. Magnetic compression along the length of the guide will increase the density and sustain the collision rate, preventing reverse heat conduction through the guide (collisions will prevent hot atoms, from the beginning of the guide, from traveling to the cold sections at the end of the guide). Convection currents in the guide are negligible due to the large aspect ratio (transverse size compared to the longitudinal size) of the cold-gas column. This will result in a negative temperature gradient throughout the length of the guide, such that a very cold, near-degenerate gas arrives at the location of the BEC trap. After the BEC forms, coherent atomic radiation will tunnel through the light-shift induced barrier as its height is controlled, and the atom laser will be achieved.

CHAPTER III

Detection: Open Channel Probe

As the setup described in Ch. II was built, it became necessary to develop methods of observing the cold, guided atomic beam. This chapter outlines the motivation for this development and presents the technique used for imaging the atomic beam without the need to disturb its steady state nature.

While the development of a wide variety of traps for atoms [3] and molecules [4] has spanned the past few decades, imaging has been the key to observing and investigating physical phenomena in trapped-particle clouds. The most common method of imaging distributions of cold atoms involves the illumination of the trap region with a monochromatic probe laser tuned to a closed-channel "cycling" transition and detection of the ensuing fluorescence. Closed-channel imaging leads to a high photon yield per atom and thus a high signal-to-noise ratio of the images. In high-gradient traps, the fluorescence rate per atom is highly dependent on position due to spatial variations of Zeeman- and/or Stark-shifts throughout the sample, variations of the angle between the laser polarization and the trapping fields, and optical pumping among magnetic sublevels. In this case, the processing of fluorescence images into actual particle density distributions requires very detailed modeling. Hence, magnetic, electric, and optical trapping fields are typically switched off during the fluorescence or absorption imaging. By switching the fields off, the spatial variation of the fluorescence rate is avoided, resulting in a uniform photon yield per atom and reliable conversion of fluorescence images into density distributions.

In some systems, switching the trapping fields off in order to perform distribution measurements may not be possible or even desirable. This is the case, for example, in magnetic atom traps where ferromagnetic materials are used [42, 43]. In experiments involving magnetic traps with high field gradients, such as achieved in atom-chip experiments [44] or high-gradient atomic guides [45], the process of switching fields can involve switching large currents. This leads to rapid thermal cycling effects that may cause micro-leaks to appear at the vacuum feedthroughs [41] and also to transients in the current loop due to high inductance. In other cases, it is desired to measure the steady-state distribution of cold atoms in systems with an equilibration time in the range of several seconds or more, such as a scheme shown to load a Ioffe-Pritchard trap with chromium atoms [46] as well as continuously loaded, long atom guides [41, 45]. In such cases, switching the fields off in order to acquire an image will necessitate a long waiting time for the system to become ready again for the next image to be taken. Consequently, an unacceptably low measurement repetition rate may result. Therefore, a robust imaging method is needed that delivers true representations of cold-atom distributions with the trapping fields left on.

At least two methods exist from which a signal that is directly proportional to the density of the sample can be delivered. The first, phase-contrast imaging (a non-destructive scheme), allows one to measure the change of the index of refraction for far-off-resonant light propagating through an atomic sample that is optically dense at resonant frequencies. The disadvantage of this method lies in the requirement to have atomic samples of very high density, which in many cases are not available.

A second method relies on the optical pumping of atoms using an open transition. This open-channel imaging method is occasionally used to measure the total atom number in optically thick samples [47, 48]. As discussed in this paper, in certain cases it also is the best method to characterize non-optically thick samples [41, 45].

In this chapter, we characterize the performance of the open-channel cold-atom imaging method used to profile and measure the temperature of our guided atomic beam. This is a case where Zeeman shifts change significantly through the detection region. The method yields accurate atomic density distributions and should be applicable to other trapping situations as well as to the trapping of molecules (which do not offer closed optical transitions).

3.1 Closed-channel Imaging

3.1.1 Continuous Atomic-beam Probing

To most readily observe the atomic beam, continuous repump and probe lasers are co-aligned such that they illuminate a small portion of the atomic flow. The repump laser, tuned to the $F = 1 \rightarrow F' = 2$ transition, optically pumps the guided atoms in the $|F = 1, m_{\mathrm{F}} = -1\rangle$ state into an $F = 2$ state. The repumped atoms generate abundant fluorescence from the probe laser, which is tuned on-resonance with the closed-channel $F = 2 \leftrightarrow F' = 3$ cycling transition. The fluorescence imaged onto a CCD camera enables continuous, spatially resolved, real-time atomic-beam observation (see Fig. 3.1, left image).

Continuous imaging of the atomic distribution has certain drawbacks. The radiative force from the probe laser accelerates atoms quickly out of resonance and causes a diminishing signal in the atomic beam direction. Further, due to repumping of the atoms into the $F = 2$ bright state and the subsequent closed-channel fluorescence on the $F = 2 \leftrightarrow F' = 3$ transition, a mixture of low- and high-magnetic-field seeking sub-levels is populated. The magnetic-dipole force in the guide is different for these various magnetic sub-levels. In addition, the atoms are exposed to the diffusive component of the radiative force due to the probe laser. Hence, the atomic flow is significantly diffused in a complicated manner during the imaging. Therefore, the observed image profile transverse to the atom flow is wider than the actual atomic distribution in the guide. The widening of the beam profile increases in the direction of the atomic flow. These effects lead to images a of broadened and distorted atomic-beam, as shown in the left inset (a) of Fig. 3.1.

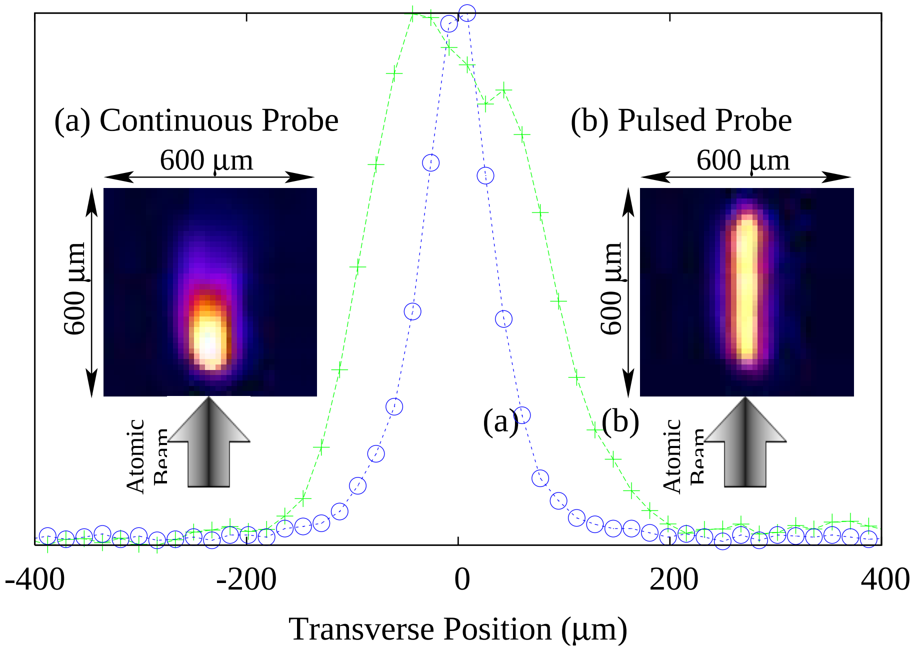

Figure 3.1: Fluorescence images of distorted and non-distorted atomic beams. (a) Fluorescence image of a distorted atomic beam obtained with a continuous probe. The distortion/broadening is due to radiation pressure and magnetic forces acting while the atoms are being imaged (b) Non-distorted atomic beam imaged via strobed probe pulses of 20 μs duration and 1 ms separation.

3.1.2 Elimination of Atomic-beam Distortion Using a Strobe Technique

In order to obtain images of the undistorted atomic distribution, the repump and probe beams in the imaging region are pulsed. The duration of each strobe pulse is short enough such that particle motion during the strobe-pulse duration can be neglected. The waiting time between subsequent strobe pulses is chosen sufficiently long that each strobe pulse interacts with an entirely undisturbed section of guided atomic beam.

For ^{87}Rb, the scattering rate at saturation intensity (about 10^7 s^{-1}) corresponds to an average acceleration of $\sim 6 \times 10^4$ m/s^2 for atoms resonant with the probe light. Assuming that an atom starts from rest, its displacement during the 20 μs long detection pulse is ≤ 12 μm. Because this displacement is much smaller than the atomic-beam diameter (about 200 μm), atomic-motion-induced blurring can be neglected for strobed atomic-beam images. To obtain a high signal-to-noise ratio in the strobed fluorescence images, typically 1000 strobed images are accumulated (which takes only of order 1 second). The strength of the strobing technique becomes apparent by comparing the left (continuous) and right (strobed) panels of Fig. 3.1. The strobed image is not blurred in the direction transverse to the atomic flow and extends in an unabated manner over the whole length of the illuminated atomic-flow segment.

3.1.3 Influence of Zeeman Effects

In a high-gradient magnetic guide such as ours, atoms are tuned out of resonance from the probe laser frequency at distances of only a few tens microns away from the guide axis. Due to the spatial variation of Zeeman shifts, the number of closed-channel probe photons scattered per atom varies in a complicated manner throughout the detection region. The spatial variation in the number of probe photons scattered per atom becomes even more significant because of the position-dependence of the probe-beam intensity, the position-dependence of the angle between laser polarization and magnetic field, and optical pumping among magnetic sublevels. Consequently, fluorescence images produced by a strobed, monochromatic, closed-channel probe laser differ strongly from the density profile of cold atoms in the magnetic guide. Thus, it is highly impractical to extract the atomic density profile from the measured closed-channel fluorescence images.

3.2 Open-channel Imaging

3.2.1 Outline of the Method

The difficulties described in Sec. 3.1 are circumvented by using an imaging method that produces a constant photon yield per atom, independent of atom location and detailed laser parameters. The method relies on the use of an open-channel transition to probe the atoms. In the present case, in which ^{87}Rb atoms are traveling in the $|F = 1, m_{\mathrm{F}} = -1\rangle$ state, the open-channel transition is the $F = 1 \rightarrow F' = 2$ repump transition. An atom in $F = 1$ scatters a repump photon and decays into one of the two hyper-fine ground levels $F = 1$ and $F = 2$. If the atom decays into the $F = 1$ level, the scattering process is repeated. If the atoms decays into the $F = 2$ level, it ceases to scatter more probe photons because the $F = 2 \rightarrow F' = 2$ transition is 6.83 GHz red-detuned from the repump transition. In Sec. 3.2.2, we find that, on average, an atom scatters 2.5 photons before being transferred into the non-resonant $F = 2$ state, independent of laser intensity and Zeeman shift. To ensure a uniform photon yield throughout the atomic sample, we only require the excitation rate on the open-channel repump transition $F = 1 \rightarrow F' = 2$ to be $\gtrsim 2.5$ times the inverse imaging-pulse width (10^5 s^{-1} under the conditions of Fig. 3.1). Assuming an intensity of $10I_{\mathrm{sat}}$, where $I_{\mathrm{sat}} = 1.6$ mW/cm^2 is the saturation intensity, this condition is satisfied well for magnetic fields up to at least ~ 60 G. If the atomic distribution samples magnetic fields less than this value, as in Fig. 3.1, almost all atoms will have sufficient time to become optically pumped into the non-resonant $F = 2$ state during their interaction with the open-channel imaging pulse. Consequently, the photon yield per atom will be uniform throughout the atomic sample, and the fluorescence images will be proportional to the atomic distribution projected onto the image plane. The only disadvantage of this method is that the average yield of 2.5 photons per atom is quite low. Hence, a sensitive camera is required to detect the open-channel images.

3.2.2 Simulation

We have simulated the open-channel detection process of cold ^{87}Rb atoms in the $|F = 1, m_{\mathrm{F}} = -1\rangle$ state in the magnetic field generated by two parallel current-carrying wires (as in Fig. 3.2). Using the quantum Monte-Carlo wave function (QMCWF) technique [49], we simulate the time evolution of the atoms in a laser field tuned close to the $F = 1 \rightarrow F = 2$ open-channel probe transition. In the simulation, we include the ground state hyperfine levels $F = 1$ and $F = 2$ and the excited-state levels $F' = 0, 1$, and 2. The exact magnetic field of appropriately placed infinitesimally thin wires is used, resulting in a transverse gradient of 2.7 kG/cm at the minimum of the guiding potential, as shown in Fig. 3.2. Zeeman shifts are assumed to be linear throughout the detection region. For the ground-state manifold ($F = 1$, g-factor $g_{\mathrm{F}} = -1/2$), this approximation is very well satisfied due to the large hyperfine splitting (6.83 GHz) between $F = 1$ and $F = 2$. The coupled excited-state manifolds ($F' = 0$, 1, and 2 with $g_{\mathrm{F}'} = 2/3$) have separations of 72 MHz (between 0 and 1) and 157 MHz (between 1 and 2). Zeeman shifts of these F' levels are approximately linear for magnetic fields less than about 60 G, corresponding to radial displacements from the guide axis of $\rho \lesssim 220$ μm. As seen in Fig. 3.2, the atomic distribution is mostly contained within this radius. Within the region of interest, the approximation of linear Zeeman shifts is therefore valid not only for the $F = 1$ ground state, but also for the relevant excited states. As in the experiment, the polarization of the simulated open-channel imaging beam is linear, transverse to the guide wires, and in the plane spanned by the guide wires. The temperature of the guided atomic beam is low enough that Doppler shifts ($\lesssim 1$ MHz) are entirely negligible.

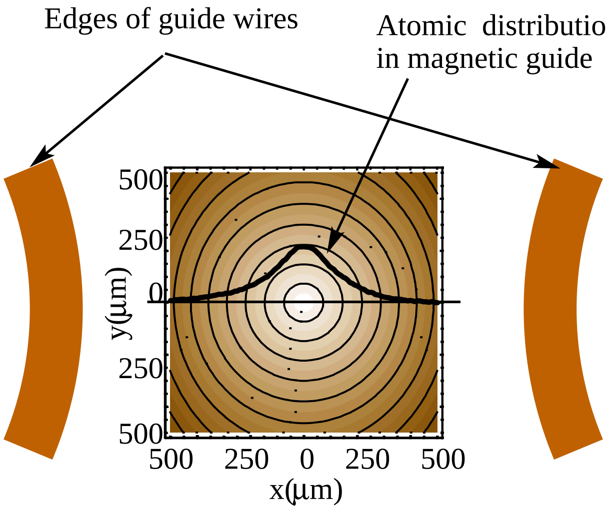

Figure 3.2: Contour plot of the magnetic field of the atom guide vs position (x, y). The contour lines show the transverse magnetic trapping field established by two parallel wires carrying parallel currents of 300 A. This establishes a field gradient of 2.7 kG/cm at the minimum of the guiding potential. The separation between adjacent contour lines is 20 G. Typical distributions of trapped atoms (overlaid curve) extend into regions with magnetic fields of order 50 G, corresponding to Zeeman shifts of order 70 MHz.

In the simulation, we average 500 quantum trajectories at each point on a uniform grid in a plane transverse to the magnetic-guide wires within the detection region. Each quantum trajectory is propagated until the atom is transferred from the $F = 1$ into the $F = 2$ sub-level, or until the simulation time reaches the end of the 20 μs imaging pulse. During the imaging pulse, the atoms are assumed to be stationary. The observables of primary interest are the average photon yield per atom and the probability that an atom is transferred into the $F = 2$ state, each as a function of position.

The results show that, for a sufficiently intense probe, atoms become transferred into the $F = 2$ state with near 100% probability, as can be seen in the right panel of Fig. 3.3. In a crude approximation, one may assume that in the simulated open-

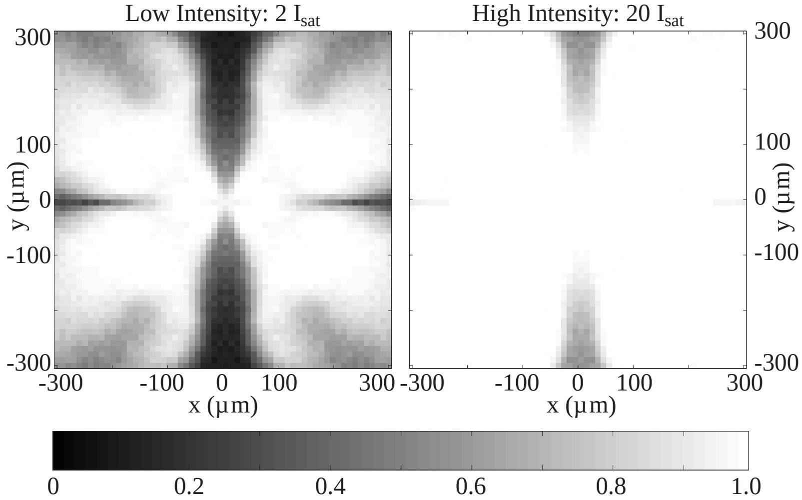

Figure 3.3: Probability that an atom is transferred into the $F = 2$ state during the 20 μs open-channel imaging pulse vs position (x, y), for probe intensities $2I_{\text{sat}}$ (left) and $20I_{\text{sat}}$ (right). The detection laser field is detuned by -15 MHz from the $F = 1 \rightarrow F = 2$ probe transition and is linearly polarized in x-direction. In the high-intensity case, it is apparent that nearly 100% transfer is achieved throughout the displayed spatial range. [50]

channel detection process the atoms are predominantly excited into the $F' = 2$ level. By summing over the transition probabilities, one can see that the decay probabilities from $F' = 2$ state into the ground hyperfine levels $F = 1$ and $F = 2$ are 50% each. Thus, neglecting off-resonant excitation into the $F' = 1$ and $F' = 0$ levels, the probability $P(n)$ that an atom scatters n photons while being transferred into the $F = 2$ ground state is $P(n) = 2^{-n}$. The average photon number then is expected to be $\langle n \rangle = \sum_{n=1}^{\infty} nP(n) = 2$.

However, the results from the simulation show that, for magnetic field magnitude $\gtrsim$ 30 G, the average number of photons required to optically pump atoms into the $F = 2$ ground state is larger than 2. This can be explained as follows. For higher magnetic field values, the magnetic sub-components of the $F = 1 \rightarrow F' = 2$ transition tune out of resonance due to Zeeman shifts, and photon scattering due to the $F = 1 \rightarrow F' = 1$ transition becomes more significant. The probability that an atom excited into the $F' = 1$ level decays back into the $F = 1$ ground state is 5 times

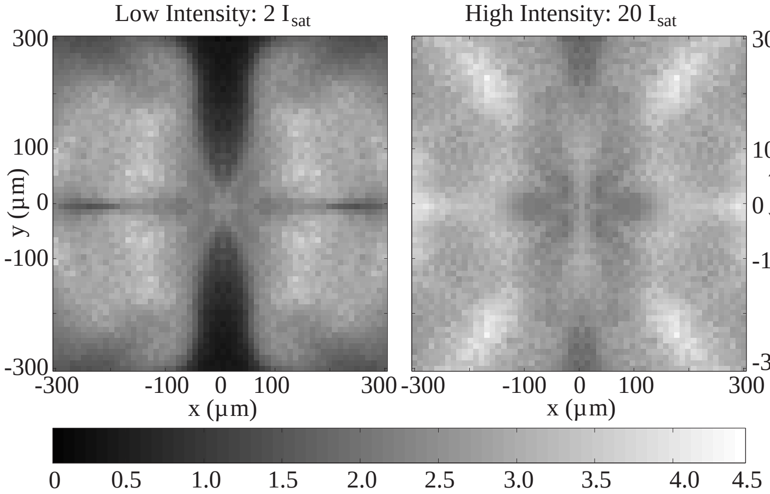

Figure 3.4: Simulated average number of photons vs position (x, y), scattered by magnetically trapped ^{87}Rb atoms illuminated by an open-channel imaging pulse of 20 μs duration and a constant intensity of $2I_{\text{sat}}$ (left) and $20I_{\text{sat}}$ (right). The imaging geometry used in the experiment corresponds to an observer located on the negative y-axis. The experimental signal corresponds to the product of the atomic density distribution and this type of plot integrated in the y-direction. [50]

greater than that of decaying into the $F = 2$ ground state. Thus, for higher magnetic fields, as the $F = 1 \rightarrow F' = 1$ transition becomes more important, an atom scatters more photons before becoming optically pumped into the $F = 2$ ground state. The simulation results shown in Fig. 3.4 indicate that for an atomic beam of ~ 200 μm diameter and $I = 20I_{\text{sat}}$, each atom scatters on average 2.5 photons, with a variation of less than ± 0.5 photons. Under these conditions, almost all atoms are optically pumped into the $F = 2$ ground state, as shown in the right panel of Fig. 3.3.

It is apparent in Figs. 3.3 and 3.4 that low illumination intensity results in a strong position dependence of the transfer efficiency and photon yield, respectively. The radial dependence is largely due to the increase of the Zeeman shift as a function of radial position in the magnetic guide. The structures present in the angular degree of freedom reflect the fact that the angle between laser polarization and the magnetic field varies throughout the detection region. This leads to variations in the relative importance of π, σ^+ and σ^- transitions and in optical pumping among the magnetic sublevels of $F = 1$.

Overall, the QMCWF simulations verify that for a sufficiently high probe intensity the open-channel imaging technique yields a nearly uniform number of photons per atom throughout the probe region. For trap-field-induced shifts of the open-channel probe transition $\lesssim$ 100 MHz and a imaging-pulse duration of 20 μs, the simulations show that an imaging-pulse intensity of 10 I_{sat} is sufficient.

3.2.3 Imaging Setup

The utilized imaging setup is shown in Fig. 3.5. A laser locked 15 MHz below the $F = 1 \rightarrow F' = 2$ transition provides both repumping light for laser-cooling as well as the open-channel probe light for imaging of the magnetically guided atoms. An acousto-optic modulator (AOM) in a double-pass configuration allows for fast switching of the imaging pulse. The probe beam is aligned through the AOM such that its frequency is not shifted during its on-phase, while a complete extinction is achieved during its off-phase (see bow-tie beam path through AOM in Fig. 3.5). The time interval between adjacent imaging pulses is chosen sufficiently long that each imaging pulse interacts with a completely undisturbed sample of the atomic beam. For the results presented here, 20 μs detection pulses are followed by waiting intervals ranging from 1 ms at low imaging-beam intensity to 4 ms at high intensity. The output of the AOM is passed through a single mode fiber and collimated to obtain a clean spatial Gaussian mode of about 5 mm diameter. This beam is then used to illuminate an aperture ≈1 mm in diameter. This filtering technique creates an approximate top-hat intensity profile immediately after the aperture. By imaging the plane of the aperture directly into the atomic beam, as indicated in Fig. 3.5, the intensity profile of the probe beam in the detection region also represents a top-hat profile, with minimal diffraction effects. Two benefits of this illumination method are that the intensity throughout the detection region is uniform and that scattering of probe light on the guide wires is minimized.

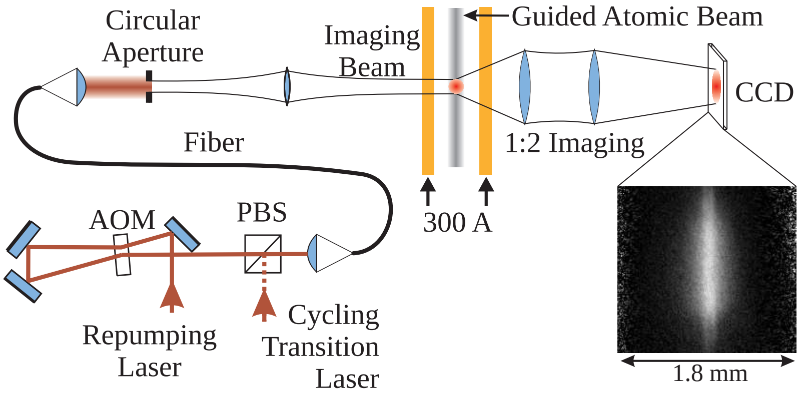

Figure 3.5: Imaging setup to probe the atomic beam. The imaging light first passes through an acousto-optic modulator (AOM) which provides fast switching for the imaging pulse. The pulsed imaging light is then passed through a fiber, collimated, and directed onto an aperture of ≈ 1 mm diameter. By imaging the aperture into the probe region of the magnetic guide, an approximate top-hat intensity profile of the imaging beam is achieved. Each probe pulse optically pumps the atoms from $F = 1$ into $F = 2$, thereby generating ≈ 2.5 photons per atom. This open-channel fluorescence is observed using a lens system that images the guided atomic beam onto a sensitive CCD camera with a 1:2 magnification ratio.

Because one probe pulse yields only ≈ 2.5 photons per atom emitted over a solid angle of 4π steradians, and because there are only about 9000 atoms in the probe volume, an efficient imaging of the atomic fluorescence is critical. The imaging system consists of two 2-inch diameter achromatic lenses with an object-side numerical aperture of 0.3 and magnification factor of 2. We further use a back-illuminated CCD (quantum efficiency ≈75% at 780 nm) from Andor Technology to detect the atomic fluorescence (Part number iXon DV-887 ECS BV). This CCD has an on-chip charge-amplifying gain element that enables near-single-photon detection capability.

3.2.4 Open-channel Imaging Results

In Fig. 3.6 we show a comparison between atomic-beam fluorescence profiles measured using either a closed-channel image or an open-channel image. The profiles are obtained by integrating images such as the ones shown in Fig. 3.1 along the

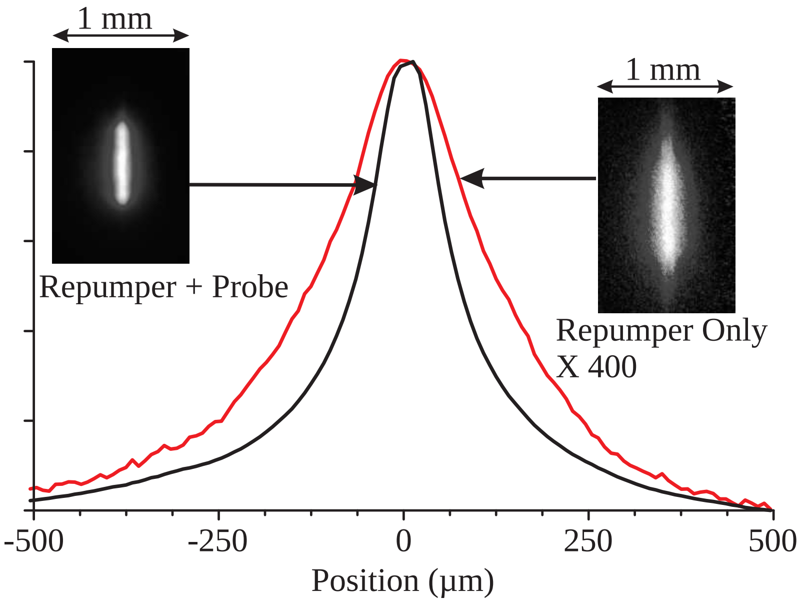

Figure 3.6: (Top Curve) Fluorescence profile of a magnetically guided beam of cold atoms obtained by open-channel ($F = 1 \rightarrow F' = 2$) fluorescence imaging. (Bottom curve) Corresponding fluorescence profile obtained by measuring fluorescence from the closed-channel $F = 2 \leftrightarrow F' = 3$ cycling transition.

atomic-beam direction, defined to be the z-axis (vertical axis in Fig. 3.1). In order to eliminate the influence of diffraction effects and of the circular shape of the illumination region on the beam profiles, the integration range is limited to a region in which the measured fluorescence does not significantly depend on z. While the closed-channel measurement in Fig. 3.6 has a high signal strength and a high signal-to-noise ratio, it does not reflect the true atomic distribution, as explained in Sec. 3.1.3. The open-channel profile in Fig. 3.6 reveals that the atomic-beam density profile is significantly wider than suggested by the closed-channel profile. Thus, Fig. 3.6 reiterates the advantages of using images obtained with an open-channel probe over those obtained with a closed-channel probe for determining atomic distributions. In the following, we demonstrate experimentally that for sufficiently high probe intensity, open-channel imaging provides fluorescence images that are approximately proportional to the underlying atomic-beam density profiles.

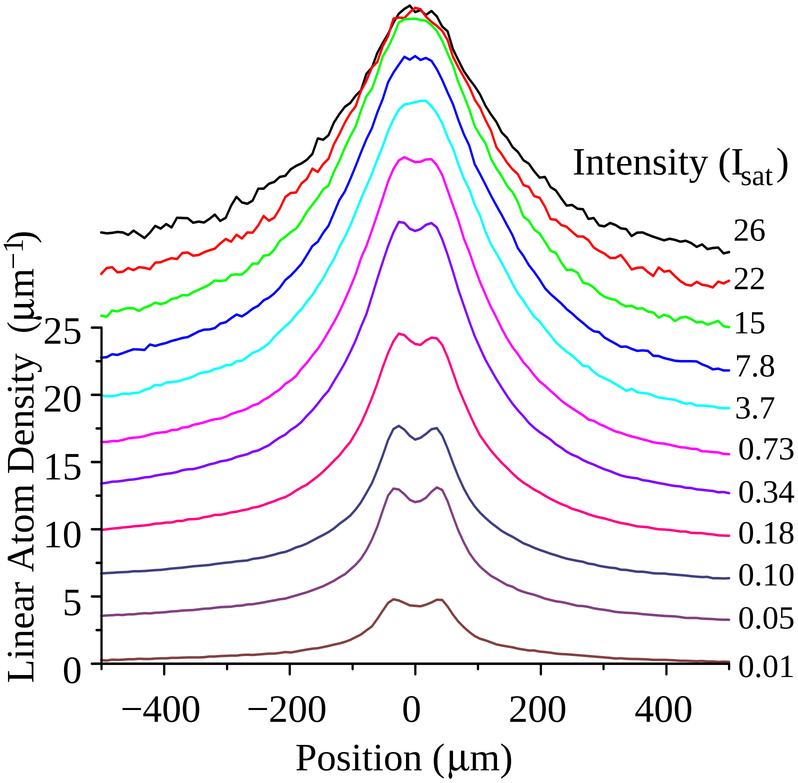

Figure 3.7: The linear density of detected atoms derived from fluorescence images obtained with the indicated intensities of the open-channel imaging laser. With increasing intensity, the profile converges towards the atomic density distribution. At high intensity, the noise level increases due to an increasing amount of stray light (which scales linear in intensity).

To obtain uniform photon yield in the magnetic guide, one must ensure that *all* atoms in the detection region are transferred into the $F = 2$ state during the probe pulses. This condition necessitates a sufficiently intense open-channel imaging pulse such that $\gamma\tau \gtrsim 2.5$ throughout the atomic sample, where γ is the photon scattering rate on the open-channel transition and τ is the duration of the detection pulse. In Fig. 3.7, we show the apparent linear atom density derived from open-channel fluorescence profiles for different imaging-laser intensities. In the conversion of fluorescence profiles into linear atom densities it is assumed that each atom isotropically scatters 2.5 photons on average. This means that, at low intensity, the atoms are actually under-counted because the average photon yield per atom is less than 2.5. The data shown in Fig. 3.7 demonstrates that with increasing probe intensity the open-channel image actually converges to an intensity-independent result, which approximately reflects the actual atomic distribution. In the measurement shown in Fig. 3.7, the open-channel imaging laser was slightly detuned from the atomic resonance for technical reasons. This detuning causes the open-channel imaging laser light to be resonant with an $F = 2 \rightarrow F' = 2$ transition at a distance of approximately 30 μm from the center of the trap. At low intensity, a combination of intrinsic scattering behavior and detuning results in a double-peak structure, as can be seen in Fig. 3.7 for $I \lesssim 1 I_{\text{sat}}$. As the imaging-beam intensity and thus the scattering rate γ increase, the double-peak structure disappears, while the linear density of counted atoms converges towards a limiting distribution which is identified with the atomic density distribution. In Fig 3.7, the atomic-beam profile is seen for intensities $I \gtrsim 5 I_{\text{sat}}$.

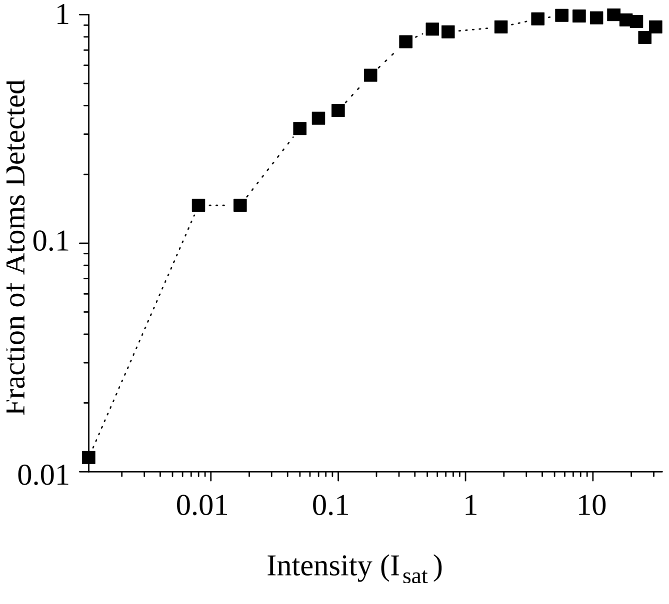

Figure 3.8: Fraction of atoms detected as a function of the intensity of the open-channel imaging pulse. The data are obtained by integrating the curves in Fig. 3.7 and by normalizing with the result obtained in the high-intensity limit (which corresponds to 9000 atoms).

The integrals of the profiles in Fig. 3.7 equal the total number of atoms counted in the detection volume. As shown in Fig. 3.8, the fraction of atoms detected increases as the intensity of the probe pulse is increased. The detected fraction saturates around $5I_{\text{sat}}$, indicating that under this condition all atoms become optically pumped from the $F = 1$ to the $F = 2$ ground state and deliver, on average, 2.5 photons each. On the plateau, the open-channel imaging is fully effective throughout the probe volume. Based on this conclusion and using appropriate calibration procedures, we find that the plateau in Fig. 3.8 corresponds to 9000 atoms present in the detection volume.

3.3 Summary

To summarize, in this chapter we have presented the characterization of an open-channel detection technique for measuring atomic distributions in high-gradient magnetic traps. This technique does not require the trapping field to be switched off and therefore is most useful for static-field traps. This technique is easy to implement in any existing imaging setup and can also be generalized to traps that involve both electric and magnetic fields, as well as AC electric-dipole traps (far-off-resonant laser traps). In the following chapter, we present the results of using this technique for characterizing the cold atomic beam in the atom guide.

CHAPTER IV

High-Gradient Atomic Guide Results

In this chapter, we set forth the characterization of a continuous cold atomic beam, the experimental apparatus of which is described in Ch. II. We begin with the unguided atomic beam used to inject atomic flux into the magnetic guide. Using absorption measurements, we characterize the temperature, velocity, and flux of the primary atomic beam. A similar absorption scheme allows us to further measure the output flux of the MMOT (at the beginning of the magnetic guide injection stage). Proceeding to the guided atomic beam, we give temperature, velocity, and flux measurements just before the 90° bend (1.7 kG/cm) as well as at the end of the 1.7 m long guide (2.7 kG/cm). This chapter will conclude with the results of an energy-selective atom filter, enabled via a continuously applied radio-frequency current.

4.1 Characterization of the Unguided Atomic Beam

4.1.1 Primary Atomic Beam

To characterize the unguided beam emitted from the PMOT, we have performed a series of absorption measurements. As depicted in Fig. 4.1, a low-intensity ($\sim 0.15\, I_{\mathrm{sat}}$ with saturation intensity $I_{\mathrm{sat}} = 1.6\,\mathrm{mW/cm^2}$), small-diameter, near-resonant probe beam was arranged to intersect the PMOT atomic beam at an angle $\theta = 45°$

in the vicinity of the MMOT. The spatial profile of the PMOT atomic beam was determined by measuring the absorption for different vertical positions of the probe beam. To determine the velocity distribution, for each vertical position y the probe laser was scanned across the atomic absorption resonance, and the absorption was measured as a function of the laser frequency. Due to the Doppler effect, the laser detuning from resonance $\delta\nu$ and the velocity of the atoms v_{z} are approximately related by $\delta\nu = \frac{v_{\mathrm{z}}}{\lambda}\cos\theta$. This allows us to plot the absorption due to the PMOT atomic beam as a function of vertical position and velocity. The data, shown in Fig. 4.2, yield an average velocity of the primary atomic beam $\langle v_{\mathrm{z}}\rangle = 22$ m/s and a FWHM spread of Δv_{z} =16 m/s. The FWHM spread of the absorption signal in height is Δy =16 mm. Since the distance between the PMOT and the MMOT is about 16 cm, the full angular spread of the primary beam is about 100 mrad.

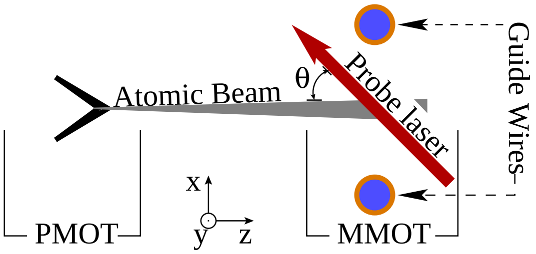

Figure 4.1: Setup of absorption measurement used in order to characterize the (un-guided) primary atomic beam emitted by the PMOT. The current in the guide wires is turned off for this measurement.

The flux Φ_{PMOT} of the atomic beam is determined as follows. In the limit of weak absorption, the absolute power $dP(y,\nu_{\mathrm{L}})$ absorbed by the PMOT atomic beam from the small probe beam is given by

$$\begin{aligned} dP(y,\nu_{\mathrm{L}}) &= -h\nu_{\mathrm{L}}\int_{-\infty}^{\infty} N(y,v_{\mathrm{z}})\gamma(v_{\mathrm{z}},\nu_{\mathrm{L}})dv_{\mathrm{z}} \\ &= -h\nu_{\mathrm{L}}\int_{-\infty}^{\infty} N(y,v_{\mathrm{z}})\frac{\Gamma}{2}\left(\frac{I/I_{\mathrm{sat}}}{1+4\left(\frac{2\pi\delta}{\Gamma}\right)^2}\right)dv_{\mathrm{z}} \end{aligned} \tag{4.1}$$

where ν_{L} is the laser frequency, γ_{p} is the velocity- and frequency-dependent photon scattering rate, Γ is the line width ($2\pi \times 6$ MHz), I is the laser intensity, and $I_{\rm sat} = 1.6\,{\rm mW/cm^2}$. $N(y, v_{\rm z})$ is the number of atoms in the probe beam per velocity element $dv_{\rm z}$ at height y. The dependence of dP on $\nu_{\rm L}$ is also contained in the atom-field detuning δ seen by the atoms,

$$\delta = \frac{\cos(\theta)}{\lambda} v_{\rm z} + \nu_0 - \nu_{\rm L} \tag{4.2}$$

where ν_0 is the un-shifted frequency of the atomic transition. Noting that the probe-beam diameter is much smaller than the atomic-beam diameter, the fractional absorption $dP(y, \nu_{\rm L})/P$ is

$$\begin{aligned} \frac{dP(y,\nu_{\rm L})}{P} &= -\frac{h\nu_{\rm L}\Gamma}{2I_{\rm sat}} \int_{-\infty}^{\infty} \left(\frac{N(y,v_{\rm z})}{A}\right) \frac{1}{1+4\left(\frac{2\pi\delta}{\Gamma}\right)^2} dv_{\rm z} \\ &= -\frac{h\nu_{\rm L}\Gamma}{2I_{\rm sat}} \int_{-\infty}^{\infty} \left(\frac{n_{\rm A}(y,v_{\rm z})}{\sin(\theta)}\right) \frac{1}{1+4\left(\frac{2\pi\delta}{\Gamma}\right)^2} dv_{\rm z} \end{aligned} \tag{4.3}$$

where δ is defined in Eq. 4.2 and A is the probe-beam cross section and $n_{\rm A}(y, v_{\rm z})$ is the number of atoms per area element $dydz$ and per velocity element $dv_{\rm z}$, *i.e.* $n_{\rm A}$ has units of ${\rm m^{-2}(m/s)^{-1}}$. Using the reasonable assumption that $n_{\rm A}(y, v_{\rm z})$ does not vary much over the velocity range over which the second factor under the integral in Eq. 4.3 is significant, we may replace $n_{\rm A}(y, v_{\rm z})$ by $n_{\rm A}(y, v_{\rm R})$, where

$$v_{\rm R} = \frac{\lambda}{\cos\theta}(\nu_{\rm L} - \nu_0) \tag{4.4}$$

is the velocity of atoms for which the probe laser beam is on-resonant,*i.e.* for which $\delta = 0$ in Eq. 4.2. The integral can then be calculated, yielding

$$n_{\rm A}(y, v_{\rm R}) = -\frac{dP(y, \nu_{\rm L}(v_{\rm R}))}{P} \frac{4I_{\rm sat}\sin(2\theta)}{hc\Gamma^2} \tag{4.5}$$

Denoting the peak absorption by $(dP/P)_0$ and the peak value of $n_{\rm A}$ by n_0, it is $n_0 = -(dP/P)_0\, 4I_{\rm sat}\sin(2\theta)/hc\Gamma^2$. Noting that the volume density of atoms $n_{\rm V} \approx$

$n_0 \Delta v_z / \Delta x$, where $\Delta\Box$ indicates the FWHM value of $\Box$, and assuming that the PMOT atomic beam is symmetric about its axis (i.e. the FWHM spreads of the atomic beam $\Delta x = \Delta y$), the estimated atomic flux is

$$\begin{aligned} \Phi_{\mathrm{PMOT}} \approx & \; n_{\mathrm{V}}\, \Delta x \, \Delta y \, \langle v_z \rangle \\ = & \; n_0 \, \Delta v_z \, \Delta y \, \langle v_z \rangle \\ = & -\frac{4 I_{\mathrm{sat}}}{hc\Gamma^2} \left(\frac{dP}{P} \right)_0 \Delta v_z \, \Delta y \, \langle v_z \rangle \, , \end{aligned} \tag{4.6}$$

where $\theta = \pi/4$ has been used. Using the measurement result $(dP/P)_0 = -0.22\%$ and the above values for the average velocity, the velocity spread and the height of the PMOT beam, we find $\Phi_{\mathrm{PMOT}} \approx 3 \times 10^9$ s^{-1}. Due to the approximations made for Eq. 4.5 and in Eq. 4.6, we expect the result to be accurate to within 30% of the stated value. It was also observed that the flux for higher PMOT laser powers was higher. For example, a PMOT laser power of 130 mW resulted in a flux of around $5.3 \times 10^9 \mathrm{s}^{-1}$.

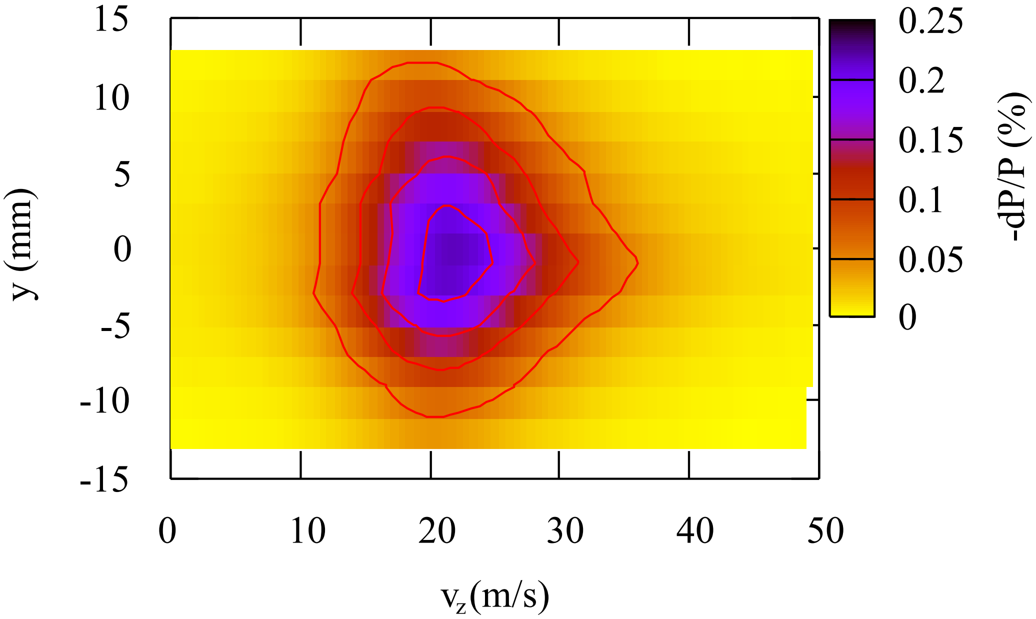

Figure 4.2: Contour plot of the relative absorption $-dP/P$ due to the primary atomic beam as a function of vertical position y and velocity v_z.

4.1.2 Injection into the Guide

An absorption scheme similar to the PMOT characterization was implemented to determine the performance of the MMOT as a function of detuning and gradient. In this case, because of limited optical access the probe beam had to be aligned perpendicular to the atomic flow and the guide field naturally had to be on. While these boundary conditions prevented us from measuring the velocity distribution, the output flux of the MMOT could be determined using the method explained in the following.

A low-power ($\sim 0.15\ I_{\mathrm{sat}}$), circularly polarized probe laser beam was aligned to intersect the topmost portion of the MMOT, just before the extraction zone. The diameter of the probe was made appreciably larger than the diameter of the atom flow in the MMOT. The MMOT was run in a pulsed fashion in which the MMOT light was on for 88 ms. During this time, the probe laser was off and atoms were cooled into the moving reference frame of the MMOT until steady-state conditions were reached. After the MMOT light was switched off, the probe laser was turned on and the relative absorption dP/P observed immediately after the turn-on of the probe was recorded. This procedure was repeated for different probe-laser frequencies ν_{L}.

For simplicity, we first consider the case where Zeeman effects can be neglected. In this case, the absolute power dP absorbed from the probe laser is, in the limit of weak absorption, given by

$$dP = -N\gamma h\nu_{\mathrm{L}} = -N\frac{\Gamma}{2}\frac{I/I_{\mathrm{sat}}}{1+4\left(\frac{2\pi\delta}{\Gamma}\right)^2}h\nu_{\mathrm{L}}. \tag{4.7}$$

where N is the number of atoms in the probe beam and $\delta = \nu_{\mathrm{L}} - \nu_0$ is the frequency detuning of the probe laser from the atomic resonance. Noting that $I = P/A$, where

A is the area of the circular probe beam, rearranging Eq. 4.7 gives

$$\frac{dP}{P} = -\frac{N}{A}\left(\frac{\Gamma h\nu_{\mathrm{L}}}{2I_{\mathrm{sat}}}\right) = -n_{\mathrm{l}}\left(\frac{\Gamma h\nu_{\mathrm{L}}}{I_{\mathrm{sat}}\pi r}\right) \tag{4.8}$$

where $A = \pi r^2$, $n_{\mathrm{l}} = N/(2r)$ is the linear number density of atoms, and r is the probe-beam radius. Thus, the number of atoms emitted from the MMOT per second is given by

$$\Phi_{\mathrm{MMOT}} = n_{\mathrm{l}} v_{\mathrm{MMOT}} = \left(-\frac{dP}{P}\right)\left(\frac{I_{\mathrm{sat}}\pi r}{\Gamma h\nu_{\mathrm{L}}}\right) v_{\mathrm{MMOT}}.$$

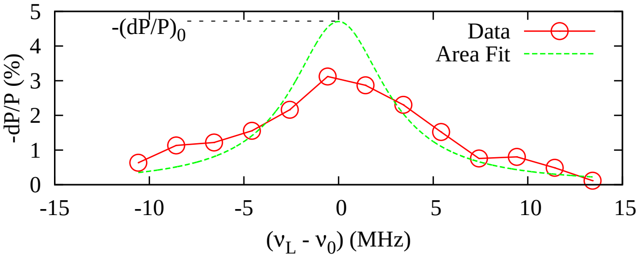

Figure 4.3: Relative absorption $-dP/P$ of a probe beam passed through the atomic beam exiting the MMOT vs the frequency detuning of the probe laser $\nu_{\mathrm{L}} - \nu_0$. The red circles show measured data, while the green line shows a Lorentzian of 6 MHz FWHM that has the same area as the data curve.

Because the MMOT magnetic fields were actually on during the probe pulse, the peak absorption $(dP/P)_0$ is reduced due to line broadening caused by the Zeeman effect. To account for this effect, the following procedure was used. The relative absorption (dP/P) observed immediately after turn-on of the probe pulse was measured as a function of the probe-laser detuning $\delta = \nu_{\mathrm{L}} - \nu_0$ (circles in Fig. 4.3). While the Zeeman effect moderately broadens the absorption line, it does not significantly affect the integral of the absorption line because the Larmor frequency of the atoms ($\lesssim$ 500 kHz) is of the order or less than the optical-pumping rate of the probe laser ($\sim$2 MHz on-resonance, under the conditions used). Therefore, the absorption signal that would be measured if the magnetic field were off is given by a Lorentzian with 6 MHz FHWM linewidth and an area equal to that of the measured absorption line. This Lorentzian is shown by the dashed line in Fig. 4.3. The output flux of the MMOT is obtained by inserting the peak value of the Lorentzian ($-(dP/P)_0$ in Fig. 4.3) into Eq. 4.9. Typically obtained MMOT flux values are $\Phi_{\rm MMOT}(v_{\rm MMOT} = 2.2~{\rm m/s}) = 5.4 \times 10^8~{\rm s}^{-1}$ and $\Phi_{\rm MMOT}(v_{\rm MMOT} = 2.5~{\rm m/s}) = 4.8 \times 10^8~{\rm s}^{-1}$ for a MMOT field gradient of $\partial B/\partial\rho \approx 20$ G/cm. Because of the uncertainty of the area under data curves like that shown in Fig. 4.3, we estimate the uncertainty of these flux values to be about 30%. The results indicate that the transfer efficiency from the primary PMOT atomic beam into the cold, concentrated beam emitted by the MMOT is 16% to 18%. Further, the quoted MMOT flux values are a sum over all magnetic sublevels of the output atoms.

For MMOTs operated with gradients of $\partial B/\partial\rho = 15$ G/cm (225 A guide current) and $\partial B/\partial\rho = 10$ G/cm (150 A) we find MMOT flux values that are $\sim 90\%$ and $\sim 60\%$ of the above quoted ones, respectively. We further find that while the average detuning ($\delta_{\rm MMOT}$) of our MMOT laser beams from resonance is typically of order two line-widths, the MMOT output flux does not vary significantly over a range of $-2.5\Gamma \lesssim \delta_{\rm MMOT} \lesssim -1.5\Gamma$.

4.2 Atomic-beam Analysis before Waveguide Bend

4.2.1 Measurement of the Transverse Temperature

In the following, we use the term "temperature" in order to quantify the velocity spread of the atoms, even though the collision rate is too small to establish a local thermal equilibrium in the atom flow. This deliberate use of the term temperature is common in laser-cooling applications.

The most direct method to measure the transverse temperature is to only use repumper light in the probe region, with an intensity exceeding about one saturation intensity of the cycling transition ($I_{\rm sat} = 1.6$ mW/cm^2). The duration of the strobe intervals (20 μs) is sufficiently long that all atoms inside the detection volume scatter of order two repumper photons and become optically pumped into the $F = 2$ state. Notably, this even applies to the atoms traveling in the wings of the atomic flow, which experience the largest Zeeman shifts. Each atom in the probe volume therefore produces the same amount of fluorescence signal during detection, independent of the magnetic field at which the atom is located. Due to this uniformity of the signal obtained per atom, images obtained with only repumper light are proportional to the atomic-flow density projected onto the image plane. This property makes repumper-only images particularly easy to analyze. A slight disadvantage of repumper-only images is that the low total photon yield per atom, only of order two, leads to dim images.

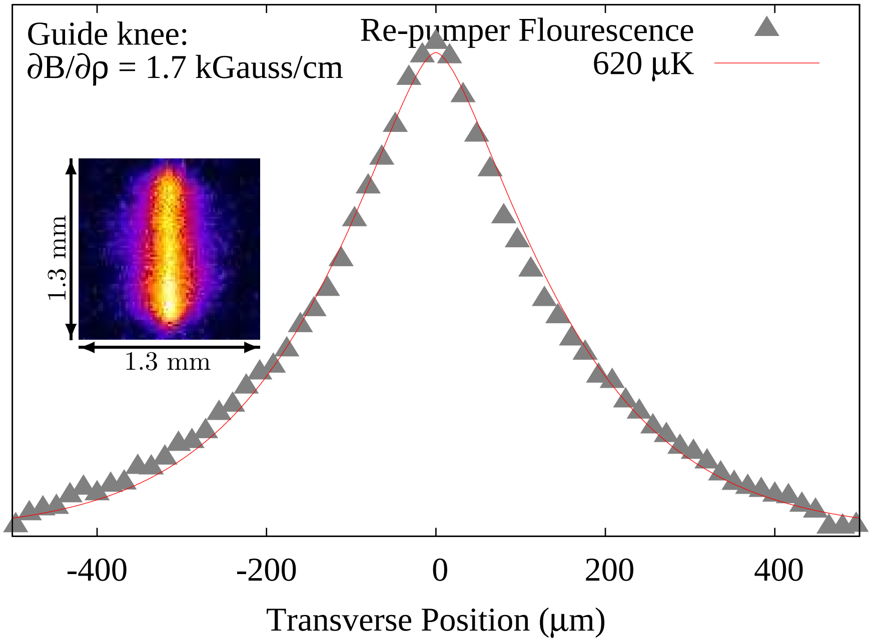

Figure 4.4: Atomic-beam image (inset) and corresponding profile transverse to the guide axis (data points). The image is obtained at a location just below the atom-guide knee with repumping light only. In the image, the guide axis is vertical. The line through the data points represents a fit for a temperature of 620 μK.

A typical repumping-only fluorescence image and its profile are displayed in Fig. 4.4.

Assuming a thermal distribution in the degrees of freedom x and y transverse to the guide axis, the profile data can be fitted with a function

$$P(x) \propto \int_{-\infty}^{\infty} \exp\left[-\frac{V_{\mathrm{B}}(x,y)}{k_{\mathrm{B}}T_{\perp}}\right] dy \tag{4.9}$$

where the magnetic-dipole potential $V_{\mathrm{B}}(x,y) = \frac{1}{2}\mu_{\mathrm{B}}B(x,y)$, and μ_{B} is the Bohr magneton. $B(x,y)$ is the exact magnetic field for a pair of infinitesimally thin wires separated by the center-to-center distance of the guide wires. A small longitudinal component ($\gtrsim$ 200 kG) generated by a combination of the Earth's magnetic field and other environmental fields is also present. The transverse temperature $T_{\perp}$ is the fit parameter of interest. The data in Fig. 4.4 are fit best with $T_{\perp} = 620\ \mu\mathrm{K} \pm 15\ \mu\mathrm{K}$.

If the atoms are illuminated with both repumper and probe light, the fluorescence on the cycling transition entirely dominates the photon yield per atom. Using a probe intensity of order ten saturation intensities, atoms located at a magnetic field, at which the applied probe light is resonant with the cycling transition, scatter of order 300 photons during a 20 μs strobe pulse. By detuning the frequency of the probe light, the 1.4 MHz/G Zeeman shift of the cycling transition $|F = 2, m_{\mathrm{F}} = 2\rangle \rightarrow |F' = 3, m'_{\mathrm{F}} = 3\rangle$ manifests itself as shown in Fig. 4.5: for zero detuning of the probe laser from the field-free transition frequency, the measured fluorescence is primarily from atoms traveling very close to the guide axis, where the magnetic field is low. For significant detunings, the images mostly show atoms traveling at a large distance from the guide axis where the magnetic field is such that the cycling transition is resonant. The signal from these outlying atoms depends strongly on the polarization of the probe light. To balance optical pumping effects on both sides of the guide axis in the image plane, a linear probe light polarization was used. Taking multiple atomic-beam profiles at different detunings (and equal intensities), the *envelope* of the entire set of curves gives a representation of the transverse extension of the atomic beam. Assuming a thermal distribution in the transverse degrees of freedom, the transverse temperature $T_\perp$ can be determined by fitting the envelope to the function

$$P_{\mathrm{E}}(x) \propto \int_{-\infty}^{\infty} w(x,y) \exp\left[-\frac{V_{\mathrm{B}}(x,y)}{k_{\mathrm{B}}T_\perp}\right] dy \tag{4.10}$$

where $w(x,y)$ is the position-dependent number of photons scattered per atom. For a linear probe-laser polarization transverse to the guide axis, the probed atoms tend to be optically pumped into the magnetic sublevels $|F=2, m_{\mathrm{F}}=\pm 2\rangle$ (quantization axis parallel to the laser direction). Thus, approximately half of the probe-light intensity I drives the atoms on the cycling transition, and $w(x,y)$ is given by

$$w(x,y) = \frac{\Gamma}{2}\frac{s}{(s+1)}\tau \tag{4.11}$$

where Γ is the excited-state decay rate ($2\pi \times 6$ MHz), τ is the strobe interval, s is given by

$$s = \frac{I}{2I_{\mathrm{sat}}}\frac{1}{1+4\left(2\pi\delta(x,y)/\Gamma\right)^2}, \tag{4.12}$$

and

$$\delta(x,y) = \frac{\mu_{\mathrm{B}}}{h}\left(B(x,y) - B(x,0)\right) \tag{4.13}$$

is the detuning of the probe laser from the Zeeman-shifted atomic resonance at the location $(x,0)$. Note that the fitting function in Eq. 4.10 does not represent a profile for a single laser frequency. Rather, Eq. 4.10 represents the envelope of the peaks from a set of profiles obtained with different laser frequencies. Using fit functions of the type in Eq. 4.10, the envelope of the data in Fig. 4.5 is found to correspond to a transverse temperature $T_\perp \approx 420$ μK.

In all measurements where the frequency of the probe laser was varied and the temperature $T_\perp$ was obtained by fitting the envelope of the peaks in the fluorescence

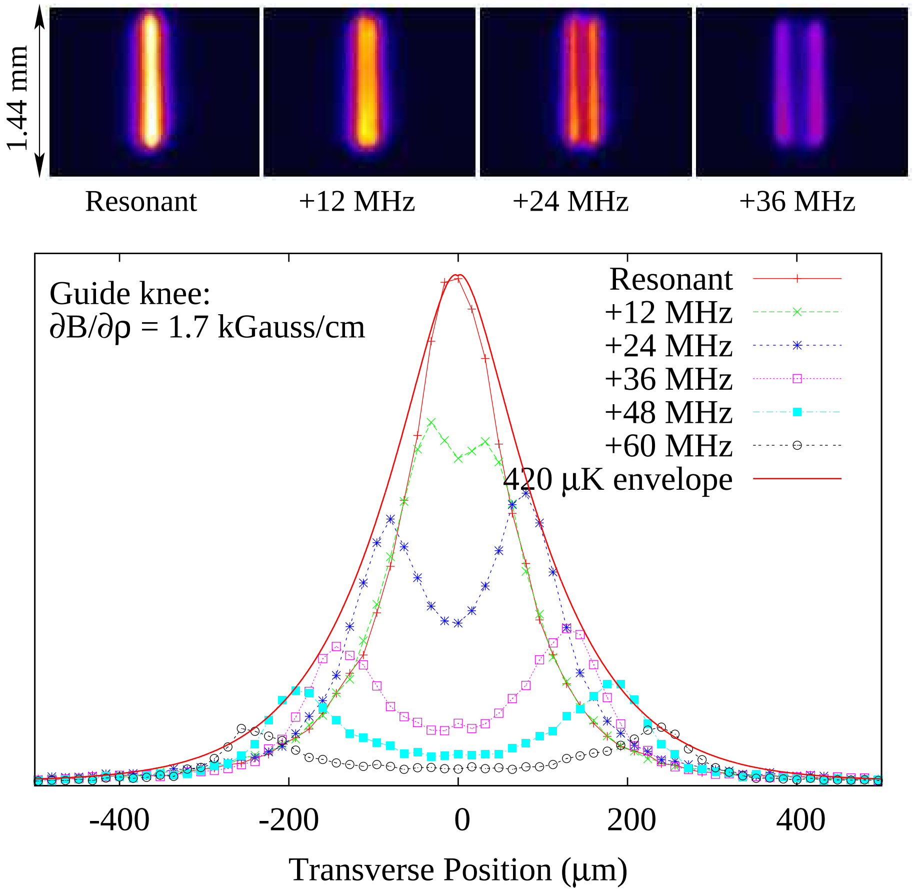

Figure 4.5: Top row: Atomic-beam images with both repumper light and probe light present in the detection region for the indicated detunings of the probe laser relative to the field-free transition frequency. The images are obtained at a location just below the atom-guide knee and with a horizontal linear polarization of the probe laser. In the images, the guide axis is vertical. Lower panel: Profiles of atomic-beam images transverse to the guide axis for the indicated detunings of the probe laser relative to the field-free transition frequency. By fitting the *envelope* of the profiles with curves of the type Eq. 4.10, a transverse temperature of $T_\perp \approx 420\ \mu$K is obtained.

profiles (such as in Fig. 4.5), the fit results for $T_\perp$ were notably lower than those found using the repumper-only scheme. This discrepancy is explained as follows. Since the repumper frequency was not detuned with the probe, the repumping rates in the wings of the atomic beam were notably lower than those near the core of the atomic distribution. Thus, atoms in the wings require a significant fraction of the probe-pulse duration to become repumped, and produce less net fluorescence on the cycling transition than atoms traveling near the guide center. This effect leads to systematically reduced values for $T_\perp$ in the temperature fits. Therefore, temperatures obtained using the repumper-only scheme (as in Fig. 4.4) are considered more reliable than those obtained with the probe-repumper scheme (as in Fig. 4.5).

4.2.2 Measurement of the Longitudinal Temperature

To determine the longitudinal temperature of the guided atomic beam, we have performed a time-of-flight analysis. This was done by observing the turn-on behavior of the atomic-beam density after a sudden enhancement of the atom flow out of the MMOT. The atomic flow is suddenly enhanced by about a factor of five by turning on the depumping beam located in the MMOT exit region. The data were obtained by varying the time over which the atomic-beam fluorescence is integrated. Data sets for two different launch velocities, displayed in Fig. 4.6, show that the signal varies linearly with integration time until the enhanced atomic flow reaches the probe region, at which point the slope changes due to the increase in atomic flux. The time-of-flight distribution is obtained by differentiating the curves shown in Fig. 4.6 twice.

Neglecting magnetic retardation effects [40] in the compression region of the magnetic guide, it is straightforward to convert the time-of-flight curves in Fig. 4.6 into a distribution of velocities at the observation point. The corresponding estimate for the longitudinal temperature $T_{\|}$ of the atoms is found to be $T_{\|} \sim 900$ μK. Since the retardation depends on the transverse energy distribution [40], it broadens the time-of-flight signal relative to the signal one would obtain without retardation. Thus, the estimate $T_{\|} \sim 900$ μK provides an upper limit of the actual value $T_{\|}$. We have performed simulations in which the exact guide fields were used and thus retardation effects were fully accounted for. Assuming MMOT temperatures $T_{\|} = 300$ μK and $T_{\perp} = 250$ μK ($T_{\perp} = 150$ μK is the Doppler limit for Rb), the simulations yield $T_{\|} = 890$ μK in the probe region, which is compatible with the experimentally

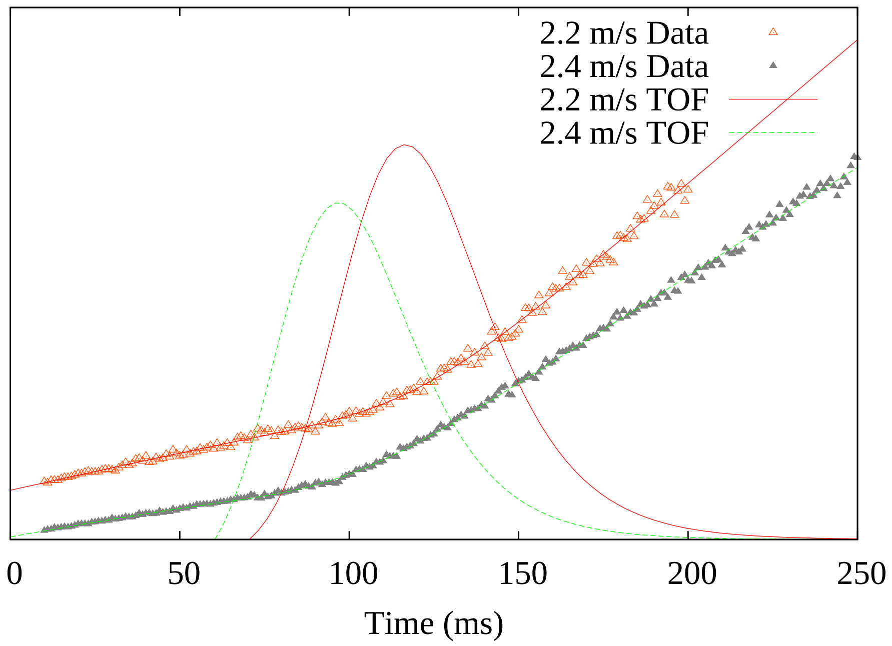

Figure 4.6: Time-of-flight experiment in the vertical launch section. The time-integrated atomic-beam fluorescence (triangles) is shown vs the integration time for the indicated launch velocities. At time zero, the atomic flux out of the MMOT is suddenly increased by about a factor of five. The time-of-flight distributions (curves peaking at about 100 ms) are obtained by twice differentiating the smoothed curves laid through the data points.

obtained upper limit.

It is noted that in our current MMOT configuration a value of $T_\perp$ greater than the Doppler limit is expected. Images of the MMOT, such as those shown in Fig. 2.5, typically show incomplete narrowing of the atomic beam at the extraction point of the MMOT. As discussed in Sec. II.2.2.3, this observation indicates less than optimal cooling in the transverse directions.

4.2.3 Ballistic Heating and Magnetic Retardation

In discussing the temperature change from the MMOT region, through the magnetic compression region, and into the narrow magnetic guide, it is helpful to discuss the adiabatic heating mechanism known as ballistic heating. For the sake of a qualitative discussion, consider a one-dimensional case where a small group of atoms are

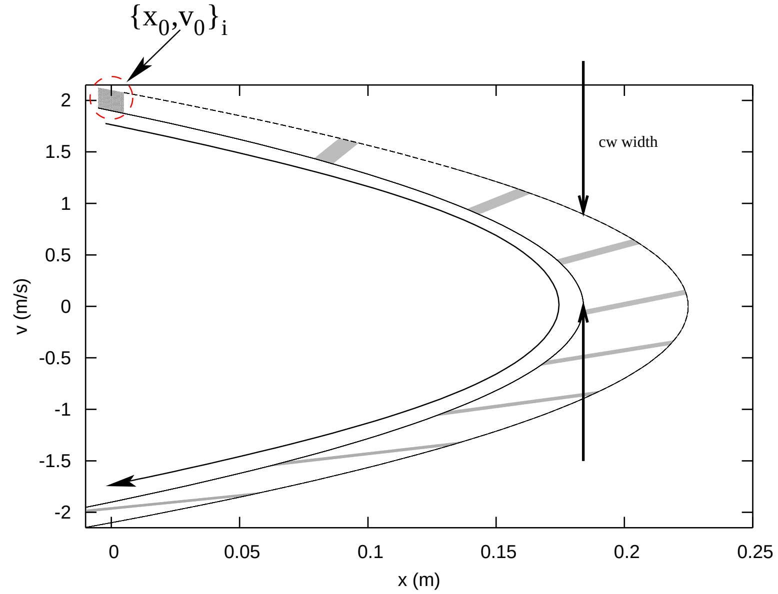

Figure 4.7: One dimensional Hamiltonian evolution of a small phase space element under gravity. Each point in the initial element, indicated by $\{x_0, v_0\}_\mathrm{i}$, has a positive initial velocity and is launched near $x = 0$. It is clear from this figure how, although the area of the single element is conserved through the motion, its shape is drastically changed. For the case of a continuously launched source, particles at a given location will have been launched from differing starting times. The vertical arrows in the figure indicate the increase in the width of the velocity distribution measured from a continuously launched source.

launched vertically against gravity. The initial velocity and position of these atoms are such that a small rectangular element of phase space is represented. As shown in Fig. 4.7, the atoms are slowed under gravity until they eventually turn around and fall back through the $x = 0$ position. During this process, the packet spreads monotonically in space. Because of this spread and the conservation of phase space (as expressed by Liouville's theorem), at any one fixed position that cuts through the packet, the velocity distribution becomes narrower. In other words, the temperature at a fixed distance away from the center of mass of the packet appears to decrease. Contrarily, if one observes a continuously launched beam (rather than just a packet) at some fixed position above the launch region, such as in the experiment described in this thesis, the temperature increases rather than decreases. This effect can easily be extracted from Fig. 4.7. At the probe location indicated on the figure, the atomic beam will be comprised of atoms launched at various times. As a result, the detected velocity distribution will be much wider than that detected from a single packet. Ballistic heating is therefore only observed when considering a continuous stream of atoms through a system.

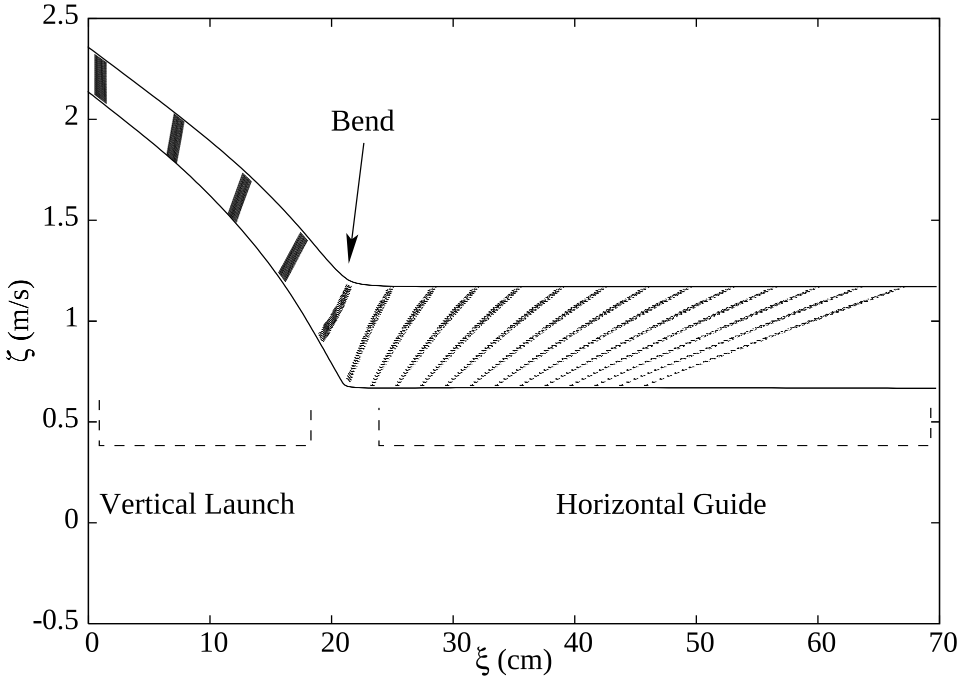

Figure 4.8: Evolution of a phase space element ($(\Delta v)_0 = 20$ cm/s, $(\Delta x)_0 = 1$cm) through the launch section of the atom guide and over the bend. ζ denotes the projection of the velocity into the direction tangential to the guide wires and ξ denotes the propagation length in the guide. In this case, the atoms are launched at the minimum of the field with zero energy in the transverse degrees of freedom. Similar to Fig. 4.7, a continuous beam monitored as some location after the bend shows a significant increase velocity distribution width.

As a nearly analogous example tailored to the geometry of our atom guide, a similar element of phase space is launched (in a simulation) at the minimum of the magnetic field at the location of the MMOT extraction point. Fig. 4.8 shows the evolution of the phase space element launched from the minimum of the magnetic field at the extraction point of the MMOT. The variable ξ denotes the propagation length in the guide, whereas ζ represents the projection of the velocity into the local direction of the atomic stream. An obvious difference between Figs. 4.8 and 4.7 is that those in Fig. 4.8 do not fall back to $\xi = 0$. Rather, the atoms in this simulation were given enough longitudinal energy to transition into the horizontal section of the guide.

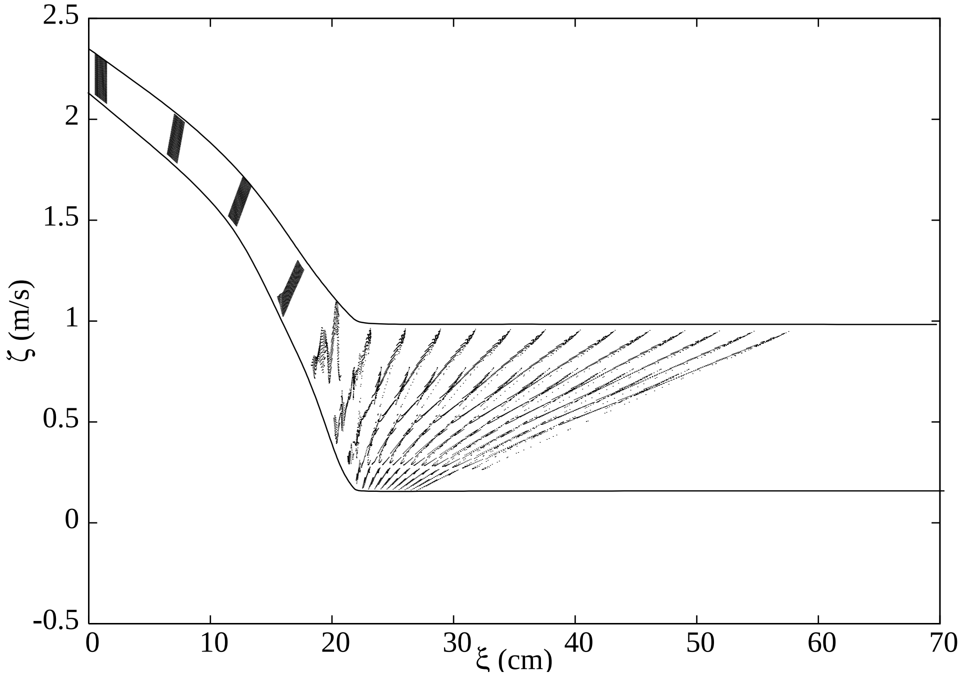

Figure 4.9: Evolution of a phase space element ($(\Delta v)_0 = 20$ cm/s, $(\Delta x)_0 = 1$cm) through the launch section of the atom guide and over the bend. ζ denotes the projection of the velocity into the direction tangential to the guide wires and ξ denotes the propagation length in the guide. In this case, the atoms are launched at the minimum of the field with one of the transverse velocities set to 15 cm/s. Additional retardation from the magnetic compression is evident by the lower velocities in the horizontal guide. The differential nature of this additional retardation force (dependence on the transverse excursion) causes even more heating than for the case shown in Fig. 4.8. The discontinuities in the bend region are due to the incomplete decoupling between the longitudinal and transverse motion.

In addition to ballistic heating due to gravity, the atomic beam suffers an inhomogeneous deceleration due to the magnetic compression. The magnetic compression creates a radially dependent gradient in the longitudinal direction. In other words, the atoms with the largest transverse excursions will experience the greatest longitudinal deceleration. This has the effect of heating the atomic beam in the longitudinal

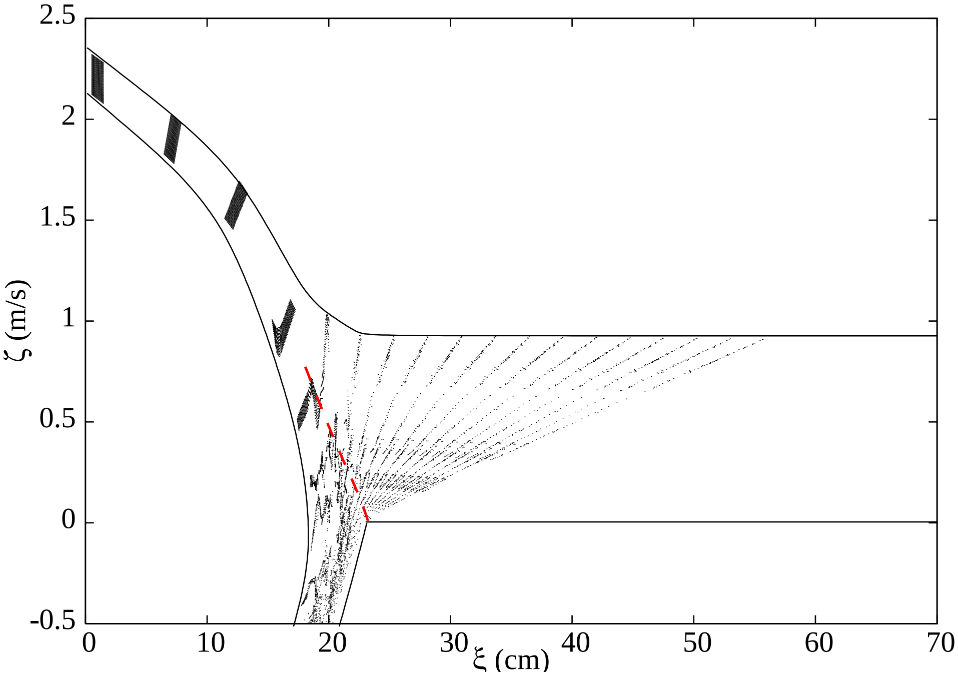

Figure 4.10: Evolution of a phase space element $((\Delta v)_0 = 20 \text{ cm/s}, (\Delta x)_0 = 1\text{cm})$ through the launch section of the atom guide and over the bend. ζ denotes the projection of the velocity into the direction tangential to the guide wires and ξ denotes the propagation length in the guide. In this case, the atoms are launched at the minimum of the field with both the transverse velocities set to 15 cm/s. With the atoms spending a significant amount of time away from the field minimum, the magnetic retardation effects cause a portion of the phase element to become reflected into the MMOT region. As in Fig. 4.9, the discontinuities in the bend region are due to the incomplete decoupling between the longitudinal and transverse motion.

direction. [1] This inhomogeneous deceleration effect is shown in Figs. 4.9 and 4.10. In Fig. 4.9, the initial packet of atoms is also given an initial velocity in one of the transverse degrees of freedom. Though the atoms do all reach the horizontal section of the guide, the associated continuous beam is considerably hotter in the longitudinal direction. In Fig. 4.10, the atoms are given an initial velocity in both transverse directions, such that many of the atoms spend a majority of their time quite far off the axis of the magnetic guide. In this final case, many of the atoms do not reach the horizontal section of the guide and are reflected back into the MMOT region.

---

[1] Assuming a collisionless model, we talk about separate effective temperatures in the various degrees of freedom.

4.3 Atomic-beam Analysis at the End of the Atom Guide

4.3.1 Measurement of the Transverse Temperature

The vertical injection/launch section of the guide is connected with the 1.5 m long horizontal section via a 90° bend with a radius of 1 inch. Considering this geometry as well as the centrifugal force and the transverse gradient of the atom guide in the bend region, it is found that atoms with launch velocities in the range 2 m/s $< v_{\mathrm{MMOT}} <$ 3.8 m/s will be able to transit into the horizontal guide section. Experimentally, a smaller useful range of 2.2 m/s $< v_{\mathrm{MMOT}} <$ 2.8 m/s is found. We believe that on the low-velocity side the useful v_{MMOT}-range is limited by reflection of slow atoms in the magnetic-compression region [40], while on the high-velocity side it is caused by limitations in the MMOT operation. In view of the long-term goals of our work, we are mostly interested in the low-velocity end of the useful v_{MMOT}-range.

In the horizontal guide section, the center-to-center distance between the guide tubes linearly decreases from 5.18 mm after the bend to 4.18 mm at the end. Thus, at a guide current of 300 A the magnetic-field gradient increases from 1.7 kG/cm to 2.7 kG/cm, leading to a further moderate adiabatic compression of the atom flow.

Using the same methods as described in Sec. 4.2.1, atomic-beam images and corresponding temperature fits have been performed at the end of the guide. Fitting the data from a repumper-only measurement, as shown in Fig. 4.11, with functions of the type Eq. 4.9, we find a transverse temperature $T_{\perp} = 420\ \mu\mathrm{K} \pm 40\ \mu\mathrm{K}$. Also, as shown in Fig. 4.12, a temperature fit of $T_{\perp} = 350\ \mu\mathrm{K}$ was determined by the probe-repumper type measurement. Following the discussion in Sec. 4.2.1, the temperature obtained with the probe-repumper method is considered less reliable.

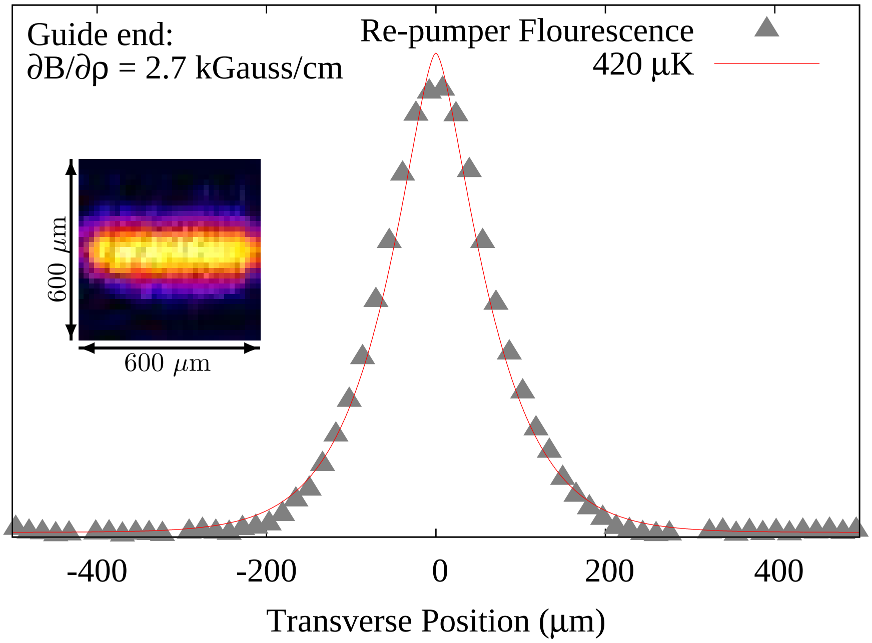

Figure 4.11: Atomic-beam image obtained at the end of the atom guide with repumping light only (inset), and corresponding profile transverse to the guide axis (data points). In the image, the guide axis is horizontal. The line through the data points represents a fit for a temperature of 420 μK.

4.3.2 Measurement of the Longitudinal Temperature

In the horizontal section of the guide, a time-of-flight experiment has been performed. At a location 50 cm ahead of the detection region, a laser beam tuned to the repumping transition ($F = 1 \rightarrow F' = 2$) is introduced. This beam is on most of the time and strongly attenuates the atomic beam. An interruption of this repumper beam for 50 ms defines a short pulse of guided atoms that is allowed to propagate through the length of the guide into the probe region located at the end of the guide. By measuring the temporal spread of the atom pulse, the longitudinal velocity distribution of the atomic beam is derived. A typical result is shown in Fig. 4.13. Fitting the velocity distribution with functions of the type

$$P(v) \propto \exp\left[-\frac{M(v-v_{\|})^2}{2k_{\mathrm{B}}T_{\|}}\right] \quad ,$$

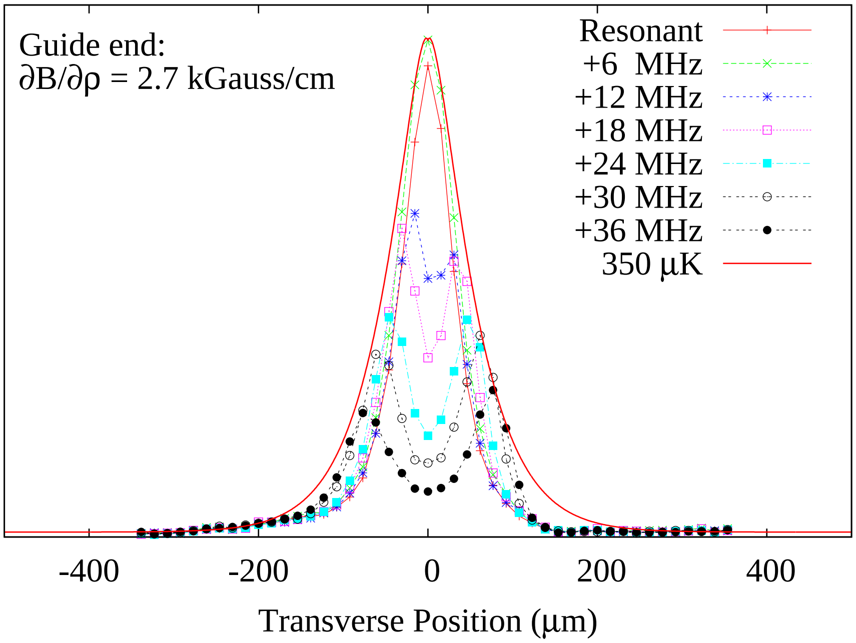

Figure 4.12: Profiles of atomic-beam images transverse to the guide axis with both repumper light and probe light present in the detection region for the indicated detunings of the probe laser relative to the field-free transition frequency. The estimate $T_\perp \approx 350\ \mu$K is obtained by fitting the *envelope* of the profiles with curves of the type from Eq. 4.10.

we find, for the case displayed in Fig. 4.13, a longitudinal temperature of $T_\parallel \approx 1$ mK and an average forward velocity of $v_\parallel \approx 1.2$ m/s. Since in this measurement the tapering of the atom guide and the resultant magnetic retardation force [40] along the time-of-flight stretch was minimal, the values of $T_\parallel$ and $v_\parallel$ are reliable.

4.3.3 Temperature Changes along the Guide

In the following, the changes in transverse temperature that occur along the guide are discussed. The first notable change in temperature occurs between the MMOT and the upper end of the magnetic-compression zone in the vertical launch section of the guide. While maintaining the phase-space density of the atoms, the compression has the side effects of retarding their forward motion and heating them both transversely and longitudinally. In a trajectory simulation in which temperatures of $T_\parallel = 300\ \mu$K and $T_\perp = 250\ \mu$K at the exit of the MMOT are assumed, the transverse

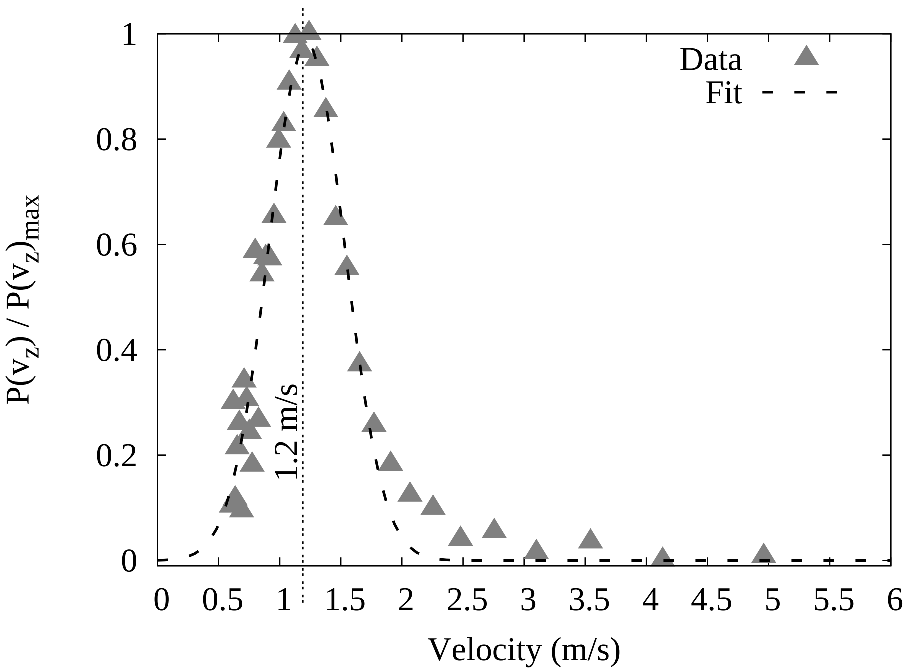

Figure 4.13: Longitudinal velocity distribution obtained from a time-of-flight experiment in the horizontal section of the atom guide. The MMOT launch velocity is $v_{\mathrm{MMOT}} = 2.2$ m/s. The velocity distribution yields a longitudinal temperature of ≈1 mK and an average forward velocity of ≈ 1.2 m/s.

temperature shows an increase to $T_\perp$ to 600 μK ± 40 μK at the observation point used in Sec. 4.2.1 (the error bar arises from statistical noise in the simulation). This simulation result is in reasonable agreement with the experimental result.

The results of Sec. 4.2.1 and Sec. 4.3.1 further indicate a considerable decrease in $T_\perp$ between the respective observation points. This decrease is a secondary consequence of magnetic compression. Since the action of the transverse motion is adiabatically conserved, during the compression longitudinal energy becomes partially converted into transverse energy [40]. Thereby, the amount of energy that is converted increases with increasing transverse energy. Due to this interdependence, the longitudinal velocity distributions and the transverse positions in Figs. 4.4 and 4.11 are not independent. The further off-axis an atom travels, the slower it becomes longitudinally. Since between the observation points of Figs. 4.4 and 4.11 the atoms undergo a final 1.6 cm vertical climb, the further out an atom is in Fig. 4.4, the higher the chance that it does not make the climb and falls back into the MMOT. Thus, there is a trend that between the observation points of Figs. 4.4 and 4.11 the outermost atoms fall back. This effect causes the transverse temperature to decrease. Simulations show that the transverse temperature decreases from $T_\perp \approx 600\ \mu$K to 425 μK ± 35 μK during the final 1.6 cm of vertical climb. This simulation result agrees well with the experimentally observed temperature drop.

4.4 Flux Measurement

Using atomic-beam images obtained with the repumper only, a measurement of the atomic flux in the guide has been performed. The method relies on the fact that the total photon yield per atom for repumper light is quite well known (simulations show about two photons per atom). Important parameters entering into the calculation are the geometric collection efficiency of the camera lens, as well as the pixel yield of the camera per photon reaching the CCD chip.

An analysis along these lines for a launch velocity of 2.5 m/s has yielded an atomic flux of 1.9×10^7 s^{-1} and a central volume density of about 1.2×10^9 cm^{-3} at the end of the guide, with uncertainties less than a factor of two. The s-wave elastic collision rate (cross section $\sigma = 700$ nm^2) at this density and at a temperature of 500 μK is about 0.5 per second, corresponding to about one elastic collision of any given atom during its passage through the atom guide. Therefore, under the present conditions collisions will barely affect the dynamics of the atomic flow and of rf-induced atom removal, discussed in the next section.

The flux measured at the end of the guide amounts to approximately 4% of the MMOT output flux. This result is about a factor of four less than our initial estimate at the end of Sec. II.2.3. We attribute this disparity to the depleting effect of stray repumper light in the vertical section of the guide, which optically pumps atoms from the guided state $|F = 1, m_{\rm F} = -1\rangle$ into other states. We have found very recently that this effect can be alleviated by detuning the repumper laser that is coupled into the MMOT region. Using a de-tuned repumper, a flux increase of about a factor of five at the end of the guide was observed.

4.5 Continuous rf-induced Energy-selective Removal of Atoms

An rf-current is coupled onto one of the guide tubes in the horizontal guide section. Since most of the rf-induced magnetic field is confined to the region between the tubes, this rf-coupling scheme requires little rf power and minimizes rf interference. The rf magnetic field is transverse to the guide axis and has a component transverse to the local static magnetic field practically everywhere on the evaporation surface. rf-induced removal of atoms from atom guides has been performed previously using a different antenna geometry [41, 51].

Fig. 4.14 shows profiles of the atomic beam at the end of the guide for continuously applied rf-currents at a frequency of 9 MHz and the indicated estimated values of the rf magnetic-field amplitude. At 9 MHz rf frequency, a large portion of the atomic beam is above the evaporation threshold $2\pi\hbar\times 9$ MHz (the "rf knife-edge") and should become removed if the rf-coupling scheme is effective. Fig. 4.14 shows that an applied rf field of $B_{\rm rf} = 500$ mG is sufficient for continuous rf-induced removal of practically all atoms above the "rf knife-edge". In the figure, we also compare the measured fluorescence profiles with a fit for a thermal distribution function ($T_\perp = 500\ \mu$K, red curve in Fig. 4.14) and the same distribution truncated at an energy of $2\pi\hbar\times 9$ MHz. There is reasonably good agreement between the calculated curves and the respective measured profiles with no rf and $B_{\rm rf} = 500$ mG.

It is noted that the experimental curves are wider than the calculated ones by $\sim$ 20 μm. The experimental broadening is due to diffraction effects and image smearing associated with the camera pixel size. Integrating the experimental data in Fig. 4.14, it is found that 16% of the atoms are left after energy-selective removal of atoms exceeding a transverse energy of h(9 MHz). Using a calculation, the average potential energy of the atoms remaining after the rf-induced atom removal is found to equal ≈11 % of the average potential energy without rf-induced atom removal.

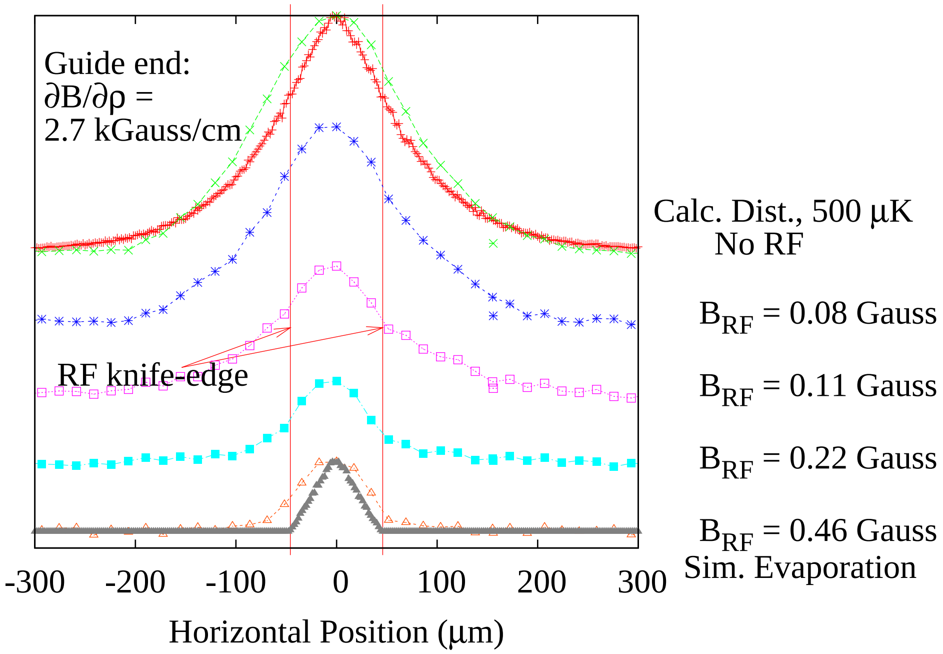

Figure 4.14: Atomic-beam profiles transverse to the guide axis at the end of the atom guide, obtained with repumping light only and with a continuous radio-frequency (rf) current of 9 MHz frequency. The rf current is coupled onto a guide tube in the horizontal guide section. The estimated value of the rf-field magnitude, $B_{\rm rf}$, is indicated to the right of the plot. rf-induced removal of atoms outside the indicated “rf knife-edges” is clearly visible. The rf-induced atom removal saturates at about $B_{\rm rf} = 500$ mG. The experimental data agree reasonably well with calculations for a thermal distribution with $T_\perp = 500$ μK (red curve) and the same thermal distribution truncated at the “rf knife-edge” (gray curve). Both theoretical curves are scaled with the same factor to match the experimental data.

4.6 Summary

A continuous flow of atoms in a 1.7 m long magnetic guide has been realized and the longitudinal and transverse temperatures of the guided atomic beam have been measured. Using an rf waveguide for coupling rf power into the guided atomic beam region, continuous removal of the most energetic atoms has been demonstrated. As of yet, there is no evidence that elastic collisions play a role in the observed atom-beam dynamics.

CHAPTER V

Numerical Methods

As a part of this effort, in collaboration with Andrew Christlieb from the UM Math department, a collisional modeling code has been developed and employed primarily for the purpose of simulating the pre-condensation evaporative process of the atom laser. This code involves a novel gridless implementation of a Direct Simulation Monte Carlo (DSMC) method [52]. As a particle method first developed to find solutions for the Boltzmann equation in rarefied gas flows (where continuous methods fail and computational resources required for direct solution of the Boltzmann equation are prohibitive), DSMC has been used successfully in a wide range of collisional systems. DSMC mandates the notion of nearest-neighbor groupings for the purpose of appropriately simulating the collision process of a system of particles. Typical DSMC involves mapping particles onto a fixed (or slowly evolving) grid, where collisions only occur between particles in the same grid cell. This mapping is intimately bound to the geometry of the physical system and mismatch can result in an erroneous solution. Furthermore, a change in the physical system often requires major changes in the code.

The novelty of the developed code stems from the use of a hierarchical tree algorithm to provide for localization of nearest neighbors. A major advantage of sorting with this approach comes from the fact that the geometry of the physical system is removed from the details of the code. This allows one to easily test arbitrary magnetic field geometries without the need to revamp or change the DSMC code. An additional advantage is faster convergence that occurs because statistical noise in the simulation is spread over the entire system rather than lumping together and moving through different simulated spatial locations. This enables one to determine the quality of a given evaporation plan more quickly. Similar tree algorithms have been very successful in calculations for long-range force problems [53] such as in gravitational [54] or plasma systems [55].

In this chapter, we outline the numerical method developed and implemented to simulate the collision process in the evaporative cooling section of the magnetic atom guide. After a brief introduction to DSMC, we present the step-by-step algorithm, after which we will present a few test cases to establish the validity of the numerical method. The following chapter (Ch. VI) will then discuss the application of this code to the atom laser project, as will show how this has been helpful in determining (or ruling out) possible evaporation schemes.

5.1 Introduction to Direct Simulation Monte Carlo (DSMC) Methods

In general, gas systems are characterized by the ratio of their mean free path λ_{MFP} to the characteristic length $\mathcal{L}$ of the system. λ_{MFP} is given by

$$\lambda_{\mathrm{MFP}} = \frac{1}{\sqrt{2}\sigma_{\mathrm{T}} n} \tag{5.1}$$

where σ_{T} is the total elastic scattering cross section and n is the local number density. The local characteristic length of a system $\mathcal{L}$ is the length over which a macroscopic property of the gas changes, e.g. temperature or density, and can be expressed as

$$\mathcal{L} = T\left(\frac{\partial T}{\partial x}\right)^{-1} . \tag{5.2}$$

The ratio $\lambda_{\mathrm{MFP}}/\mathcal{L}$, called the local Knudsen number and denoted by (Kn), specifies the type of gas system and the modeling approach that is most appropriate. Fig. 5.1 shows the range of (Kn) and indicates the model typically used for each range of (Kn). Low values of (Kn) ($\lesssim 0.1$) represent very dense gas systems for which fluid-modeling equations (i.e. Navier-Stokes) are very appropriate. Conversely, high values of (Kn) ($\gtrsim 0.1$) represent rarefied gas systems for which the fluid model is known to produce unphysical results.

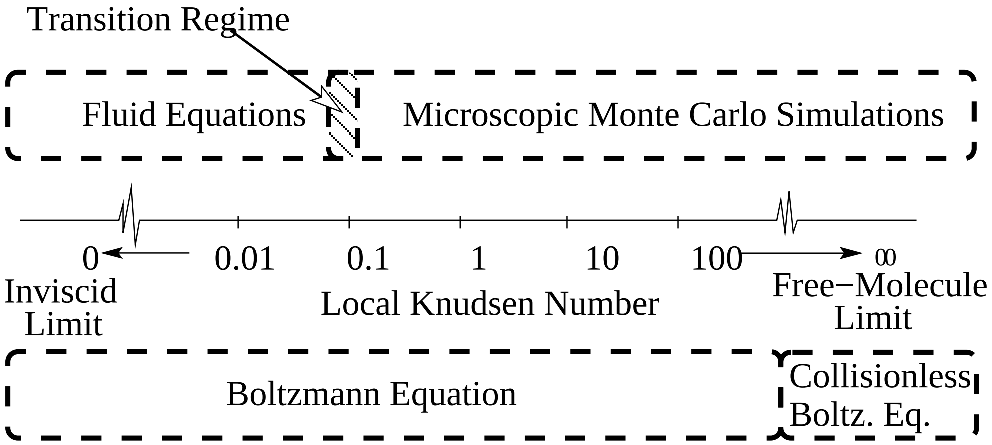

Figure 5.1: Validity regions for various gas simulation approaches. For very low Knudsen number (Kn), fluid equations, such as the Navier-Stokes equations are typically used. As $(Kn) \to 0$, the solutions of the fluid equations approach those of incompressible, inviscid solutions of the Euler equations. For $(Kn) \gtrsim 0.1$, statistical simulations are typically used to model microscopic interactions. As $(Kn) \to \infty$, deterministic free-molecular motion is the limit.

For all (Kn), a gas system can be modeled by the Boltzmann equation, given by

$$m\left[\partial_t + \left(\partial_t \hat{x}_\alpha\right)\partial_x{}^\alpha + \left(\partial_t \hat{p}_\alpha\right)\partial_p{}^\alpha\right] f = \int_{-\infty}^{\infty}\int_0^{4\pi} \left(f^\dagger f'^\dagger - f f'\right)\left|\vec{\mathbf{p}} - \vec{\mathbf{p}}'\right| \sigma d\Omega d\vec{\mathbf{p}}' \tag{5.3}$$

where $f\left(\vec{\mathbf{x}}, \vec{\mathbf{p}}, t\right)$ describes a phase-space distribution for the gas over all space and momentum $\vec{\mathbf{p}}$, $\hat{x}_\alpha$ and $\hat{p}_\alpha$ are the position and momentum operators respectively, and m is the mass of a gas particle. The double integral on the right side of Eq. 5.3

models collisions between particles in phase-space. It is thereby conceivable that a solution for a gas system might be found by directly solving Eq. 5.3.

In some cases, though only with low degrees of freedom, it is possible to analytically solve the Boltzmann equation. For higher degrees of dimensionality, only numerical solutions are possible. One such numerical method of solving the Boltzmann equation is via a direct finite-element approach. While this method simply implements a solver for a differential/integral equation, it is extremely resource intensive. For even semi-complex geometries, it is necessary to have resources beyond the reach of many small institutions, e.g. terabytes of random access memory and years of computational time (at least with current CPU speeds).

For more complex physical systems, the continuum approach to solving Eq. 5.3 becomes prohibitive. For this reason, Bird [56] proposed using a statistical approach to solving the Boltzmann equation for rarefied ($(Kn) \gtrsim 0.1$) gas flows. This approach involves direct simulation of the microscale processes, i.e. microscale motion and collisions. In other words, the motion of individual particles is followed and interparticle collisions are directly calculated. While the microscale motion of particles in a simulation can be deterministic, collisions are simulated in a statistical manner according to proper probability laws. This method has become known as Direct Simulation Monte Carlo (DSMC). The remainder of this chapter will outline the algorithm and our approach to its implementation.

5.2 Numerical Approach

In a direct simulation of microscopic gas dynamics, molecular motion and collisional processes must be calculated. This involves following the position of each particle in the system and exchanging energy and momentum between particles in the form of an elastic collision. The basic tenet of DSMC allows separation of the collisional time-scales from the time-scale of the free molecular motion. By assuming such a separation, a simple algorithm is achievable, wherein each of the physical processes is handled independently in a step-by-step fashion. Because DSMC allows the decoupling of the simulation of the physical processes, these steps may be executed in an almost arbitrary order. Thus, a simple implementation of DSMC could include a few steps as shown in Fig. 5.2. First, collisions are performed between nearest neighbors according to a physical collision probability. Second, the particles are allowed free-molecular movement according to the Hamiltonian of the system. Last, boundary conditions are applied to particles as necessary.

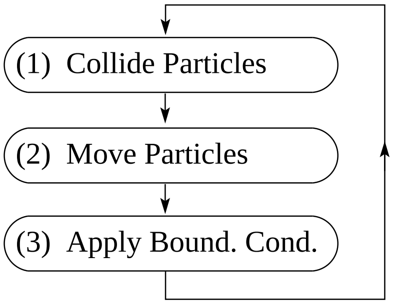

Figure 5.2: Simple implementation of DSMC.

It must be noted that this de-coupling of the free molecular motion from collisional processes is only valid for simulations where the probability of any particle colliding with another in any given time step is much smaller than unity. This is ensured by the common requirement that the basic time step of the simulation is no more than 10 % of the collision time.

5.2.1 Nearest Neighbor Collisions

Particle species for which long range interactions can be neglected only have a significant probability for collisions with nearest neighbors. Thus, for implementing a collision model with such particles, it is valid (and an efficient use computational resources) to limit collision tests to pairs of particles that are separated less than or on the order of a few collision lengths. In other words, it is unnecessary to calculate collision probabilities for pairs of particles which are separated by a distance much greater than the mean free path λ_{MFP}.

A typical approach for implementing efficient collision pair selection involves inserting a preparatory step before step 1 in Fig. 5.2. During this preparatory step, all particles are sorted into bins that contain only nearest neighbors within a particular portion of the simulated space. Collision pairs are then created by selecting partners from within the same spatial bin. This allows an efficient selection of probable collision pairs without the need to overextend the computational resources.

Traditionally, a fixed grid of computer memory maps to a grid of simulation cells and that provide natural binning for collecting and organizing the groups of nearest-neighbor particles. While this fixed-grid approach enjoys much success, development of fixed grids often requires much finesse for creating the correct layout of grid cells. For example, a system with steep gradients (of gas properties such as density or velocity) such as at the front of a shock propagation, a uniform grid is problematic: if the grid cells are too large, such that the shock front is traversed by a walk of one or two cells, incorrect collision statistics will result. On the other hand, in low density regions, if the cells are too small, large statistical error will occur. In addition, a dense grid in a rarefied gas region will result in wasted computational resources. Ideally, creating a physically correct simulation with a fixed grid involves an algorithm with the following steps.

1. A fixed grid is created to best match the estimated solution.
2. The simulation is executed until steady state is reached or until noticeable error in the solution increases.

3. The simulation results are compared with the geometry of the grid.
4. If the grid-simulation comparison does not meet a given tolerance, the algorithm returns to step 1 to repeat the process.

By iterating this algorithm, a correct grid would be found that produces the correct solutions to the physical system. This is the idea behind adaptive mesh refinement (AMR) [57, 58].

5.2.2 Gridless DSMC

Rather than attempting to create physically correct simulations via the grid-refinement procedure, we have implemented a gridless technique that avoids the issue of grid-mismatch. Without the need to match a grid to an underlying physical system, the gridless approach further allows the abstraction of the DSMC code from the description of the physical environment. In other words, the user (i.e. physics programmer) is allowed to focus on the details of the physical system (boundary conditions, forces, etc.) rather than the DSMC layer of the simulation.

The main disadvantage of a gridless system stems from the computational time required to sort particles into nearest-neighbor bins. It is of utmost necessity to avoid algorithms where the required computational time increases exponentially with particle number. Various non-gridded sorting algorithms have been around for some time, but only since the development and work with the generalized binary search algorithm (expanded to n dimensions) has a tractable solution been possible. The two and three dimensional specializations of this algorithm are known as the quadtree or octree algorithms respectively. By implementing the generalized binary search algorithm, we have developed a code that automatically adjusts to the changes of the particle distribution in a simulation requiring $O\left(Nlog\left(N\right)\right)$ time. Because our particle simulations are at most three-dimensional, we will hence refer to the generalized binary search tree algorithm as the octree algorithm.

5.2.2.1 Octree Sort

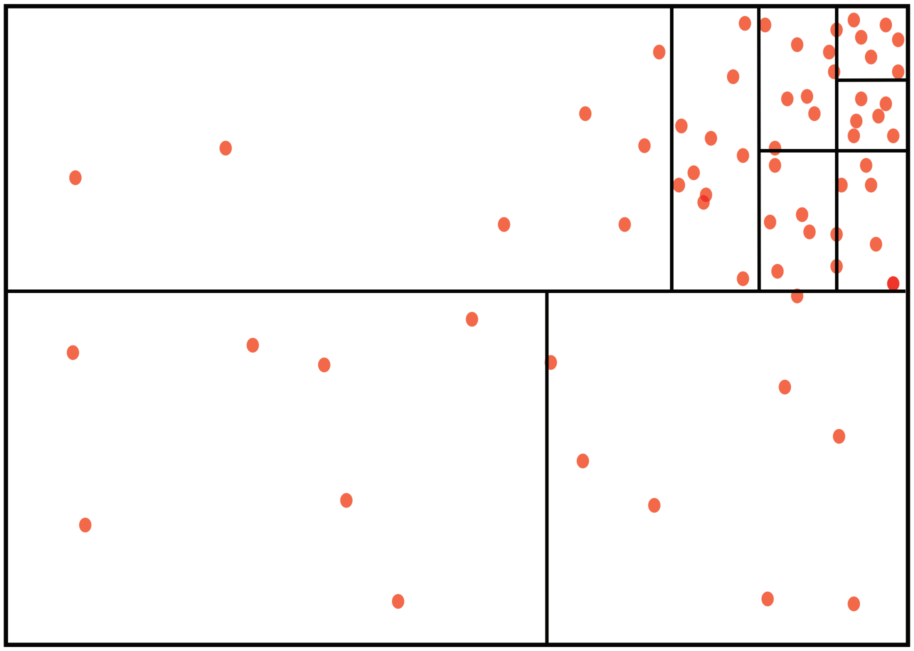

Figure 5.3: Quadtree: two-dimensional specialization of the octree. For an arbitrary distribution of particles, as indicated by the dots here, the root node of the tree is just large enough to bound all the particles in the system. Terminal subdivision is then performed by iterating a quicksort of each degree of freedom using the center of mass as the pivot point.

Because the two-dimensional specialization of the octree, or quadtree, lends itself to a simple description, we discuss it first. Consider an arbitrary two-dimensional distribution of objects or particles as indicated in by the dots in Fig. 5.3. The root container or box is made just large enough to bound all particles within the system. For the purpose of grouping nearest neighbors in a simulation, it is desirable to sub-divide the root box into smaller containers, wherein a specified maximum number of particles per box is present. Subdivision into terminal leaf nodes begins by performing a quicksort of the particles over each degree of freedom. [1] This sorting

---

[1] There are many good entry-level descriptions of quicksort on the WEB, many of which have JAVA applet demonstrations. A few sites on the WEB that I found helpful are
`http://www.cs.sunysb.edu/~algorith/lectures-good/node5.html`,

mechanism is iterated over the various degrees of freedom, generating a new level in the hierarchical tree at each iteration. For n dimensions, this results in the creation of $\leq 2^n$ new child nodes or branches. Thus for two dimensions, the hierarchical tree is known as a quadtree, whereas for three dimensions, it is known as an octree. When a newly created node has less than a given maximum number of particles, N_{max}, the iteration down that branch of the tree stops. (N_{max} is typically set in the range $40 \lesssim N_{\mathrm{max}} \lesssim 100$.) The terminal leaf nodes of such an iterative scheme for a quadtree is depicted in Fig. 5.3 by the various boxes in the figure. Each box contains roughly the same number of particles. An analogous example of an octree is given in Fig.5.4.

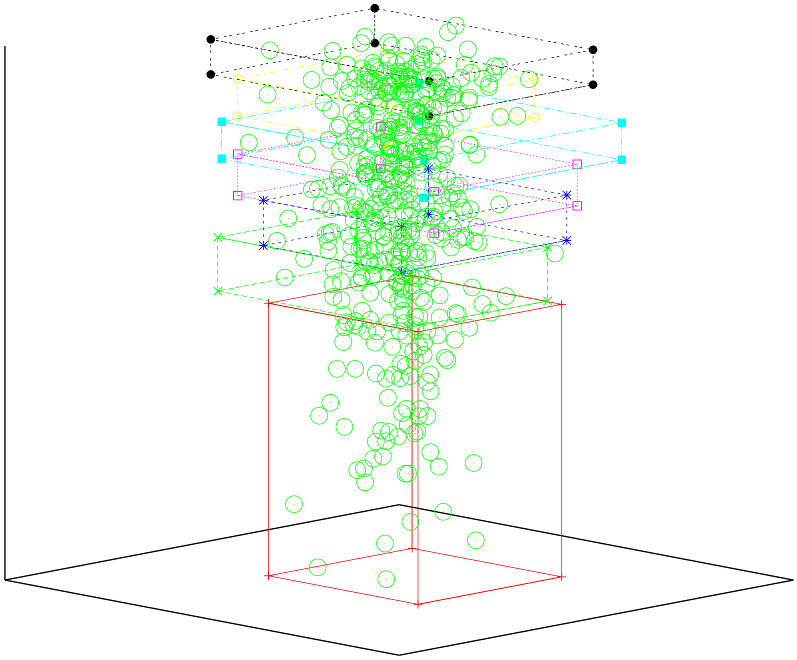

Figure 5.4: Octree of a three-dimensional distribution of atoms. This particular figure represents a snapshot of an atomic beam in its startup phase. The boxes indicated in this figure are the bounding boxes of the leaf nodes of the octree. These bounding boxes were created using the "CM/Shrink" method described in Sec. 5.3.2.

`http://www.nist.gov/dads/HTML/quicksort.html`, and
`http://en.wikipedia.org/wiki/Quicksort`

5.2.2.2 Octree For DSMC

Typical octree implementations divide a container into eight equally-sized domains. This is a valid and fast method for sorting objects into a tree such that the tree is easily searchable. This is the approach taken by many modern computer graphics systems for the purpose of deciding which objects to render [59]. Such a hierarchical organization is also commonly used for simulated collision detection [60], especially in modern computer gaming systems. [2]

Although this method of dividing space by its geometrical center may be the fastest approach, DSMC can benefit by using an alternate scheme. In order to obtain leaf nodes with a more uniform particle number and thus more uniform collision rate per node (done to reduce statistical noise), our octree algorithm divides a node about the center of mass. By dividing by the center of mass, sibling nodes have roughly the same particle number. This ensures a more uniform tree depth and avoids badly imbalanced trees. A more uniform tree depth keeps the computational load throughout the simulation space roughly constant. Furthermore, by ensuring that leaf nodes have roughly the same particle number, statistical noise that is common in DSMC due to large oscillations in the cell occupancy rate should be minimized, though not eliminated (a refinement study is needed to prove this).

5.2.3 Revised DSMC Algorithm

As described in Sec. 5.2, the DSMC algorithm allows a nearly arbitrary order of the sort, collide, move, and boundary-condition steps. This allows us to optimize the order such that computational time is minimized and implementation is less complicated. An outline of our implementation of Gridless DSMC is shown in

---

[2] There are numerous popular articles (mostly for a programmer audience) concerning using octrees to optimize graphics rendering as well as collision detection. These are easily searchable on the web using Google.

Fig. 5.5. Each time step begins the current population of particles sorted into an octree with a certain maximum number of particles per leaf node. After the sort is finished, macroscopic gas quantities (needed to obtain correct collision statistics) are assigned to each of the leaves of the newly created octree. (The following section will detail our method of performing this assignment in a gridless environment.) This is followed by the collision selection and execution methods detailed in Sec. 5.2.3.2. Free particle movement then takes place, followed by the application of boundary conditions.

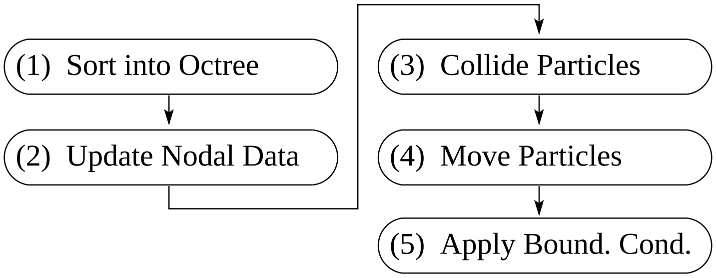

Figure 5.5: Flow chart of our implementation of a Gridless DSMC algorithm.

5.2.3.1 Gridless Maintenance of Macroscopic Quantities

In DSMC, local macroscopic gas properties are needed to maintain correct collision rates. Many of these macroscopic quantities tracked per grid cell are further time-averaged to reduce statistical noise. In a gridless approach, there is no underlying structure to track and maintain such time-averaged macroscopic quantities. We have therefore developed an adaptive method that tracks these quantities at the lowest levels of the particle octree. Near the beginning of each time step (just after sorting), instantaneous quantities such as density and average velocity are measured. To account for time averaging, a weighted average is taken between the instantaneous data and an interpolation of the data of the previous time step, as indicated in Fig. 5.6. After performing this update, the old tree is then discarded.

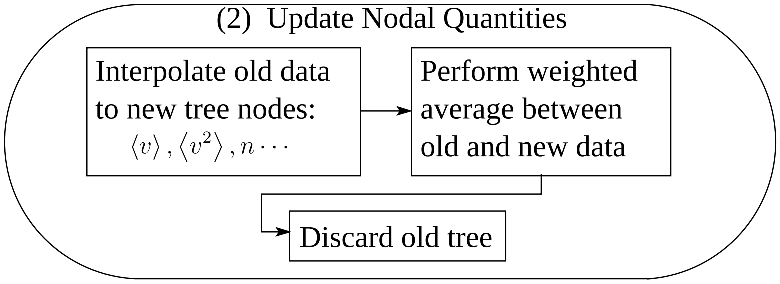

Figure 5.6: Steps to update local gas properties using a gridless technique.

To perform the interpolation, any unstructured interpolation scheme will work, such as Shepherd's algorithm [61]. Unfortunately, performing unstructured interpolation is known to be very computationally intensive (i.e. this should raise a red flag with DSMC enthusiasts). We solve this dilemma by accepting a method with an interpolant that does not pass exactly through the data. Hernquist and Katz [62] developed such a method for use with octrees in a smoothed particle hydrodynamics (SPH) calculation.

This method is based on a spherical spline with a kernel given by

$$w\left(r, r_{\mathrm{I}}\right) = \frac{1}{\pi {r_{\mathrm{I}}}^{3}} \begin{cases} 1 - \frac{3}{2}\left(\frac{r}{r_{\mathrm{I}}}\right)^{2} + \frac{3}{4}\left(\frac{r}{r_{\mathrm{I}}}\right)^{3}, & 0 \leq \left(\frac{r}{r_{\mathrm{I}}}\right) \leq 1 \\ \frac{1}{4}\left(2 - \left(\frac{r}{r_{\mathrm{I}}}\right)\right)^{3}, & 1 \leq \left(\frac{r}{r_{\mathrm{I}}}\right) \leq 2 \\ 0, & 2 \leq \left(\frac{r}{r_{\mathrm{I}}}\right) \end{cases} \tag{5.4}$$

where r is the distance from the data to the point of evaluation and r_{I} is what is known as the radius of influence for the respective data point. r_{I} is given by

$$r_{\mathrm{I}} = \left(\frac{3V_{\min}}{4\pi}\right)^{1/3}$$

where $V_{\min}$ is the smallest volume that includes a specified number of nodes (this specification of neighboring nodes to include is constant over the entire tree). It should be noted that r_{I} is determined under the assumption of local isotropy in the nodal distribution. A demonstration of this technique is shown in Fig. 5.7, where the interpolation of coarsely sampled $\sin(x)/x$ is performed.

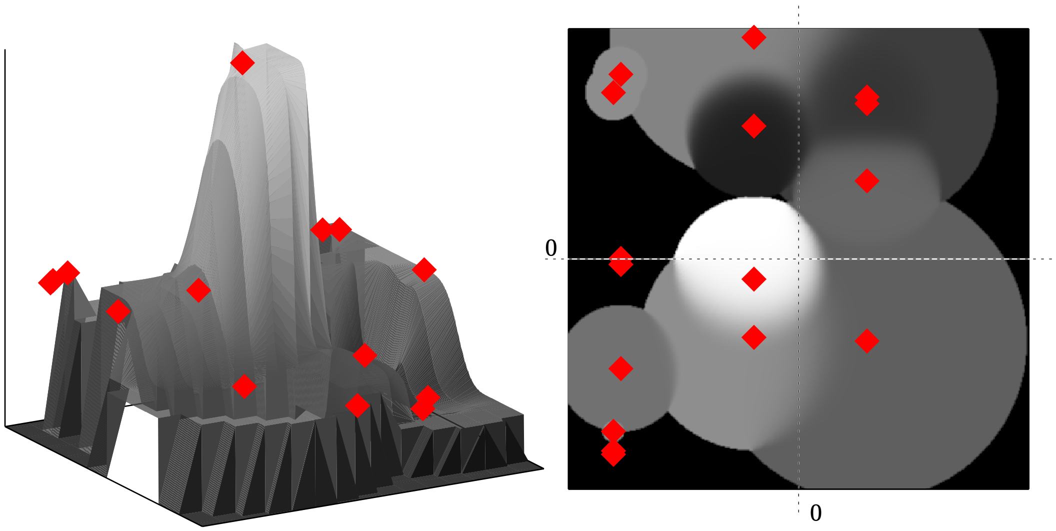

Figure 5.7: Spherical spline interpolation of a coarsely sampled $\sin(x)/x$ function. The diamonds indicate data points. Left: Comparing the interpolated spline to the original set of data shows a reasonable interpolation. For visibility, a coarse sampling of the interpolant was used. Right: A two-dimensional view of this interpolated spline highlights the radii of influence assigned to each of the data points. The radius of influence is dynamically assigned such that a given number of nodes fit inside the spherical volume with that radius. For demonstration purposes, the number of nodes within the volume of influence in this figure was limited to one. Thus, some data points with very small separation have a nearly invisible radius of influence.

In terms of using this method in DSMC for tracking local gas properties, the effect is to both average in time as well as in space. Though a more thorough study of this is needed, we believe this may further reduce the typical DSMC noise. A more thorough study could include the comparison with simulations where something like Shepherd's algorithm is used.

5.2.3.2 Collide Particles

Within a tree-node, standard DSMC techniques are used for selecting collision pairs with an alteration only in the number of collision pairs to test. G. A. Bird's standard "no-time-counter" [3] method [52] prescribes the number of collision pairs to

---

[3] As a historical note, early implementations of DSMC achieved correct collision rates by directly comparing the elapsed time of the simulation to the real-time accumulation of time spent for collisions. This approach is called the "time-counter" method and is described by Bird [63]. Although successful, the "time-counter" method does not lend

test N_{sel} as

$$N_{\mathrm{sel}} = \frac{1}{2} \frac{F_{\mathrm{N}} N \left\langle N \right\rangle \Delta\ t \left(\sigma_{\mathrm{T}} v_{\mathrm{rel}}\right)_{\mathrm{max}}}{V} \tag{5.5}$$

where F_{N} is the number of physical particles each simulated particle represents, N is the number of particles in the cell, $\langle N \rangle$ is this number averaged over time, Δt is the time step of the simulation, and $\left(\sigma_{\mathrm{T}} v_{\mathrm{rel}}\right)_{\mathrm{max}}$ is the maximum value in the particular cell of the product of the total scattering cross section σ_{T} and relative particle velocity v_{rel}. The normalized probability of any given collision pair actually exchanging momenta is then given by [4]

$$P_{\mathrm{coll}} = \frac{\left(\sigma_{\mathrm{T}} v_{\mathrm{rel}}\right)}{\left(\sigma_{\mathrm{T}} v_{\mathrm{rel}}\right)_{\mathrm{max}}}. \tag{5.6}$$

In our gridless algorithm, we replace some of the factors in Eqs. 5.5 and 5.6 with their space-time smoothed equivalents, denoted as $< \cdots >_{x,t}$, from the gridless tracking scheme described in Sec. 5.2.3.1. Doing so, Eqs. 5.5 and 5.6 become

$$N_{\mathrm{sel}} = \frac{1}{2} F_{\mathrm{N}} N \left\langle n \right\rangle_{x,t} \Delta\ t \left\langle \left(\sigma_{\mathrm{T}} v_{\mathrm{rel}}\right)_{\mathrm{max}} \right\rangle_{x,t}, \tag{5.7}$$

and

$$P_{\mathrm{coll}} = \frac{\left(\sigma_{\mathrm{T}} v_{\mathrm{rel}}\right)}{\left\langle \left(\sigma_{\mathrm{T}} v_{\mathrm{rel}}\right)_{\mathrm{max}} \right\rangle_{x,t}} \tag{5.8}$$

where $\left\langle n \right\rangle_{x,t}$ and $\left\langle \left(\sigma_{\mathrm{T}} v_{\mathrm{rel}}\right)_{\mathrm{max}} \right\rangle_{x,t}$ are the exponential (running) space-time averages of the n and $\left(\sigma_{\mathrm{T}} v_{\mathrm{rel}}\right)_{\mathrm{max}}$ respectively.

5.2.3.3 Move particles

The particular integrator that one uses to move the particles under free molecular motion depends on the application. For instance, in a non-harmonic atomic trap it

---

itself easily to be used for scalable systems, as each parallel component must be tied very intimitely to the whole system. Bird [52, and references therein] later developed a scalable method of a priori selecting the number of collision pairs to test in any given region of the simulation. The work presented here uses this so called “no-time-counter” method to achieve correct collision rates.

[4] See [52] for a good description of the physical intuition of Bird’s method.

is often best to use a high accuracy method, such as 5th-4th order adaptive Runge-Kutta. For the case when there are no trapping potentials, a simple leap-frog or 2$^{\text{nd}}$ order Runge-Kutta routine is sufficient.

5.2.3.4 Apply boundary conditions

After moving the particles and before continuing with the next time step iteration, it is necessary to apply boundary conditions. To do this, we introduce the concept of boundary objects. A boundary object can be something as simple as a reflective surface that has a bounded volume (for generality, the bounding volume of a boundary object is allowed to be as large or small as possible). While moving the particles, we maintain and update the maximum distance any one particle in a particular octree leaf has traveled. Using this maximum distance traveled, we then scale the bounded volume of the boundary objects and test for resulting overlap with the bounded volume of the octree leaf, as depicted in Fig. 5.8. The associated boundary condition for the overlapping boundary objects is then tested and applied to all relevant particles within the leaf. The applicability of this method will be briefly discussed in Sec. 5.3 with an example application.

For each new geometrical type of boundary condition, a new boundary object must be coded. To streamline the application of complex physical boundaries, perhaps an approach more similar in nature to gaming code would be helpful. Gaming code takes care to reduce large complex surfaces into simple constituents.

5.3 Results

To verify the validity of this numerical approach, we performed some standard DSMC simulation tests including normal Couette flow and thermal Couette flow. In the following sub-sections, we will present the results of these tests. We will conclude

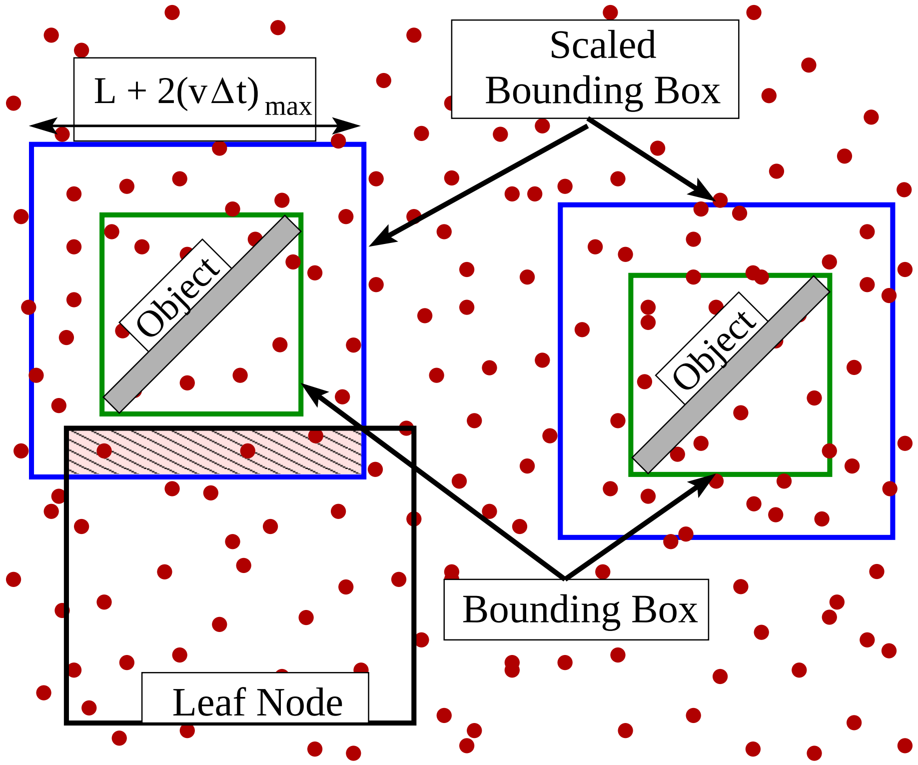

Figure 5.8: Schematic of boundary object collision test for applying boundary conditions. The side lengths of bounding boxes of all boundaries are first increased by the maximum distance traveled $(v_i \Delta t)_{\max}$ by any one particle in the given octree node. Boundary conditions are only applied from scaled boundaries that overlap with the octree node. The shaded region indicates the overlap between one boundary and the octree node.

this section with a measurement of the speed of the algorithm.

5.3.1 Couette Flow

A classic test to help validate a DSMC code is that of a Couette flow. A Couette system is described by two parallel, diffusely (i.e. non-specularly) reflecting plates, each at some specified temperature and transverse velocity, as depicted in Fig. 5.9. The dynamics of one-, two-, or three-dimensional gas between the plates are allowed to approach steady state.

For the two following Couette-flow tests, the simulations were run as a function the order of magnitude of the Knudsen: from high density case, through the transitional regime, to rarefied gas flow.

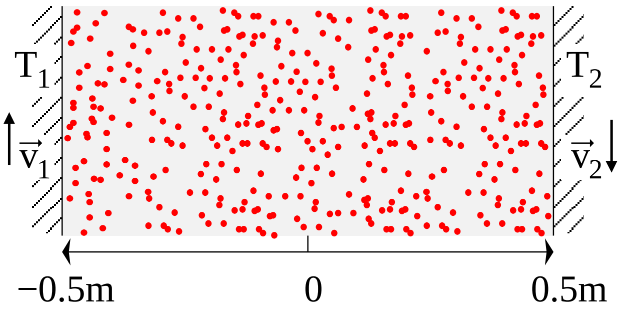

Figure 5.9: Setup for Couette flow simulations. The channel between the two plates is initially filled with a uniform distribution of simulated Ar gas at 273 K.

5.3.1.1 Thermal diffusion

In the first Couette-flow test, a uniformly distributed one-dimensional sample of Ar gas, initially at rest and at 273 K, is placed between two stationary plates held at 173 K and 373 K respectively. The system is then allowed to evolve until steady state is reached. For each of these simulations, the number of simulation particles was kept constant at $N = 10000$. Many averages were done to reduce the statistical noise in the presented results. For the fixed grid data, 1×10^5 averages were used [64], whereas for the gridless data, 2×10^4 to 7×10^4 averages were used, depending on the value of (Kn).

Temperature profiles of the steady-state solution for various orders of (Kn) are shown in Fig. 5.10. We find very good agreement with similar results from a fixed grid simulation (also shown in Fig. 5.10) for $(Kn) <= 10$ (the low-to-high density cases). For the very rarefied case with $(Kn) = 100$, we find that the gridless technique appears to produce results closer to the free molecular flow regime than does the fixed grid system. As discussed below, we believe this may be an indication that the gridless method actually performs better than the fixed grid system for very rarefied gases.

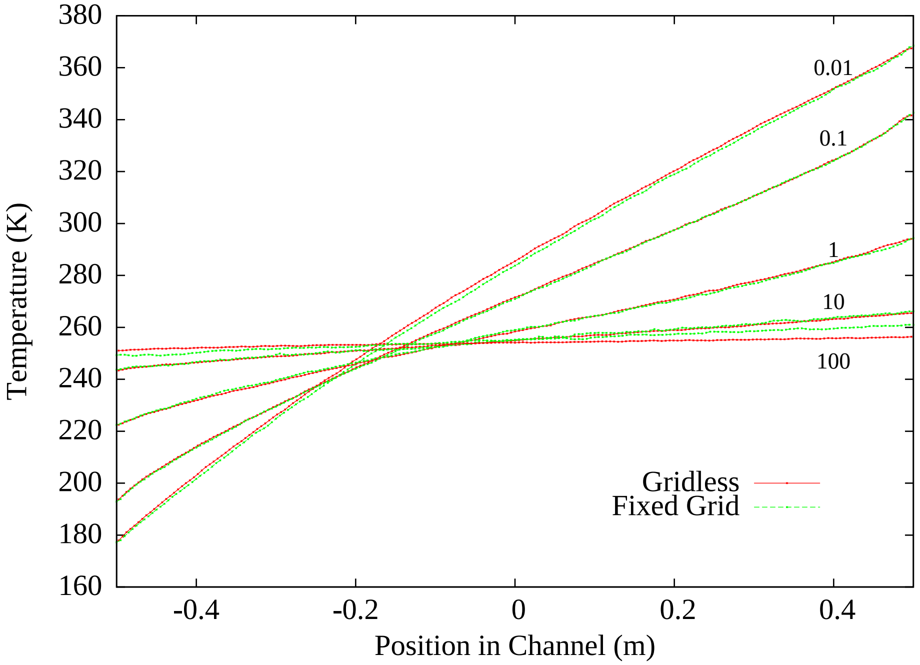

Figure 5.10: Temperature profile across a channel in a thermal Couette flow simulation. The left and right walls are held at 173 K and 373 K respectively. The particles are initially uniformly distributed between the two plates with zero average velocity. The results for Knudsen numbers of 0.01, 0.1, 1, 10, and 100 are compared to similar results from a fixed grid approach. (Fixed grid data as published in [64] used with permission.) Fixed grid data courtesy of Dr. Quanhua Sun [64].

5.3.1.2 Velocity diffusion

In the second Couette-flow test, the sample gas is placed between two plates, both of which are held at 273 K, but have transverse velocities of ±150 m/s. Initial conditions as well as averaging procedures for this simulation were coincided with those of the first Couette-flow test.

Temperature profiles of this simulation are compared to similar fixed-grid results in Fig. 5.11 and velocity profiles are likewise compared in Fig. 5.12. From each of these two figures, we can see a very good agreement with the fixed grid data for the higher density cases. Similar to the thermal Couette flow, there is a slight disagreement in the low to very rarefied cases ($(Kn) = 10$ and $(Kn) = 100$). Looking at a closeup of the temperature profiles in these low density cases, shown in Fig. 5.13,

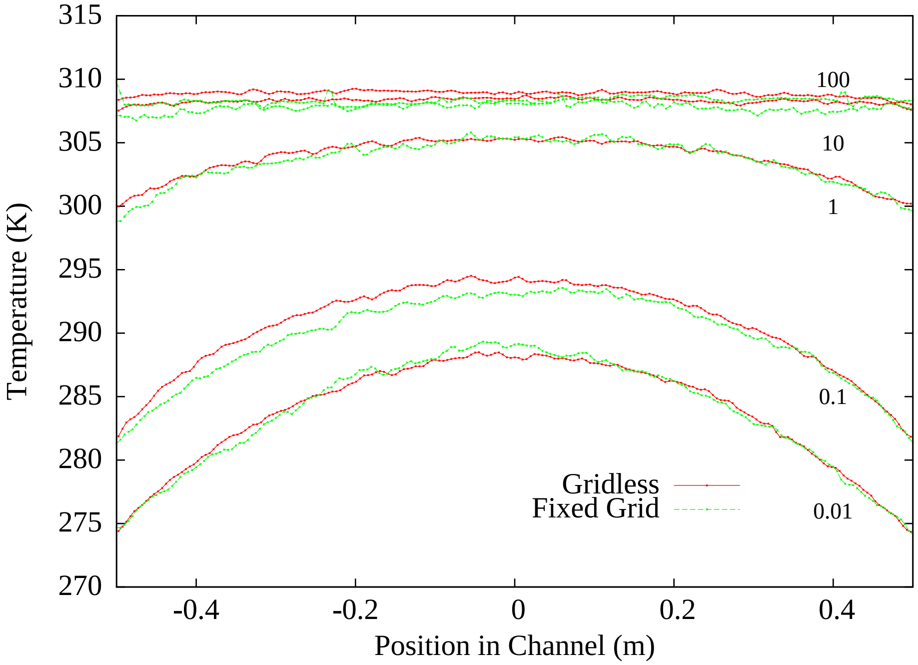

Figure 5.11: Temperature profile of a Couette flow simulation. The particles are initially uniformly distributed between the two plates, the transverse (to the channel) velocity of each is $\pm 150\frac{\mathrm{m}}{\mathrm{s}}$ respectively. Fixed grid data courtesy of Dr. Quanhua Sun [64].

there appears to be slightly more curvature in the gridless results than in the fixed-grid results. This appears to be the case even for a much lower number of averages in the gridless case ($\sim 5 \times 10^4$ for $(Kn) = 10$).

The differences between the sets of results of these two Couette-flow tests cannot be easily attributed to systematic error in the gridless approach. This is because for one case, the simulation appears to be slightly more collisional (the case of velocity diffusion where curvature in the temperature profiles is seen), while for the second case the gridless simulation appears to be slightly less collisional (the case of thermal diffusion where the results more closely resemble a free molecular flow). In spite of these initial findings, a refinement study is needed to determine the relative performance of the fixed-grid to a gridless system for the very rarefied case. More alignment in the timing of sampling for averages between the two methods will need to take place.

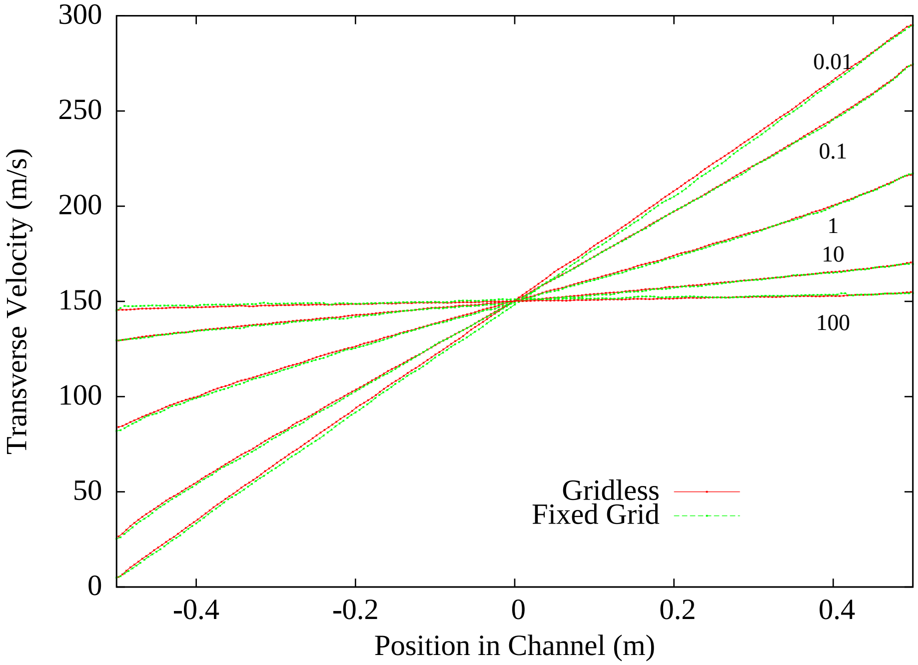

Figure 5.12: Velocity profile of a Couette flow simulation. The particles are initially uniformly distributed between the two plates, the transverse (to the channel) velocity of each is $\pm 150\frac{\mathrm{m}}{\mathrm{s}}$ respectively. Fixed grid data courtesy of Dr. Quanhua Sun [64].

5.3.2 Computational Time Issues

For large DSMC simulations, the computational time required for an iteration of the algorithm is of utmost importance. Because the physical system is simulated by paying attention to the microscale interactions, memory as well as CPU resources are taxed very heavily. Time step iterations on the order of 1 μs per simulation particle are considered to run at average speed, while fast codes, all of which are optimized gridbased systems have been known to need as little as ~ 0.5 μs per particle. [65] The most time intensive portion of our gridless DSMC implementation occurs within the octree sorting algorithm. Though, among unstructured sorting algorithms the octree performs very well ($O(N\log(N))$), it cannot really compare to the integer arithmatic of a fixed-grid binning algorithm (some of which are able to give ~ 0.5 μs per particle). It is therefore necessary to discuss the execution time required to run

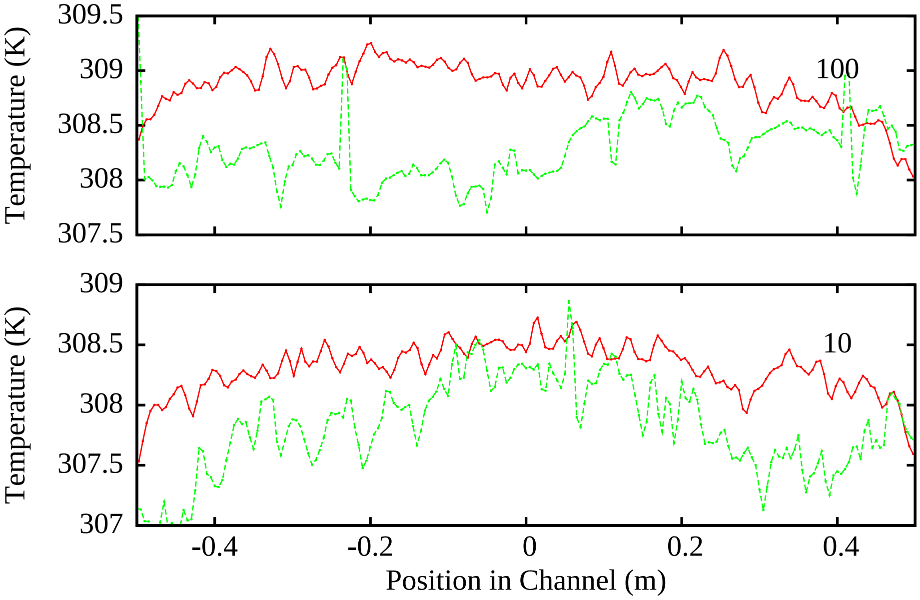

Figure 5.13: Temperature profile of a Couette flow simulation for significantly high values of (Kn). Fixed grid data courtesy of Dr. Quanhua Sun [64].

a DSMC code based on the gridless system and determine the viability of running large simulations with this code. [5]

While testing the sort of particles into nearest neighbor octree nodes, we used three different cases, each of which cost slightly more with regards to processor time (see Fig. 5.14). The first method we name the Center method. This is the most standard division routine for the octree, where a node divides into children based on the geometrical center of the node. Because of this type of division, each of the child nodes are of the same shape and size.

The second method we name the CM method, or center-of-mass method. In this case, an octree node is divided into children with each of the axes of the division passing through the center of mass. By dividing through the center of mass, the leafnodes of the octree will have roughly the same number of particles (for a mono-

---

[5] It should be noted that these algorithm speeds are for field-free gas flow. For the case of the high-gradient atom guide, executions time are at least an order of magnitude slower because of the necessity to calculate (or interpolate) accelerations due to the magnetic trapping field.

tonic gas). This will ensure a roughly balanced octree allowing additional operations on the tree to be optimized for speed. Even for a gas with additional components, the leafnodes will have a more closely matched number of collisions per time-step. This should prove helpful for reigning in the statistical error of typcial DSMC. As shown in Fig. 5.14, the CM method is slower than the Center method. This is because the center of mass of each node must be measured before subdividing the node.

The third method we name the CM-Shrink method. Similar to the CM method, subdivisions are performed about the center of mass of the parent node. The difference is that the volume of each of the newly created children are shrunken to only bound the particles within this box. Though using the CM-Shrink method for DSMC would result in synthetically high collision rates (because the density would be over guessed), this type of subdivision will be useful for integration with plasma codes. [66] This is the slowest of the three methods as shown in Fig. 5.14. In addition measuring the center of mass, the bounding volume must also be measured.

Fig. 5.14 shows the time-to-sort per particle for the various subdivision schemes. It can be seen from Fig. 5.14 that though the performance of the three methods varies, the difference between them is not too great. In addition, the execution time of this sort is on the order of 1 μs, or less than an order of magnitude slower than optimized fixed-grid DSMC. We conclude therefore, that this gridless method is a viable DSMC method with respect to sort time. Furthermore, the abstraction of the DSMC algorithm from the physical system establishes an ease of use (i.e. simple reusability of code) that justifies the moderate sacrifice in computational time.

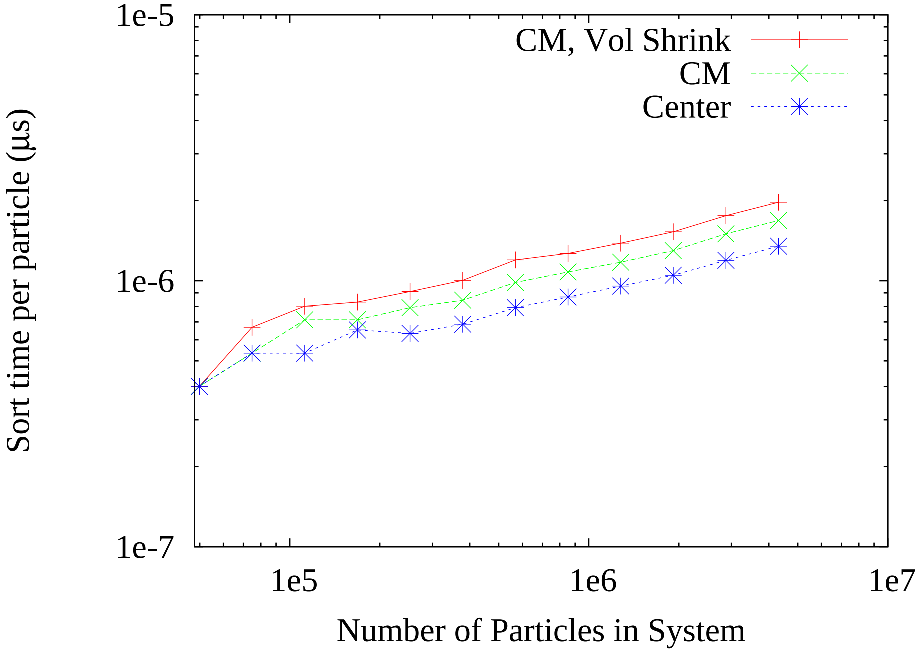

Figure 5.14: Time required to sort as a function of number of particles in the system. From this graph, it is apparent that these three volume defining methods only differ by a component linear in N (is this true–think for a second...). For DSMC calculations, where local density should not be over-guessed so as to obtain correct collision rates, the most appropriate volume defining techniques are either the CM no shrink, or geometrical division methods. The vol-shrink routine would be useful for plasma simulations. [66]

CHAPTER VI

Simulations

The implementation of a continuous-wave atom laser design and exploration of its parameter space are non-trivial. While the components in the present apparatus have been designed to be modular, large changes on a day-to-day basis remain difficult. Thus, the various components present in the system define the range of parameter space that can be explored for a length of time on the order of weeks to months. To aid in the determination of plausibly good system parameters, we have developed a suite of tools to simulate both laser and evaporative cooling. The primary goal of this numerical work is to increase the rate at which the experimental portion of the atom laser project is successful. By testing schemes well before experimental implementation, we hope to shorten the time-table for attaining a continuous-wave atom laser.

In this chapter, we discuss several of these simulations and more importantly their impact on the future of the continuous-wave atom laser. We will first discuss some of the simulations regarding the MMOT-guide coupling and finish with collision simulations for the evaporative cooling process.

6.1 Compressed Moving MOT

As a part of our simulation work, we have considered alternative forms of the MMOT, with the goal of increasing the initial phase-space density of the atomic beam in the magnetic guide. By increasing the initial phase-space density in the guide, the evaporative cooling process becomes more viable and requirements relaxed. In addition to fundamental MMOT issues, we have examined MMOT-guide coupling. Early on in this experiment, we determined that a large mode-mismatch existed between the MMOT and the magnetic guide. While the MMOT at the extraction point has a radius of $\lesssim 100$ μm, the magnetic guide mode for similar temperatures is much higher (~ 500 μm). This mode-mismatch is problematic because of the resulting transverse oscillations that occur in the guided atomic beam. As discussed in Sec. 4.2.3, atoms that undergo large transverse excursions through the coupling region can be reflected back into the MMOT, decreasing the magnetic guide flux input.

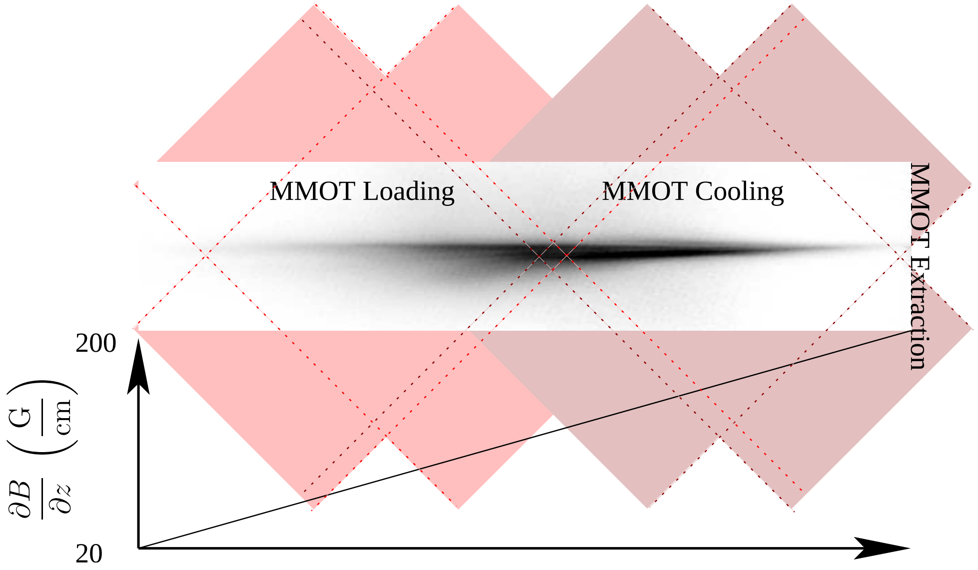

Figure 6.1: Compressed moving MOT. Rather than having a constant field gradient, as in the current setup, the field gradient will increase from 20 G/cm to 200 G/cm. In addition to this increased field gradient, a second pair of MMOT beams, with an average detuning $\delta_{\text{MMOT}} \sim 4\Gamma$.

We have thus considered what we term a “compressed MMOT.” It is well known from standard MOTs that a ramped magnetic-field increase over a time interval of order a few milliseconds leads to a temporary increase of atomic density [67]. The density enhancement in these so-called compressed MOTs can be further enhanced by changing the laser detuning as the magnetic-field gradient is ramped up. In the context of the cw atom laser project it appears natural to look for ways to implement such a scheme in a continuous fashion. This is, in fact, both possible and fairly straightforward. Since in the MMOT the atoms are collected and cooled into a moving frame of reference, a compression effect can be achieved by simply providing a *spatial* increase of the field gradient along the trajectory of an injected atom.

The guide field in the MMOT region can be modified such that it takes the form

$$\mathbf{B} = \begin{pmatrix} \alpha x \\ -\alpha y \\ 0 \end{pmatrix} + \begin{pmatrix} \beta z x \\ -\beta z y \\ \frac{\beta}{2}(x^2 - y^2) \end{pmatrix} . \tag{6.1}$$

This field satisfies $\nabla \cdot \mathbf{B} = 0$ and $\nabla \times \mathbf{B} = 0$. There, α is the gradient of the MMOT magnetic field at the intersection point of the primary atomic beam with the vertical atom guide axis, and the term involving β adds a transverse field gradient that *increases with the height* z in the MMOT region of the guide. Atoms cooled into a moving frame of reference in which all MMOT beam frequencies appear equal will, as they move upward, experience an increasing transverse field gradient. The resultant compressed-MOT effect is similar to normal compressed MOTs [67]. In linear MOT geometries such as in the present case, the compression leads to a reduction in atomic-beam diameter, while the velocity distribution remains practically unchanged.

The results of a simulation shown in Fig. 6.2 indicate that for the moderate choice $\alpha = 40$ G/cm and $\beta = 60$ G/cm^2 the improvement in central collision rate and beam

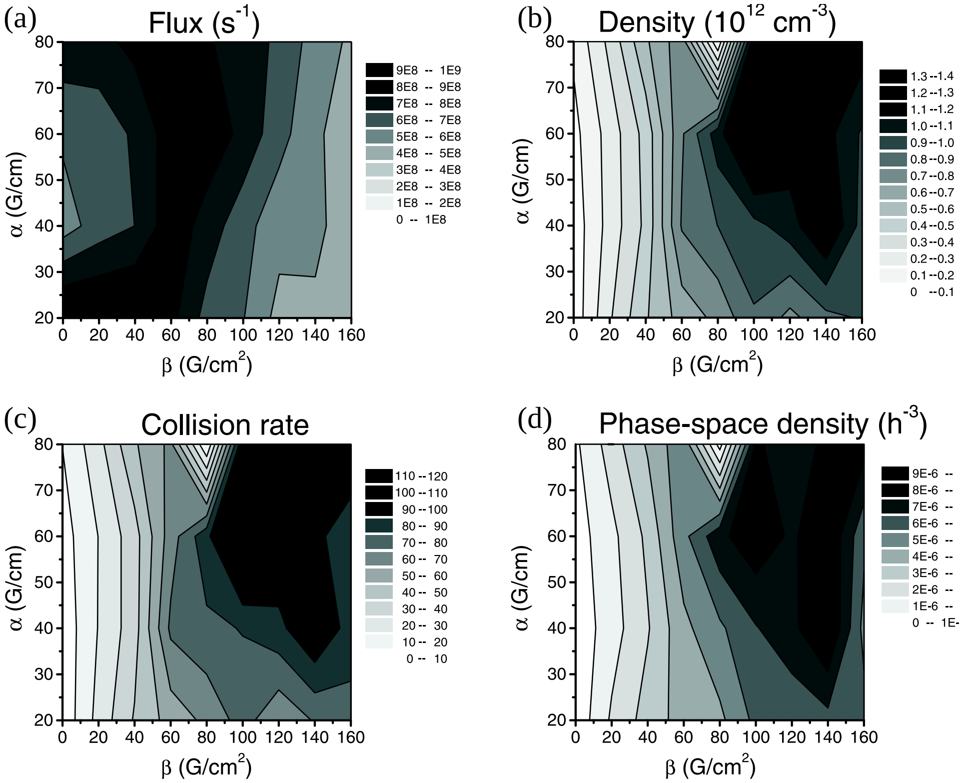

Figure 6.2: Simulation results of the laser cooling in the compressed MMOT. Atoms are injected into the MMOT at a rate of 10^9 s^{-1}. The intensity of the four MMOT beams is 6 mW/cm^2, and their detunings are -2.3 Γ for the down-going and -1.7 Γ for the up-going beams, corresponding to an upward extraction velocity of 2 m/s. The length of the cooling and compression region is 7cm. The panels show gray-scale representations of the following quantities vs the parameters α and β as defined in the text. (a): the output flux, (b): the beam density, the elastic collision rate, and (d) the phase-space density. All data are at the MMOT exit. (b)-(c) are at the beam center.

density should be one to two orders of magnitude over a standard moving-MOT (*i.e.* $\beta = 0$). Further, the compression significantly improves the balancing of kinetic energy E_{kin} and potential energy E_{pot} at the MMOT exit. In a standard MMOT it is $E_{\text{kin}} \gg E_{\text{pot}}$. As a result, the atoms significantly spread out upon their transition from the MMOT into the atom guide, leading to a reduction in density and collision rate. The compressed MMOT reduces the imbalance between E_{kin} and E_{pot} by about a factor of three.

The simulation presents an optimistic picture, because internal radiation pressure effects are neglected. However, even if the central collision rate and the beam density only increased by a factor of order ten, the compressed MMOT may become an essential piece in the realization of cw-BEC. Therefore, it is planned to add field coils in the MMOT region that will allow one to vary the parameter β in Eq. 6.1 from 0 to about 60 G/cm^2. While a general idea of how to design these coils exists, detailed magnetic-field calculations will be necessary before a prototype is built.

6.2 Evaporative Cooling

We have also been focused on creating simulations for the purpose of optimizing various parameters that will lead to the most efficient evaporative cooling and BEC formation. To simulate our system, we employ a direct simulation Monte Carlo (DSMC) method popularized by Bird [52] and thoroughly discussed in Ch. V. This method has been used successfully to simulate evaporative cooling in standard three dimensional BEC formation [68] and Mandonnet et al. [69] and Lahaye and Guéry-Odelin [70] have applied it to a similar magnetic atom guide. Mandonnet et al. [69] showed that evaporative cooling in a guide is possible and Lahaye and Guéry-Odelin [70] have explored a discretized truncation of the evaporation threshold (only two truncations thus far have been simulated). Simulations of the atom guide presented here were done using a parallel algorithm discussed in App. B.

6.2.1 Rethermalization

The key ingredient to efficient evaporative cooling lies in the maintenance of the rethermalization rate, or the rate at which a non-thermal gas can reach equilibrium. This rate sets the limit for the speed of a forced evaporative cooling scheme. As a demonstration of this, we consider a small (30 cm long), specularly reflecting, closed, and initially empty cylinder. An input stream at one edge of the cylinder of 10^9 atoms/s (^{87}Rb) with a longitudinal velocity of 10 cm/s is started at $t = 0$

and allowed to continue until $t = 3$ s. The simulation then continues until $t = 10$ s, during which time the gas in cylinder is allowed to thermalize.

The upper panel of Fig. 6.3 shows the temperatures T_{x}, T_{y}, and T_{y} in the middle of the 30 cm cell as a function of time. In the lower panel of Fig. 6.3 we see the collision rate γ_{coll} in this same location of the cell. The figure shows the probe location first becoming filled with atoms and then reaching thermal equilibrium. From this figure, we see that the rethermalization process begins at $t \sim 3/\mathrm{s}$ (with $\gamma_{\mathrm{coll}} \sim 5\mathrm{s}^{-1}$) and on the order of 10 collisions per atom are required to complete the process at $t \sim 5$s. The most commonly accepted value for the minimum number of collisions (per particle) to thermalize a truncated distrubtion is 5 [68, 71] although as low as 2.7 has been reported. [72]

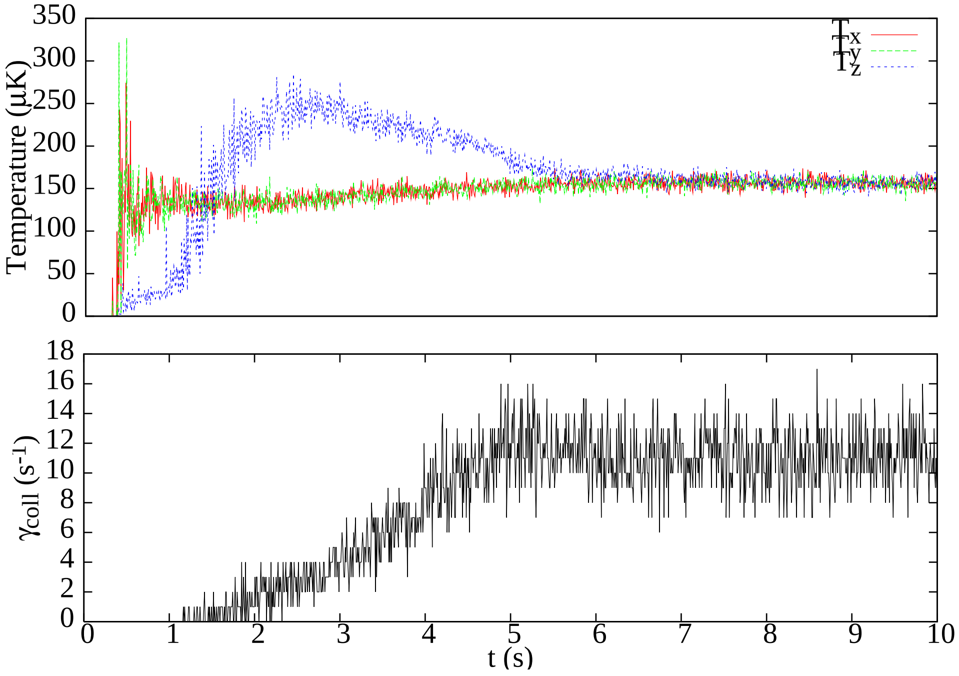

Figure 6.3: Rethermalization shown in the middle of 30 cm cylindrical cell.
Top: Temperatures (T_{x}, T_{y}, and T_{z}) at the specified location as a function of simulated time.
Bottom: Collision rate (γ_{coll}) at the specified location of the cell as a function of simulated time.

To apply this information to the atom guide, consider an atomic beam with velocity $v_{\parallel}$ and collision rate γ_{coll}. The above dictates that the minimum length Δl

over which thermalization can occur is given by

$$\Delta l = \frac{\eta v_{\parallel}}{\gamma_{\mathrm{coll}}} \tag{6.2}$$

where η is the rethermalization rate in pseudo-units of inverse number of collisions (given as 10, 5, or 2.7 above). If then a thermal beam with temperature T_{i} enters a region where the evaporation threshold suddenly decreases by an amount $k_{\mathrm{B}}\Delta T$, the maximum temperature gradient $\partial T/\partial z$ at this point in the guide would then be given by

$$\frac{\partial T}{\partial z} = \frac{\gamma_{\mathrm{coll}}\Delta T}{\eta v_{\parallel}}. \tag{6.3}$$

Eqs. 6.2 and 6.3 imply a minimum length required for evaporative cooling to reach a given minimum temperature. Because it is difficult to predict a priori changes in the collision rate and density along the length of the evaporatively cooled beam, we will at this time forego any speculation of the minimum length required for cooling to a certain phase-space density. The results of the ensuing sections will shed some light on this issue. Suffice it to say that the collision rate must be high enough so that the experiment acceptably fits inside of the basement of Randall Lab.

6.2.2 Evaporative Cooling in the Atom Guide

For the simulations of the guided atomic beam we begin with an initially unfilled guide. At the beginning of each time step, new atoms are added at $z = 0$ with a x, y, and z velocity components given by a thermal distribution as

$$P(x, y, \mathbf{v}) \propto \exp\left[-\frac{M\left|\mathbf{v} - \hat{\mathbf{z}}v_{\parallel}\right|^2}{2k_{\mathrm{B}}T} - \frac{V_{\mathrm{B}}(x, y)}{k_{\mathrm{B}}T}\right]. \tag{6.4}$$

For each of the following simulations, the initial temperature T was set to 150 μK, $v_{\parallel}$ was set to 20 cm/s, and the input flux was set at 5×10^9 s^{-1}. As described in Ch. V, during each time step, collisions between nearest neighbors are calculated and particles are moved according to the guiding Hamiltonian given by

$$H = \frac{p^2}{2m} + \frac{\mu_\mathrm{B}}{2}\sqrt{\left[B_\parallel(z)\right]^2 + \left[B_\perp(x,y,z)\right]^2}\,. \tag{6.5}$$

As allowed by scaling the Boltzman equation (Eq. 5.3), in each of the following simulations, each particle represented 5000 rubidium atoms in the $|F = 1, m_\mathrm{F} = -1\rangle$ state (for which Eq. 6.5 is valid). A refinement-study was performed with representative sizes of 5×10^3, 1×10^4, 5×10^4, and 5×10^5. The final size (5000) of these representative particles was chosen as high as possible without significantly disturbing the collision processes along the length of the guide. It should be noted that a decrease in representative particle size will only result in a larger temperature gradient along the length of the guide, or in other words a better performance of the longitudinal cooling mechansim. These simulations therefore do not represent the best possible result, but are used rather as a lower bound of the performance of the evaporative-cooling portion of the atom laser experiment.

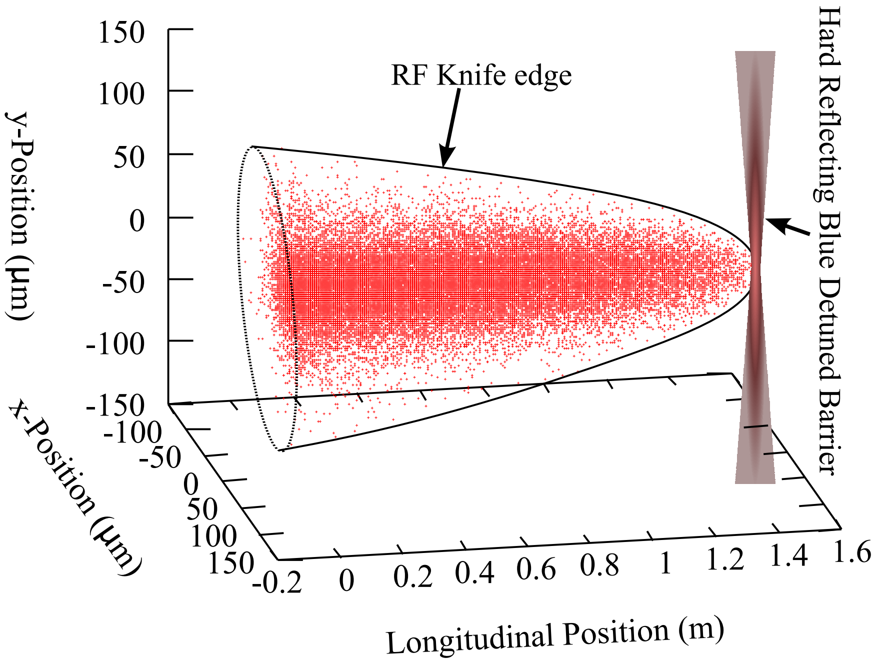

Figure 6.4: Schematic of atom-laser simulation with sheet-of-light barrier.

To simulate the rf-induced removal of atoms, we assume a classical approximation by removing all atoms from the simulation that go beyond a cylindrical surface where the Zeeman splitting from the static field of the trap equals the energy of the rf field given by $h\nu_{\mathrm{rf}}$. Fig. 6.4 is a representative picture of the simulated atomic beam with the rf-removal shell indicated. Also depicted in Fig. 6.4 is a hard-reflecting wall at at the end of the guide. As mentioned in Sec. II.2.6, this wall will be created by a blue-detuned sheet of light and is to help establish a three dimensional trap wherein a condensate can form.

One of the goals of this simulation work is to evaluate the function and efficiency of each of the variables that can be used to alter the evaporation process. These include changing the rf frequency as a function of position, changing the longitudinal magnetic field $B_{\|}$ as a function of position, and tilting the table so as to change the gravitational potential along the length of the guide. In addition to testing the evaporation tools, a scheme is sought whereby degeneracy can be reached. There are two main approaches currently for developing the atom laser. One approach is to cool a moving atomic beam directly into the degeneracy regime while the other approach is to cool an atomic beam into a zero velocity reference frame, thus establishing a steady-state BEC. The following sections will present simulation results that help classify each of these approaches and the tools to be used for them. Although the following has been helpful for the project, it should be noted that it is still in a preliminary phase and more results will follow the writing of this thesis.

6.2.3 Cooling to a Moving Degenerate Gas

6.2.3.1 Variable rf Frequency

For cooling an atomic beam into a moving reference frame, two types of simulations were run, with different control variables to change the evaporation threshold. For the first simulation, ν_{rf} was used as the control variable. This setup closely

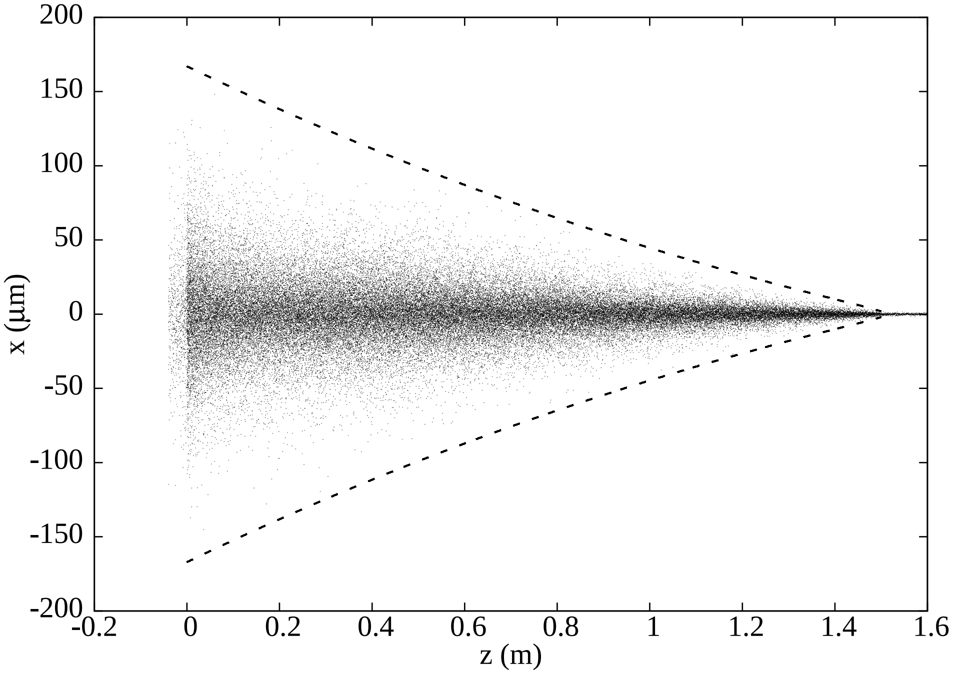

Figure 6.5: Snapshot of the cooled atomic beam by varying the rf frequency ν_{rf}. The particle distribution shown is as projected onto one of the transverse direction. In this simulation, ν_{rf} was varied linearly from 21 MHz to 550 kHz. One can see the obvious increase in spatial density as a function of longitudinal position z.

mimics that of Mandonnet et al. [69], where similar simulations were run for an evaporatively cooled atomic beam. A major difference between this simulation and that of Mandonnet et al. is the magnetic compression applied as a function longitudinal position in the guide. This resembles the experimental setup presented in this work. The purpose of this compression is to enhance the density as a function of position, analogous to timed magnetic compression stages in a magnetic BEC experiment. By enhancing the density as the beam travels through the guide, the collision rate and thus evaporative cooling should be maintained.

Fig. 6.5 shows a snapshot of the atomic beam after steady state has been reached. For simplicity, the energy of the rf knife edge $h\nu_{\mathrm{rf}}$, the physical position of which is also shown in Fig. 6.5, varied in a linear fashion from 21 MHz to 550 kHz. At the end of the guide, a very cold and narrow atomic beam exits the evaporation stage. To

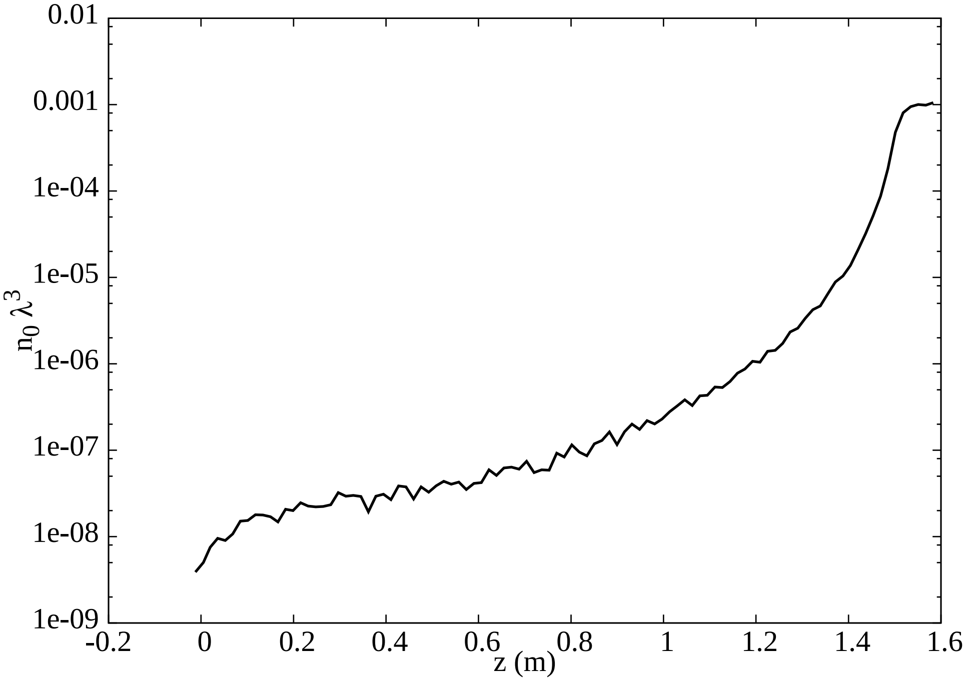

Figure 6.6: Phase space density ($n\lambda_{\mathrm{th}}^3$) increase along the length of the guide by cooling to a moving reference frame using a linearly varying ν_{rf}. In this simulation, ν_{rf} was varied linearly from 21 MHz to 550 kHz. For this plot, only the central portion of the guide was considered (core of 1 μm diameter).

quantify the performance of this simulated beam, we examine the phase-space density $n\lambda_{\mathrm{th}}^3$ as a function of z shown in Fig. 6.6. This figure shows that the $n\lambda_{\mathrm{th}}^3$ increases by about five orders of magnitude. Although final value is not enough for degeneracy, this is a significant increase and may not represent the optimal conditions. For example, as the density and collision rate increase, the length of guide needed for thermalization decreases (see Eq. 6.2). Thus a more optimum variation of ν_{rf} would be more exponential (although more technically difficult). [1]

6.2.3.2 Fixed rf Frequency; Variable $B_{\parallel}$

In the second attempt to simulate cooling in a moving reference frame, ν_{rf} was held fixed at 24 MHz while $B_{\parallel}$ varied linearly from 0.6 mG to $\approx$ 32 G. This method of changing the evaporation threshold is analogous to raising the bottom of a bucket

---

[1] I should point out that this simulation is the result of approximately 200 days of CPU time, or 160 hours on a 32 processor cluster. I am very grateful for the use of the cluster.

(while keeping the top fixed) and thus spilling the contents over the edges. Figs. 6.7 and 6.8 show a snapshot of the steady state beam and the associated phase-space density at the core of the guide respectively. It is obvious from this data that this simulation failed to show any advantage to using $B_{\|}$ for changing the threshold. The failure of this simulation stems from the fact that while raising the bottom of the magnetic trap, an increase in $B_{\|}$ also makes the trap much less confining. The result is to dramatically decrease the collision rate and thus kill the rethermalization process, as shown in the temperature plot in Fig. 6.9.

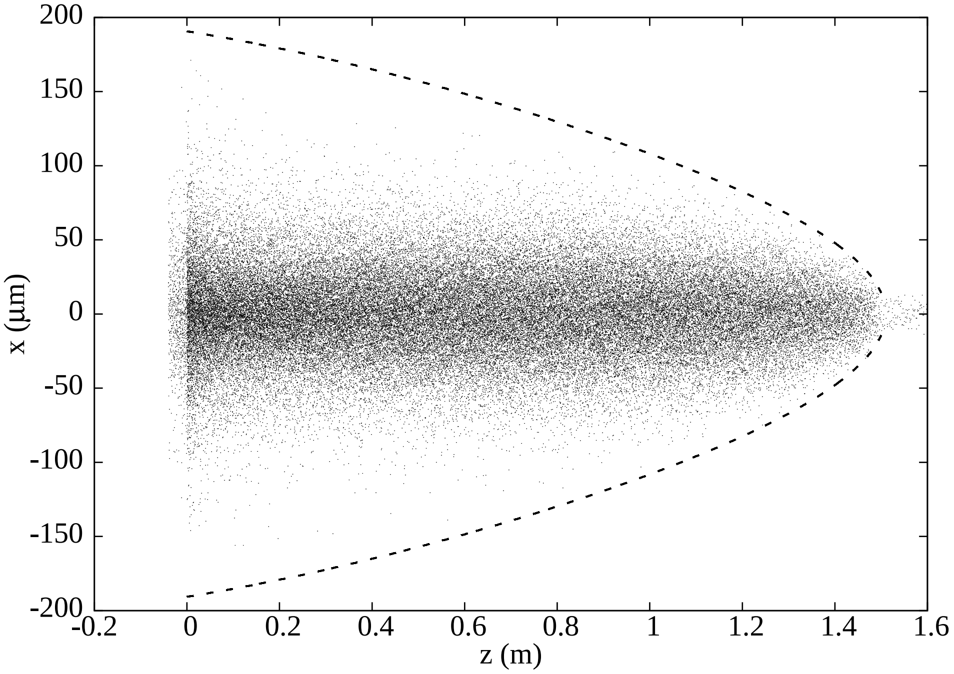

Figure 6.7: Snapshot of the atomic beam cooled by linearly varying the longitudinal field $B_{\|}$. The particle distribution shown is as projected onto one of the transverse direction. In this simulation, $B_{\|}$ was varied linearly from 0.6 G to 34 G. It is clear from this figure that spatial density is not enhanced.

Fig. 6.7 also possibly shows that the situation might be improved by using a more aggressive change in $B_{\|}$. Fig. 6.10 shows such a atomic beam where $B_{\|}$ was varied in an exponential manner. Unfortunately, this complicates the matter by changing the longitudinal force in a non-linear manner, such that simple gravitational

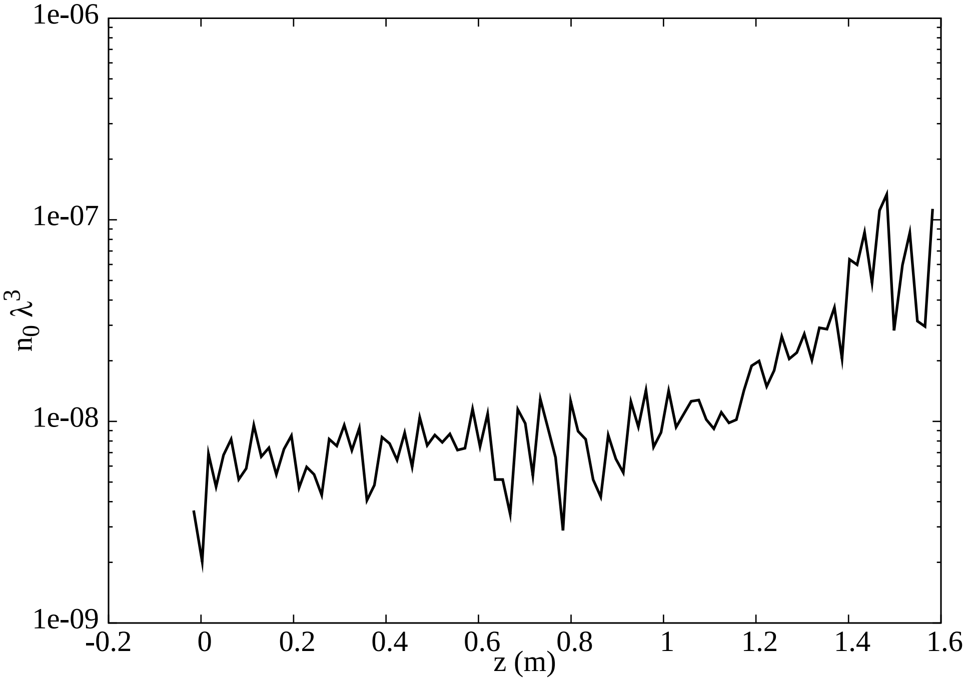

Figure 6.8: Phase space density ($n\lambda_{\mathrm{th}}^3$) increase along the length of the guide by cooling to a moving reference frame using a linearly varying $B_{\|}$. In this simulation, ν_{rf} was held fixed at 24MHz while $B_{\|}$ varied linearly from .6 G to 32 G. For this plot, only the central portion of the guide was considered (core of 1 μm diameter).

compensation (by tilting a table) is not possible. The result is to create a shallow trap at about $z = 25$ cm, not too far from the atom source at $z = 0$ with $T = 150\ \mu$K. We conclude therefore that a variable $B_{\|}$, by itself, is not practical for realizing an evaporatively cooled atomic beam.

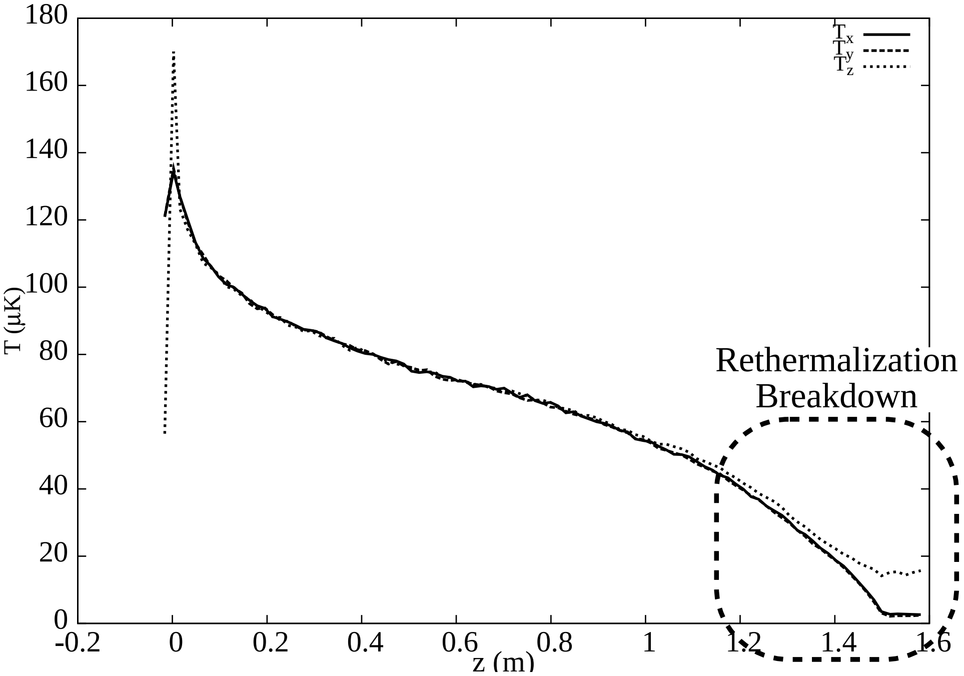

Figure 6.9: Temperature decrease along the length of the guide by cooling to a moving reference frame using a linearly varying $B_{\|}$. In this simulation, $\nu_{\rm rf}$ was held fixed at 24MHz while $B_{\|}$ varied linearly from .6 G to 32 G. For this plot, only the central portion of the guide was considered (core of 1 μm diameter).

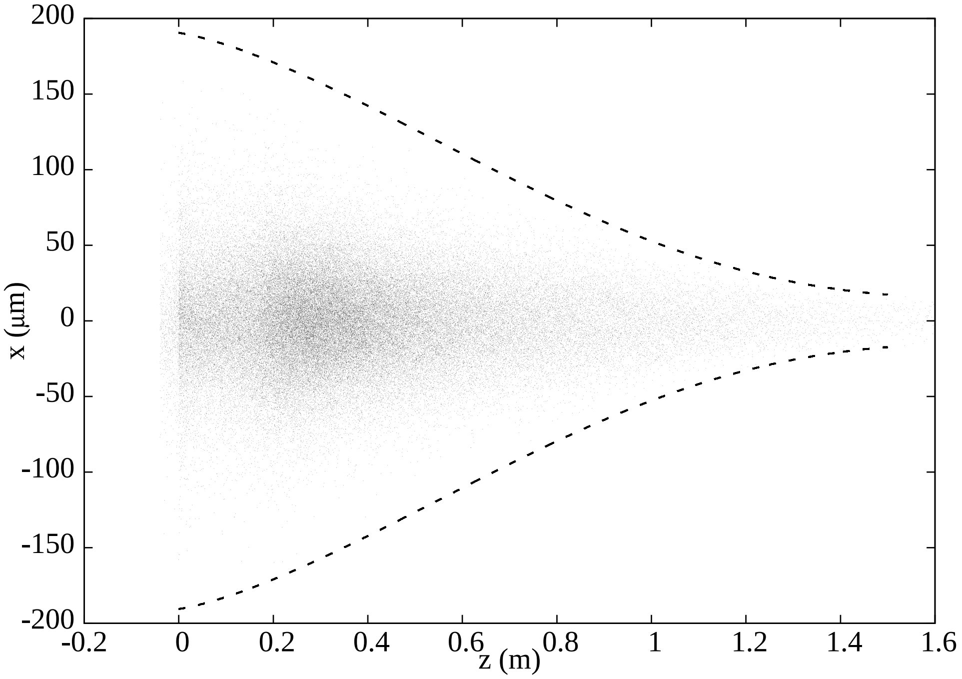

Figure 6.10: Snapshot of the atomic beam cooled by exponentially varying the longitudinal field $B_{\|}$. The particle distribution shown is as projected onto one of the transverse direction. $B_{\|}$ is varied much more aggressively with an exponential increase from 0.6 G to 34 G. It is clear from this figure that spatial density is not enhanced.

6.2.4 Cooling to a Stationary BEC

6.2.4.1 From a $\langle v_{\|} \rangle > 0$ Atomic Source

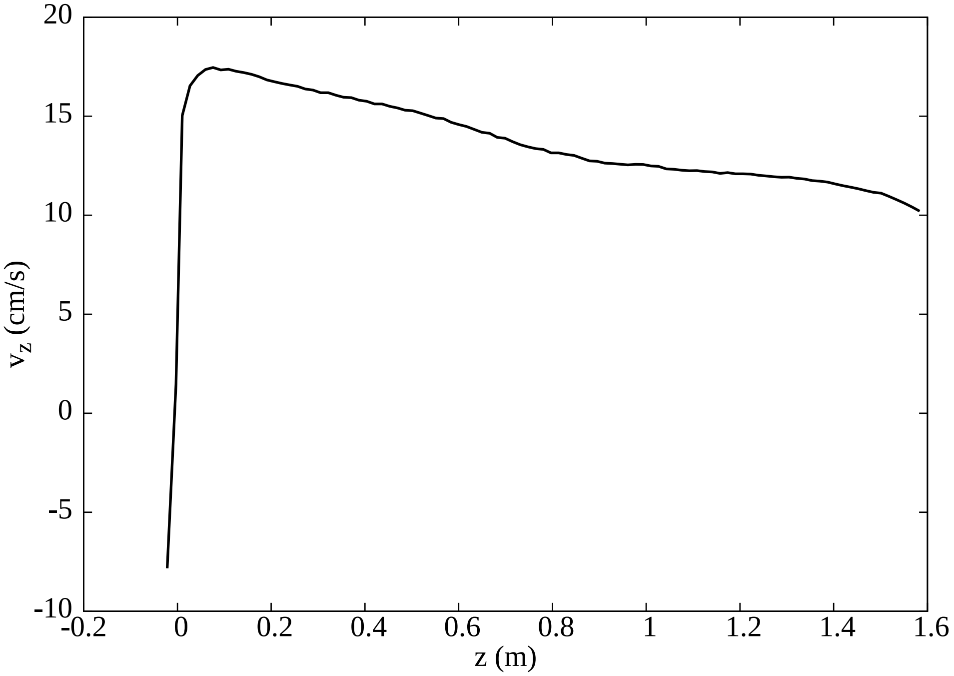

Figure 6.11: Longitudinal velocity ($v_{\|}$) decrease along the length of the guide by cooling to a stationary reference frame using a linearly varying ν_{rf} and positive gravitational potential. In this simulation, ν_{rf} was varied linearly from 21 MHz to 550 kHz. For this plot, only the central portion of the guide was considered (core of 1 μm diameter).

One method which might be used to cool an atomic beam into a stationary BEC is to slow an initially moving beam to $\langle v_{\|} \rangle = 0$ at the end of the guide. The most practical control variable for removing the longitudinal energy is the tilt applied to the guide, such that atoms are forced to climb a gravitational potential. A simulation was run wherein the guide was tilted uphill by 2 mm over the length of 1.6 m. This gravitational gradient is enough to stop the average forward motion of an atomic beam, with $v_{\|} = 20$cm/s initially, at ≈ 1.6 m. The conditions for this simulation are otherwise the same as described in Sec. 6.2.3.1.

Fig. 6.11 shows how $v_{\|}(z)$ decreases through the guide. This figure shows that the 2 mm rise over the length of the guide failed to slow the beam to a stationary

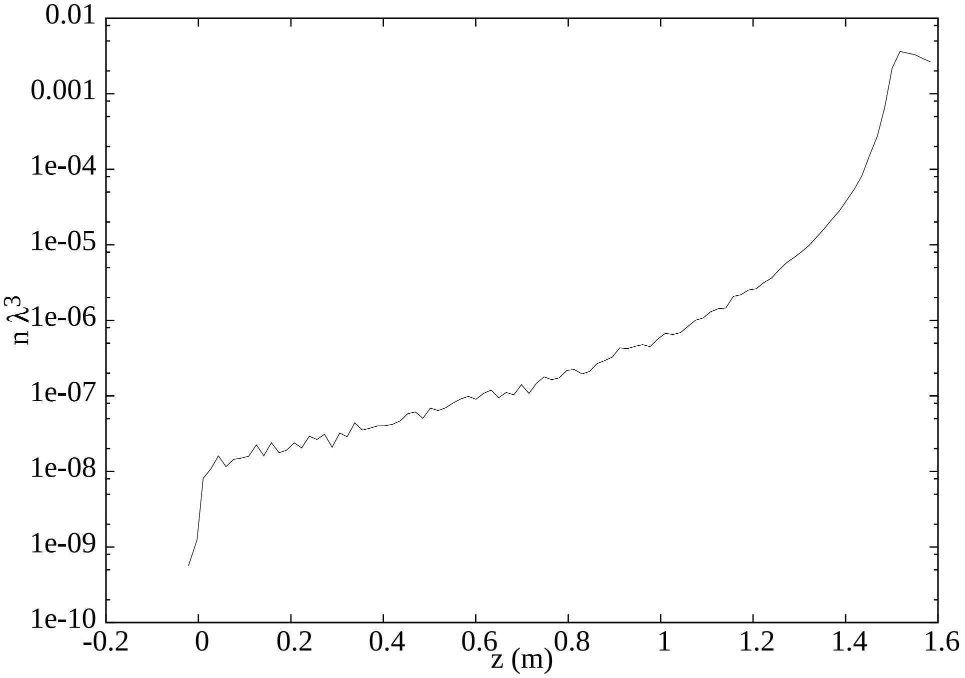

Figure 6.12: Phase space density ($n\lambda_{\mathrm{th}}^3$) increase along the length of the guide by cooling to a stationary reference frame using a linearly varying ν_{rf} and positive gravitational potential. In this simulation, ν_{rf} was varied linearly from 21 MHz to 550 kHz. For this plot, only the central portion of the guide was considered (core of 1 μm diameter).

frame. The 2 mm rise was chosen assuming a collisionless gas, or in other words, the collisions in the beam transfered thermal energy into the common mode energy of the beam. Fig. 6.12 shows the increase of $n\lambda_{\mathrm{th}}^3$ as a function of guide position. This figure shows an even higher phase-space density increase than for the simulation discussed in Sec. 6.2.3.1. Although more simulations will have to be done, this evaporation scheme shows promise for reaching degeneracy in a stationary frame at the end of the guide.

6.2.4.2 From a $\langle v_{\parallel} \rangle = 0$ Atomic Source

While it is apparent that cooling a moving atomic beam into a stationary degenerate gas might be possible, one might assume that by beginning with a $v_{\parallel} = 0$ atomic source, the task might even be easier. For this case, the system would be entirely pressure driven and would have a near-zero average velocity throughout the guide. Because the system is pressure driven with a very low stream velocity, it is expected that a much shorter atomic guide might be possible. This is focus of a current simulation effort. For technical reasons, the input flux for this simulation was set at 1×10^9 s^{-1}. Preliminary results in Fig. 6.13 show the phase-space density increase as well as the velocity dependence along the length of the guide. [2] Fig. 6.13 shows that the phase-space density does indeed increase by about 5.6 orders of magnitude with a final velocity around 5 cm/s. It is expected that a larger increase in flux (by a factor of 5 to match the input flux of the other simulations) that the final phase-space density will dramatically increase.

---

[2] This is the longest type of simulation to run as we rely of purely kinetic motion of particles to fill the beam.

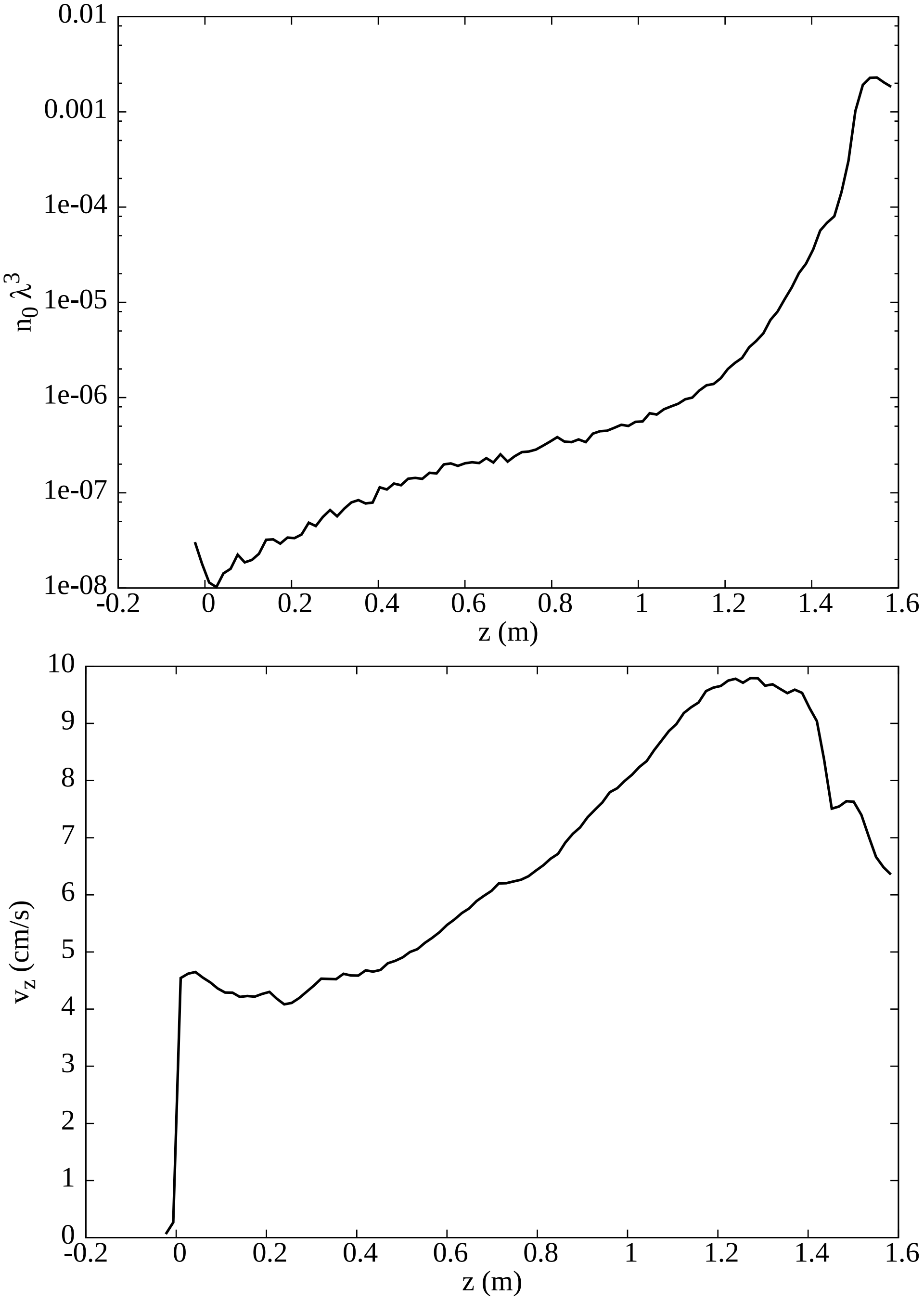

Figure 6.13: Phase space density ($n\lambda_{\mathrm{th}}^3$) and velocity dependence along the length of the guide with a $v_\parallel = 0$ atomic source. Thermal truncation is performed by linearly varying ν_{rf} from 21 MHz to 550 kHz. For this plot, only the central portion of the guide was considered (core of 1 μm diameter).

CHAPTER VII

Summary of Experimental and Numerical Results

7.1 Summary of Experimental Results

Experimentally, we have realized a continuous flow of atoms in a 1.7 m long magnetic guide and measured longitudinal and transverse temperatures of the guided atomic beam. We have further demonstrated continuous rf-induced removal of the most energetic atoms from the guide. As of yet, there is no evidence that elastic collisions play a role in the observed atom-beam dynamics. In context with the long-term goal of this project, which is to generate a continuous-wave, amplitude- and phase-stable coherent atomic beam, the next step will be to demonstrate rf-induced evaporative cooling in the horizontal section of the guide, as has been proposed earlier [31, 32, 69, 73]. The work presented in this thesis lays important foundations for the realization of these ideas. The challenge for the future will be to obtain collision rates high enough that the atom evaporation causes a strong increase in phase-space density of the atomic beam. It should be noted that related work performed at ENS, Paris [51] has now recently resulted in such a demonstration of evaporative cooling in a magnetic guide [41].

7.1.1 Single Mode Filtering

The end result of this project will be the cw atom laser—a cw amplitude- and phase-stable coherent matter wave—and will be the ideal atom source to operate atom-interferometric devices. In atom interferometers, relative phase shifts of de Broglie matter waves can be utilized to measure atomic accelerations due to electromagnetic fields [74], gravitational fields [75], rotations [76], and interactions with other atoms [77, 78]. The recent surge of interest in atom interferometry stems from this wide range of potentially detectable phenomena and the associated high precision due to the short de Broglie wavelength of matter waves in the velocity range of interest ($\lesssim 1$ m/s to a few 10 m/s) [79].

Another approach to build atom-interferometric devices can be compared to white-light interferometry. Just as white-light optical interferometry is possible using nearly matched optical path lengths, precise atom interferometry may be possible using a reasonably mono-energetic beam of atoms [80]. In other words, a filter properly applied to a thermal atomic beam could result in a reasonably mono-energetic beam useful for atom interferometry. As in this experiment, a continuously applied rf current for the removal of atoms may make such a filtering scheme possible.

To evaluate the performance of the achieved atomic beam, we calculate the number of quantum-mechanical atom-guide modes occupied with the rf filter applied. We use a semi-classical analysis in cylindrical coordinates to calculate the number of modes in the plane transverse to the guide axis. The number of modes with an outer turning point less than ρ_0 is given by

$$N_{\mathrm{modes}} = \sum_{m=-\infty}^{\infty} \frac{2}{h} \int_{\rho_{\mathrm{min}}}^{\rho_0} \sqrt{2M \left(E_{\mathrm{m}}\left(\rho_0\right) - E_{\mathrm{m}}\left(\rho\right)\right)} d\rho$$

where the potential energy $E_{\mathrm{m}}(\rho)$ of mode m is given by

$$E_{\mathrm{m}}(\rho) = \frac{\hbar^2 \left(m^2 - 1/4\right)}{2\rho^2} + \left| \frac{\partial B}{\partial \rho} \mu_{\mathrm{B}} g_{\mathrm{F}} \right| \rho \ ,$$

the angular momentum about the guide axis $l_{\mathrm{z}} = \hbar m$, and ρ_{min} is defined by $E_{\mathrm{m}}(\rho_{\mathrm{min}}) = E_{\mathrm{m}}(\rho_0)$ (let $\rho_{\mathrm{min}} \rightarrow 0$ for $m = 0$). To estimate the number of modes that carry a significant flow, Fig. IV.4.14 is used to estimate ρ_0. For the case when no rf is applied, $\rho_0 \approx 100\ \mu\mathrm{m}$ and we obtain $N_{\mathrm{modes,no\ rf}} = 3.5 \times 10^8$. By applying the rf-induced energy filter, $\rho_0 \approx 40\ \mu\mathrm{m}$ and we obtain $N_{\mathrm{modes,with\ rf}} = 3.6 \times 10^7$. Assuming the atom flux is the same in all significant guide modes, the flux per mode is then about $\Phi_{\mathrm{m}} = 0.2\ \mathrm{s}^{-1}\mathrm{mode}^{-1}$. If one were to build an atom interferometer based on filtering the atomic beam in a way that only the fundamental guide mode enters the interferometer, flux-per-mode would correspond to the count rate. Reasonable experiments will require a count rate of order $10^3\ \mathrm{s}^{-1}$. Therefore, an increase of the phase-space density by a factor of order 10^4, combined with mode filtering techniques, will be sufficient to perform atom-interferometric experiments in the guide. This increase could be obtained by implementing a larger initial flux and some degree of evaporative cooling enabled by an improved collision rate. (Improvements along these lines are discussed in Ch. VIII.) Further, the present phase-space density, estimated to be $h\Phi_{\mathrm{m}}/(M \Delta v_{\mathrm{z}} \langle v_{\mathrm{z}} \rangle) \sim 10^{-9}$, needs to be increased by a factor of order 10^9 to reach a quantum-degenerate atomic flow.

7.2 Summary of Numerical Results

One of the goals of our simulation work pertains to the evaluation of each of the control variables used to alter the evaporation threshold. Our simulations have clearly shown the benefit of using a variable rf frequency ν_{rf} along the length of the guide. It is apparent that this method is quite robust in increasing the phase-space density $n\lambda_{\mathrm{th}}^3$ by several orders of magnitude.

These simulations have also clearly shown the difficulties, if not impossibilities, of using only a change in $B_{\|}$ to raise the bottom of the trap, and thus change the evaporation threshold. It may still be possible to use $B_{\|}$ as a control variable along the length of the guide, but it is clear that a more complicated variation in the gravitational potential would be necessary. It is also evident that high values of $B_{\|}$ should be avoided as the confinement of the trap must necessarily remain tight so as to maintain the collision rate. In passing, we should also mention that it would be physically very difficult to compensate the rounding of the trap due to a high $B_{\|}$ by changing $B_{\perp}$ from the DC wires. Minimum wire spacing as well as maximum current are limited by size and resistivity of the wire (perhaps a superconducting wire might help here).

We have furthermore obtained promising results that show that cooling to both a moving degenerate gas, as well as to a stationary BEC might be possible by using a varying ν_{rf} along the length of the guide. Although no final, best evaporative solution has been found, our simulations have made significant progress and have been helpful in planning for the next iteration of the atom guide.

CHAPTER VIII

Future Directions

The long-term goal of this project is to generate a continuous-wave (cw), amplitude- and phase-stable coherent atomic beam, or cw atom laser. This atom laser will be the ideal atom source to operate atom-interferometric devices. The next major milestone of this project is to demonstrate significant gain in phase-space density along the length of the guide via evaporative cooling. Achieving this milestone within the 1.7 m length of our guide entails overcoming a few major obstacles. First and foremost, the input flux of the guide must be increased. Second, the injection of atoms into the magnetic guide must be improved, such that (1) coupling efficiency is increased, (2) adiabatic heating is avoided, and (3) an initially slower atomic beam is produced. In this chapter, we first discuss several improvements that are either currently underway or in being considered for future designs. This chapter will end with an brief description of alternative atom guides that could be explored.

8.1 Improvements of Present Experiment

8.1.1 Input Atomic Flux

The most important improvement to this system will be an increase of the input flux. While the pyramidal LVIS implemented in the first iteration of our atom guide is low cost, easy to set up, and easy to maintain, it does not produce a primary atomic

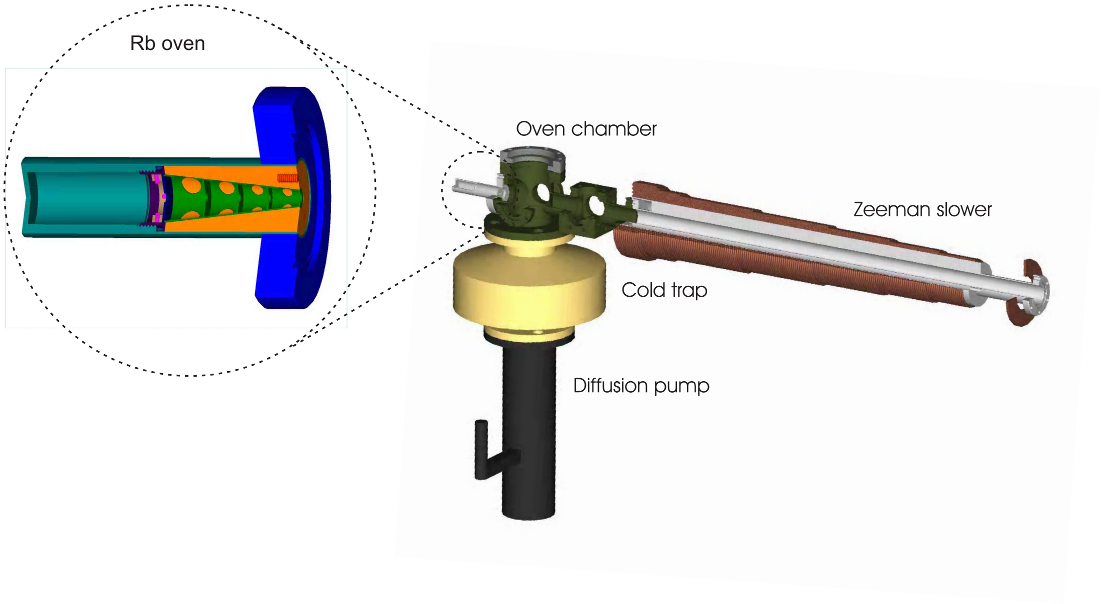

Figure 8.1: Rendering of a CAD drawing used to design the new Zeeman slower. Image courtesy of Rahul Mhaskar.

beam with a high enough output flux to drive evaporative cooling. Our replacement atom source (soon to be coupled to the guide) is a Zeeman slower, as depicted in Fig. 8.1.

Fig. 8.2 shows preliminary measurements of the atomic beam generated from the Zeeman slower. Using an absorption measurement similar to that discussed in Ch. IV, we have found a usable (slow enough to be recaptured by laser cooling) maximum flux with 6% absorption. This corresponds to $\sim 4 \times 10^{11}\text{s}^{-1}$ at 40 m/s and $\sim 2 \times 10^{11}\text{s}^{-1}$ at 20 m/s. In Ch. IV we discussed the atomic flux measured throughout our current setup and the associated collision rate within the horizontal section of the magnetic guide. With the PMOT output flux $\Phi_{\text{PMOT}} \approx 3 \times 10^9\ \text{s}^{-1}$ the elastic collision rate in the guide is $\sim 0.5\ \text{s}^{-1}$. This is approximately 100 times too low for efficient evaporative cooling in a 1.5 m guide (this is also confirmed by the simulations). Therefore, with an output flux two orders of magnitude higher than

Φ_{PMOT}, the Zeeman slower promises to bring the system directly into the collisional regime.

8.1.2 Guide Coupling

As shown in Ch. IV, our current atom guide injection suffers from non-negligible adiabatic heating through the vertical launch section of the magnetic guide. In addition, the initial value of $v_\|$ in the guide is too high to allow for many rethermalization cycles along the length of the guide (assuming that the Zeeman slower helps increase the initial collision rate by a factor of 100). The next iteration of the injection stage will therefore need to reduce its heating mechanisms as well as the value of $v_\|$ delivered to the horizontal magnetic guide.

A possible solution for the injection problem is shown in Fig. 8.3. In this situation, the atom-guide injection is performed by an auxiliary guiding light potential. With this approach it will not be necessary for the MMOT to actually cool into a moving reference frame. Because the MMOT only traps in two dimensions, the natural axial leak of the MMOT might be captured by the guiding light potential. Such a slow loading mechanism will allow optimal cooling in the MMOT and will avoid ballistic heating. Although the optical guide will trap all Zeeman sublevels, only the $m_{\mathrm{F}} = 0$ level will reach the center of the magnetic guide. At this point, a stimulated Raman adiabatic passage (STIRAP) transfer in the guide will be necessary to transfer all $m_{\mathrm{F}} = 0$ atoms into the $|F = 2, m_{\mathrm{F}} = 2\rangle$ state. The STIRAP transfer will rely on atoms passing through spatially separated laser beams. By using a coherent STIRAP transfer, spontaneous photons are not scattered into the trapped atomic beam. It will also be necessary for the magnetic trap depth to exceed the optical trap depth.

A slightly more exotic version of Fig.8.3 is shown in Fig. 8.4. In this case, the freely propagating optical guiding potential is replaced by a hollow-core fiber guide.

By coupling blue-detuned light into the shell of the hollow-core fiber, atoms are guided in the center of the fiber at the evanescent field minimum of the light. Fatemi et al. [81] recently demonstrated this using a micro prism embedded into the side of the fiber to couple in the light. By coating the ends of the fiber with a mirror surface, the guiding light is be contained within the fiber. Thus, coupling atoms into and out of the optical guide does not involve atoms traversing stray optical fields.

As discussed in Ch. VI, we have numerically explored transforming our MMOT stage into a longitudinally compressed MMOT. With a field gradient increase from ~ 20 G/cm to ~ 200 G/cm within the MMOT light field, based on simulations, we expect improvements in the initial phase-space density (by about a factor of 10) and the initial collision rate in the horizontal section of the guide.

8.2 Alternative Atom Guides

I conclude this thesis with a brief description of an alternative type of atom guiding that we have been considering. Fig. 8.5 shows a cross section of the potential created by one DC wire (at 300 A) and one rf wire (5 A) aligned such that gravity is parallel to a line from the DC wire to the rf wire. In this configuration, it is possible to create a two dimensional trap, or an atom guide. For the following discussion, we set the center of the DC wire as the origin. Radial confinement is determined by the difference between the rf frequency ν_{rf} and the Larmor frequency ν_0 (see Ch. I). A trace of the potential and its gradient as a function of the radial coordinate ρ is shown in the lower two panels of Fig. 8.6. For the azimuthal direction, confinement is provided by a variation in the strength of the rf field projected into the direction perpendicular to the DC field. An azimuthal trace of the potential and its gradient are also shown in the top two panels of Fig. 8.6. This figure shows a minimum of the trap where each of the transverse oscillation frequencies are quite close to each other. By varying the various parameters of the setup (rf current, DC current, ν_{rf}, and the separation between the rf wire and the DC wire), it is possible to change the aspect ratio and shape of the minimum of the trap. For example, by moving the two wires closer together, the trap minimum becomes more triangular and less confining as shown in Fig. 8.7. As the wires continue to move together this triangular minimum fades away and the trap become very asymmetric between the radial direction and the azimuthal direction.

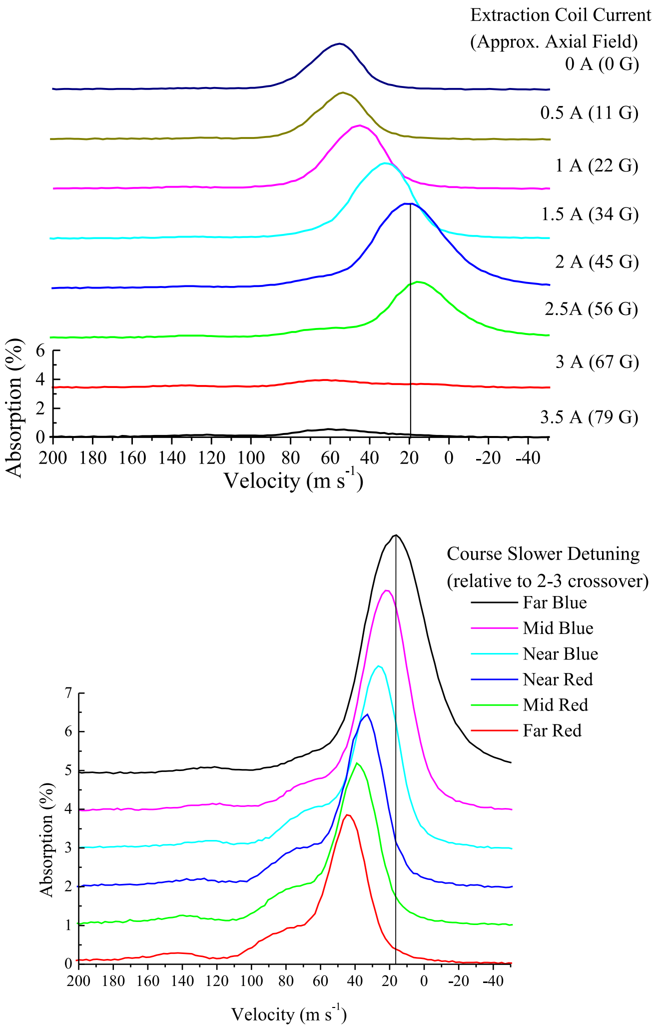

Figure 8.2: Preliminary measurements of the atomic beam generated by the Zeeman slower. Top: Absorption of probe beam vs. the extraction coil current. Bottom: Absorption of probe beam vs. the cooling beam detuning (relative to the $F = 2 \rightarrow F = 3$ cross over peak of a saturated absorption spectrum). Courtesy of Rahul Mhaskar.

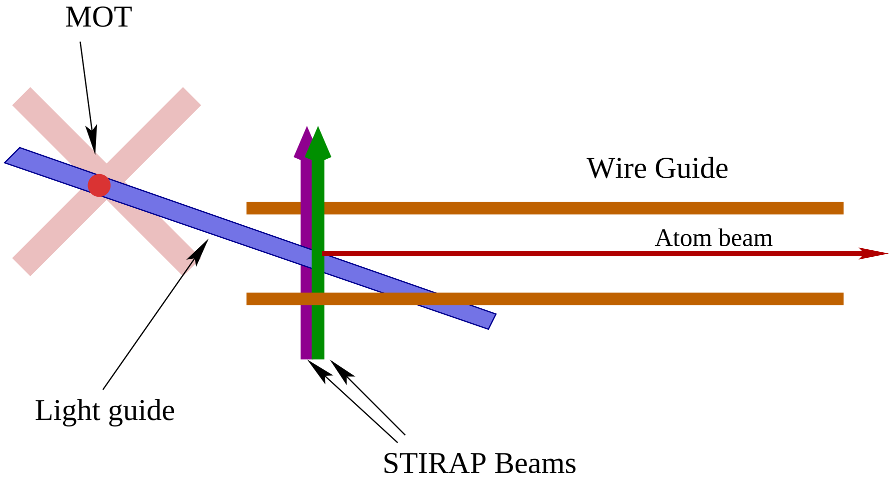

Figure 8.3: Coupling from MOT to magnetic atom guide provided by a guiding light potential.

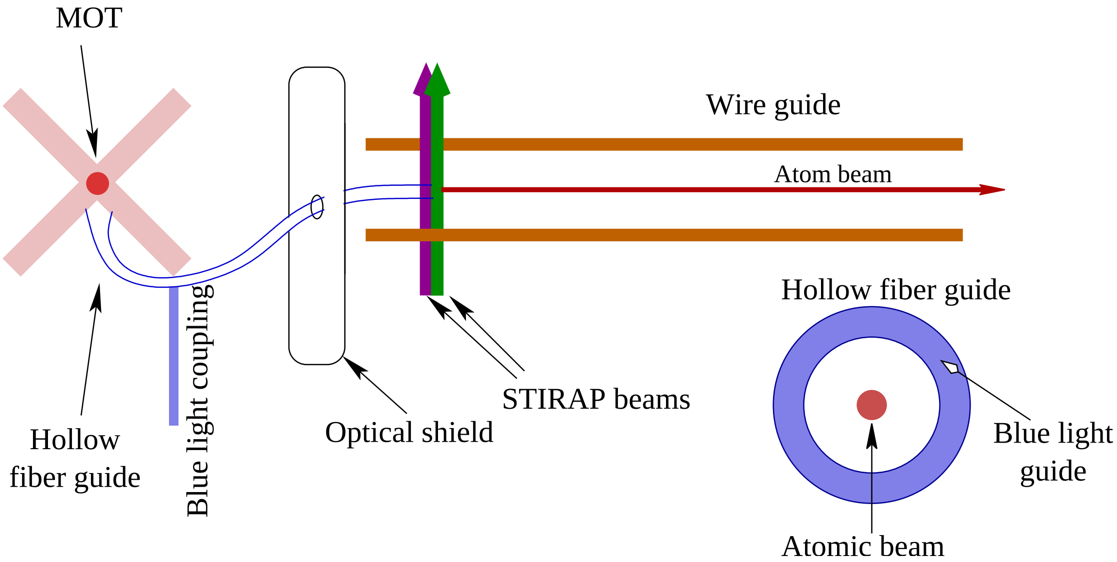

Figure 8.4: Coupling from MOT to magnetic atom guide via a hollow-core fiber with a blue-detuned guiding light potential.

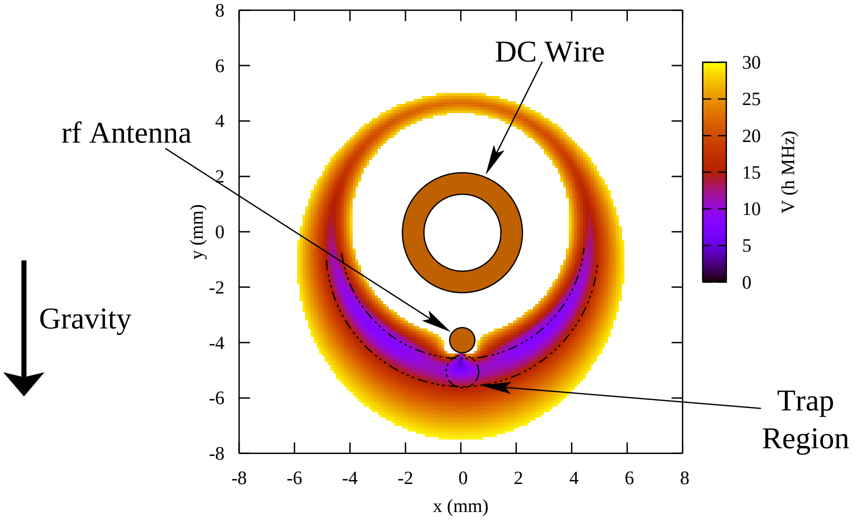

Figure 8.5: Cross section of an effective potential (with rf-coupling) created by one DC wire (at 300 A) and one rf wire (5 A). Gravity is parallel to the line from the DC wire to the rf wire.

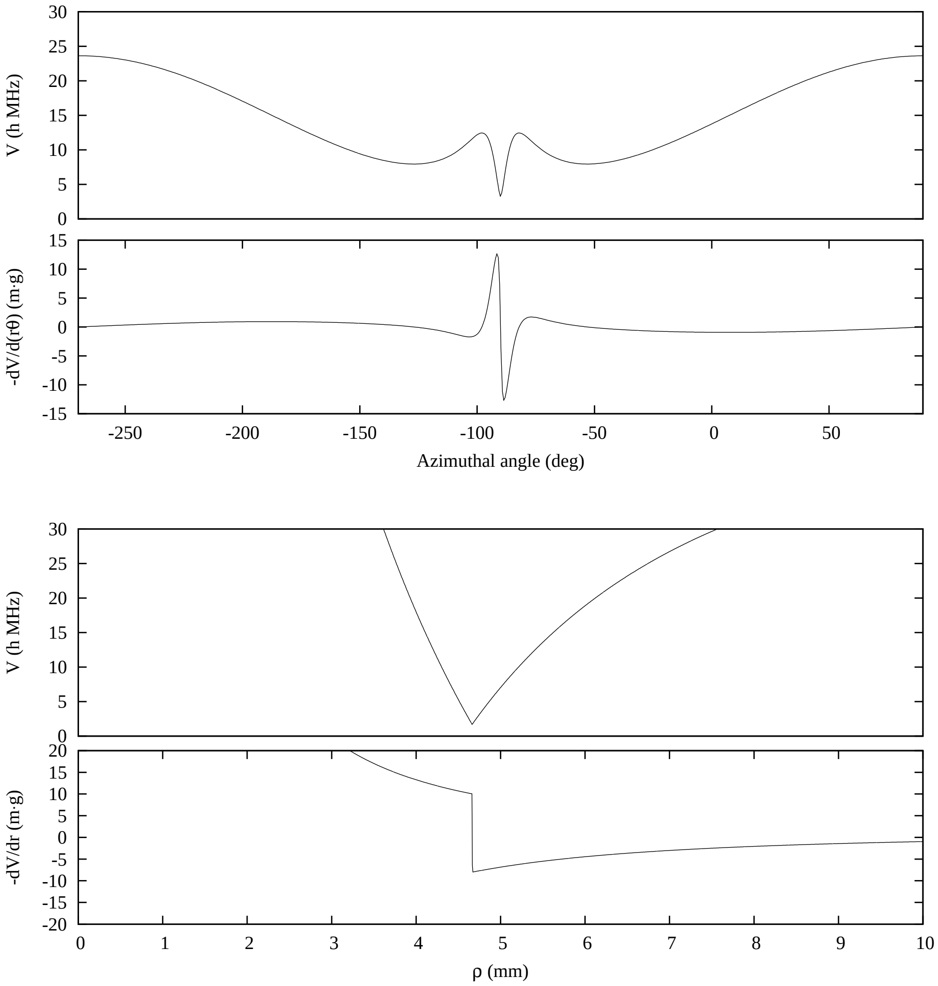

Figure 8.6: The azimuthal component of the gradient of the potential shows the acceleration on atoms in the trap as a function of position. From this figure, it is apparent that gravity is indeed overcome in the azimuthal direction at about $\phi = \pm 30^{\circ}$.

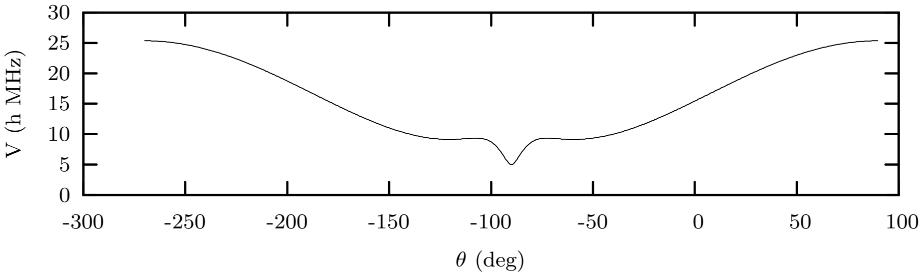

Figure 8.7: The azimuthal component of the gradient of the potential shows the acceleration on atoms in the trap as a function of position. From this figure, it is apparent that gravity is indeed overcome in the azimuthal direction at about $\phi = \pm 30^\circ$.

APPENDICES

APPENDIX A

Time-Averaged, Multi-mode, Optical Fiber Output for Laser Cooling

We demonstrate a method for increasing the amount of power available for laser cooling applications by using a multi-mode optical fiber. By randomizing phase shifts of modes within the fiber on time scales faster than the center-of-mass response time of the atoms, a smooth time-averaged trapping beam is generated. The principle has been demonstrated in a pyramidal magneto-optical trap (MOT). The method is particularly suitable for harnessing the high output power of broad-area diode lasers (BALs) for laser cooling.

A.1 Introduction

Diode laser systems provide a relatively inexpensive and reliable source of laser light for experiments using laser cooling and trapping techniques.[82–84] However, these sources have two properties which can limit their usefulness in such experiments. The first limitation is the low output power provided by many tunable external cavity diode lasers (ECDL). This problem can be resolved by using a separate diode, such as a broad-area diode laser (BAL), for amplification.[85] The second limitation is the non-Gaussian spatial mode of many diode lasers, particularly BALs. The most common solution to this second problem is to spatially filter the light through a single-mode optical fiber. While being effective spatial filters, single-mode optical fibers are limited to low coupling efficiencies and are very sensitive to beam walk and pointing instabilities. Multi-mode fibers have a much higher coupling efficiency and are more stable, but are characterized by a high-contrast speckle pattern at their output which prevents their use in laser cooling and trapping. In this paper, we describe a method for circumventing the problem by time-averaging the speckle pattern of the multi-mode fiber on a time-scale faster than the response time of the atoms to optical forces. The resulting effective beam profile is sufficiently smooth to operate a magneto-optic trap (MOT)[30].

A.2 Time-averaged smoothing

The multi-mode fiber is capable of propagating multiple spatial modes simultaneously, allowing for properties of individual modes to vary independently. To obtain effective time-averaged smoothing of the multiple spatial modes in the fiber, the phase $\delta_{\rm n}(t)$ of each mode should be varied by more than 2π on time scales faster than the response time τ of the atoms in the trap. A lower bound of the response time τ is given by the time it takes an atom starting at rest to traverse the atom trap under the influence of a maximum radiation pressure force $F_{\rm rad} = \Gamma\hbar\omega/(2c)$,

$$\tau \gtrsim \left(\frac{2\phi mc}{\hbar\omega\Gamma}\right)^{1/2}$$

where ϕ is diameter of the trap, $\omega/2\pi$ the frequency of the optical transition, m the mass of the atom, and Γ the decay rate of the excited state. Assuming a typical MOT size $\phi = 1$ mm, we find $\tau \approx 100\mu s$ for Rb. This indicates that phase modulation frequencies of order 10 kHz will be sufficiently large for effective time-averaging.

The time-averaged smoothing can be understood by using a simplified model for the speckle pattern. After collimation, the instantaneous multi-mode fiber output can be represented by an interference pattern of plane waves

$$\mathbf{E} = \sum_{\mathrm{n}} \mathbf{E}_{\mathrm{n}}(t) \exp\left(i[\mathbf{k}_{\mathrm{n}} \cdot \mathbf{x} - \omega t + \delta_{\mathrm{n}}(t)]\right)$$

where fields $\mathbf{E}_{\mathrm{n}}$ and wave-vectors $\mathbf{k}_{\mathrm{n}}$ are associated with the fiber's n-th spatial mode. The number and angular range of the relevant modes depends on the type of fiber and the way the light is coupled into the fiber. The time-dependence of $\mathbf{E}_{\mathrm{n}}$ accounts for (possible) variations of mode-couplings within the fiber, while the time-dependence of the phases $\delta_{\mathrm{n}}(t)$ is caused by deliberately induced length variations in the fiber. Assuming constant mode amplitudes, a phase modulation frequency $> 1/\tau$, and modulation amplitudes of all phase differences $\gtrsim 2\pi$, the atoms will respond to a time-averaged intensity $\propto \langle|\mathbf{E}|^2\rangle \approx \sum_{\mathrm{n}} |\mathbf{E}_{\mathrm{n}}|^2$, *i.e.* a smooth profile with greatly reduced speckle visibility.

A.3 Apparatus

The phase variations required to eliminate the speckle pattern are generated mechanically using a short cylindrical piezoelectric actuator (PolytecPI PT.130.40, diameter of 20mm) and the multi-mode fiber (ThorLabs FT-200-EMT, NA 0.39, core diameter 200 μm). Approximately one meter of fiber is coiled fifteen times around the cylindrical surface of the actuator and attached with epoxy. To maximize the fiber-stretching effect caused by the radial oscillations of the actuator, the fiber is wound and set as tightly as possible around the actuator. The piezo is driven at easily achievable frequencies (tens of kHz) and voltages ($\leq$12 V peak-to-peak), stretching the fiber ~ 0.3 μm/V at non-resonant frequencies, and thus varying the phases of the different modes. As noted below, the effect is enhanced near the mechanical resonance frequencies of the piezo-fiber assembly. The lowest strong resonance of our assembly is at about 30kHz.

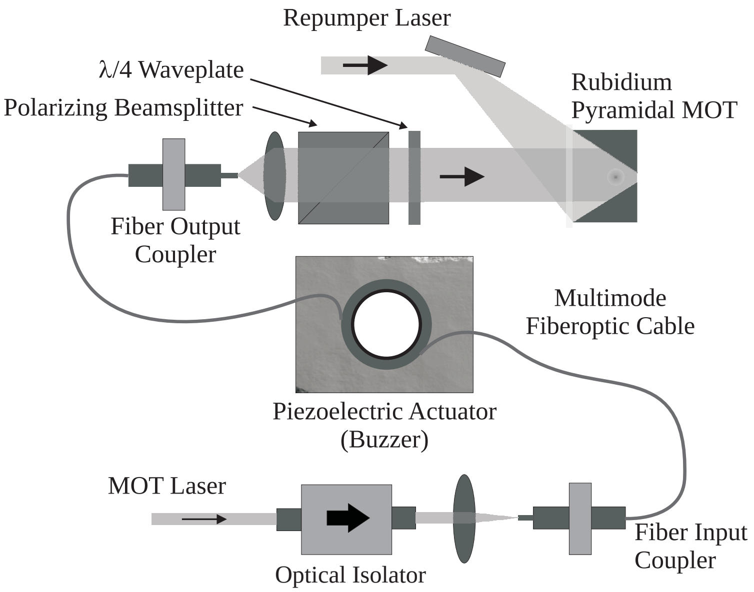

Figure A.1: Experimental setup. The MOT laser beam is passed through an optical isolator and coupled into a multi-mode fiber. The speckle pattern in the multi-mode fiber output is randomized using a piezoelectric actuator. The fiber output beam is circularly polarized and used for a pyramidal MOT. A repumper beam recovers Rb atoms otherwise lost from the cycling transition.

The piezo and the fiber were used to operate a ^{87}Rb pyramidal MOT,[29] as shown in Fig. A.1. The MOT ECDL was detuned to the red of the cooling transition $5S_{1/2}, F = 2 \rightarrow 5P_{3/2}, F' = 3$ (wavelength λ=780 nm, decay rate $\Gamma = 2\pi \times 6$ MHz). After passing through an optical isolator to suppress feedback caused by reflection from the optical fiber, the laser beam was coupled through a multi-mode fiber (78% fiber coupling efficiency; maximal output power 27 mW). As explained above, the phases of the multiple-mode beam emerging from the fiber were differentially modulated by the piezoelectric element. Since the multi-mode fiber randomizes the polarization of the beam, the beam coupled out from the fiber was passed through a polarizing beam splitter. One of the polarized beams was passed through a $\lambda/4$-waveplate and used to generate the (single) circularly polarized beam for the pyramidal MOT.

With this setup, we utilized only half of the fiber output power after linear polarization. After this reduction, the beam still had an average intensity of 3.4mW/cm^2

at the trap center. In MOT configurations employing multiple beams, such as the standard MOT configuration with three retro-reflected beams, both polarized beams emerging from the polarizing beam splitter could be used. A repumping laser tuned on the $5S_{1/2}, F = 1 \rightarrow 5P_{3/2}, F' = 2$ transition was used to recycle atoms from the $5S_{1/2}, F = 1$ level back into the cooling cycle.

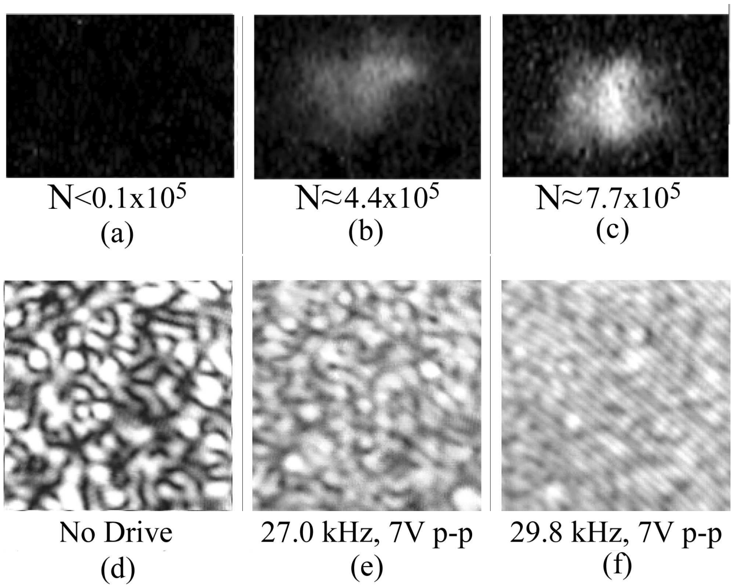

Figure A.2: These images demonstrate the correlation between MOT fluorescence(a-c) and the contrast in the corresponding time-averaged speckle pattern (d-f). The speckle patterns are displayed on identical linear scales with black corresponding to zero intensity. The atom populations N and piezo drive parameters are indicated. The MOT images show a total area of 1.5 mm×1.1 mm to scale, while the speckle patterns show a 4.7 mm ×4.7 mm cross section. The lines in some of the speckle patterns are due to interference in the CCD camera.

In order to characterize the performance of the technique, the atom population in the MOT and images of the time-averaged speckle pattern were obtained for various piezo driving parameters. The population of atoms in the MOT was determined by measuring the fluorescence from the trapped atoms with a photodiode. A background measurement, acquired with the MOT magnetic coils off, was subtracted from the fluorescence measurement to reveal the difference current ΔI_{PD}. The population, N, in the case of a saturated transition, is evaluated as

$$N = \frac{4\pi}{\Delta\Omega} \; \frac{2}{|e|\eta_{\mathrm{PD}}\Gamma} \Delta I_{\mathrm{PD}} \ ,$$

where $\Delta\Omega$ is the solid angle subtended by the detector, η_{PD} the detector efficiency, and e the electron charge. In our experiment, this equation yields a lower estimate on the atom number because the MOT beams do not entirely saturate the cooling transition. The actual atom numbers could be systematically higher than the ones quoted in Sec. A.4 and in Figs. A.2, A.3, and A.4 by a factor of up to about two. The values of N were evaluated in context with the contrast of the speckle pattern in the (time-averaged) MOT beam profile, which was recorded by guiding the beam directly onto a CCD camera. A comparison of MOT beam profiles with snapshots of the associated atom clouds is shown in Fig. A.2. While no atoms could be trapped using a high-contrast time-averaged speckle pattern, as seen in Figs. A.2a and 2d, the MOT is progressively more effective when the time-averaged speckle contrast of the MOT beams is reduced (Figs. A.2b, A.2e and Figs. A.2c, A.2f). This is the essence of the technique.

A.4 Characterization

The effectiveness of the trap was examined as a function of the driving voltage and frequency. The piezoelectric element was driven with frequencies ranging from 0 to 40 kHz and amplitudes from 0 to 12 V peak-to-peak. Speckle images $I(\mathbf{r})$ such as the ones shown in Figs. A.2(d-f) are characterized with the autocorrelation function $S_{\mathrm{2D}}(\Delta\mathbf{r})$,

$$S_{\mathrm{2D}}\left(\Delta\mathbf{r}\right) = A \int_{\mathrm{image}} I\left(\mathbf{r} - \Delta\mathbf{r}\right) I\left(\mathbf{r}\right) \, d\mathbf{r} \ ,$$

where A is a normalizing factor. The function S_{2D}, defined on the two-dimensional $\Delta\mathbf{r}$-plane, is then reduced into a radial function $S\left(|\Delta\mathbf{r}|\right)$ by averaging over the azimuthal angle of $\Delta\mathbf{r}$. The contrast C of the original speckle pattern $I(\mathbf{r})$ is defined as $C = (S_{\max} - S_{\min})/S_{\max}$, where the values $S_{\max}$ and $S_{\min}$ are obtained from $S(|\Delta\mathbf{r}|)$, as indicated in Fig. A.3a. The contrast C of the time-averaged intensity of the trapping beam is shown as a function of the driving parameters in Fig. A.3b. As expected, C generally decreases with increasing driving voltage. Mechanical resonances of the piezo assembly lead to particularly low contrast (30 kHz in Fig. A.3b). As we find in the following, the contrast C of a time-averaged beam is an approximate benchmark for the MOT performance that one can expect to obtain with that beam.

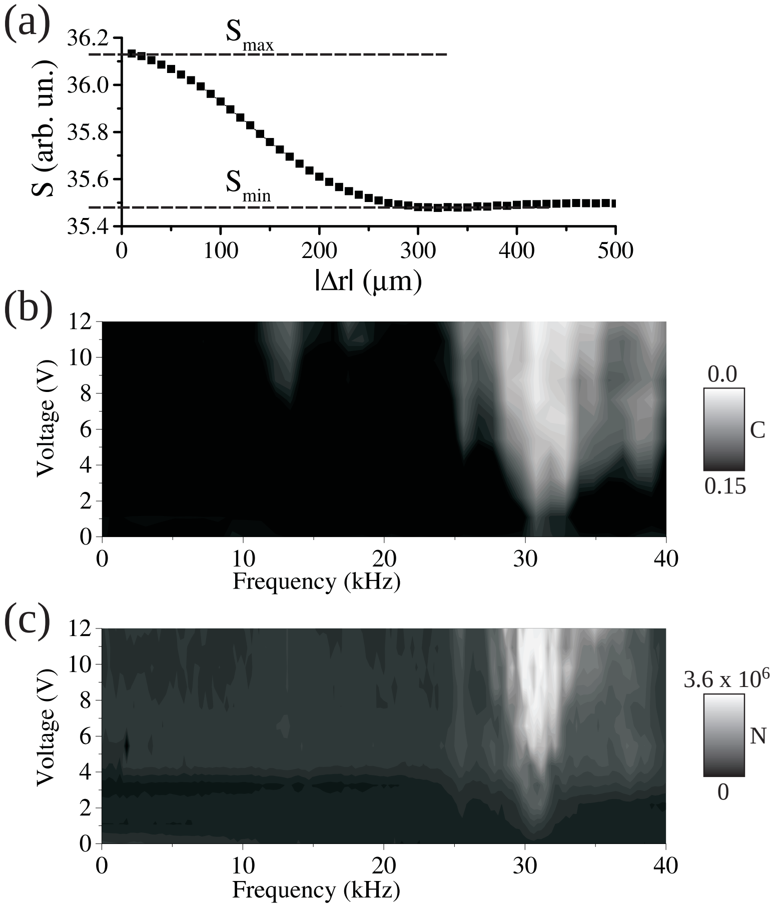

Figure A.3: Contrast and MOT population as a function of the piezo driving parameters. (a) Typical radial autocorrelation function S of a speckle pattern. The extracted quantities $S_{\max}$ and $S_{\min}$ are used to calculate the speckle contrast $C = (S_{\max}\text{-}S_{\min})/S_{\max}$. (b) Linear grayscale representation of the contrast C versus driving voltage and frequency. Contrast values $C > 0.12$ (black) correspond to speckle patterns with nearly 100% intensity modulation. (c) MOT population N versus driving voltage and frequency using the indicated linear grayscale representation.

The population of atoms N in the MOT is shown as a function of the piezo driving parameters in Fig. A.3c. A comparison of Fig. A.3b and Fig. A.3c shows that the efficiency of the MOT largely reflects the contrast C of the beam. As expected, when the amplitude of the driving voltage approaches zero (*i.e.* no time-varying mode phases), C is maximal and the MOT is not tenable. No atoms are trapped in the high-contrast speckle. At higher driving voltages and lower speckle contrast, the MOT is effective and atoms are trapped. In our setup, sufficient loss of contrast was mostly achieved near the mechanical resonances of the piezo-fiber assembly ($\approx$30 kHz in Fig. A.2 and Fig. A.3a; $\approx$ 25 kHz in Fig. A.3b).

A low contrast C is a strong indicator for high MOT performance. This is shown in Fig. A.4, where the atom population N is plotted versus C for two separate measurements. There are wide parameter regions in which robust and predictable MOTs are achieved. There is an exception where the simple relationship between C and N breaks down. In the measurement shown in Fig. A.4b (performed with an different piezo-fiber assembly than for Fig. A.4a), no atoms were trapped when large voltages were applied at the mechanical resonance frequency. This "overdriving" effect indicates that excessive phase variation can be detrimental to the performance of the MOT. Further investigation will be required to clarify the physical mechanism underlying this mode of trap failure.

It is of interest to compare the performance of a MOT operated with a modulated piezo-fiber assembly with one that is formed using a single-mode fiber. Using the modulated multi-mode fiber, we achieved a maximum of 3.6×10^6 trapped atoms with a statistical uncertainty of 0.4×10^6. A comparison experiment using a single mode fiber with a comparable beam diameter and power yielded a population of 6.8×10^6 atoms with a statistical uncertainty of 1×10^6. The factor of two difference

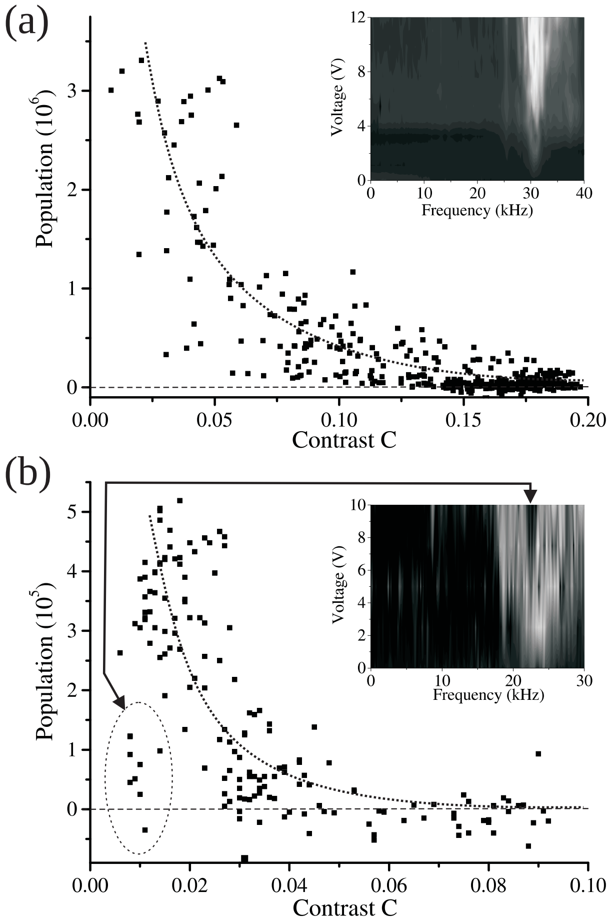

Figure A.4: MOT population N versus speckle contrast C for two experiments with different fiber modulators. The curves drawn through the data represent the general trends. The insets show the MOT populations represented as in Fig. A.3(c). The data points inside the ellipse in panel (b) correspond to the "overdriving" region (as indicated by an arrow). The population measurements have statistical uncertainties of $\pm 3 \times 10^5$ in panel (a) and $\pm 5 \times 10^4$ in panel (b).

may be due to differences in the details of the respective beam profiles. It was, for instance, the case that the spatial modes of the multi-mode fiber outputs were close to a flat-top distribution, while the mode of the single-mode fiber had a Gaussian distribution. Since both MOT beams had the same power (at the trap location), the single-mode beam had a higher central intensity than the multi-mode beam. A larger central intensity is expected to lead to more trapped atoms as well as more photon scattering per given atom. Both effects will lead to higher estimates of the atom number for the case of the single mode fiber.

A mixed multi-mode beam can be advantageous despite the apparent moderate degradation in MOT performance noted in this report. Although a single-mode beam will usually out-perform a multi-mode beam of the same power, it is often much cheaper and easier to find high-power multi-mode diodes, such as BALs, than single-mode diodes with the same power. Using the technique described in this work, a large percentage of the power from the multi-mode diodes could be harnessed with a multi-mode fiber; this would not be possible using a single-mode fiber because of the low coupling efficiency of multi-mode light into single-mode fibers. Mode-mixing techniques, such as the presented method, appear to be the only viable option to utilize high-power multi-mode light for laser cooling.

Further, it may be noted that the overall beam propagation properties of multi-mode fiber output are worse than those of single-mode fiber output because of respective differences in their optical invariants (fiber core diameter × angular spread). However, this is not a significant issue since MOTs are known to be robust with respect to small variations of the beam direction.

A.5 Conclusion

We have demonstrated in this proof-of-principle experiment that the output of multi-mode optical fibers can be used for applications demanding evenly distributed light such as laser cooling. By randomizing the differential phases of the fiber modes on time scales faster than the center-of-mass response time of the atoms, the speckle pattern in the fiber output beam can be "smoothed" to provide effective laser-cooling and trapping beams. The contrast of the time-averaged output beam is found to be a strong predictor of the effectiveness of the beam for magneto-optic atom trapping. There are other methods of time averaging of multi-mode fiber output. In addition to the scheme presented, we have been able to realize a MOT by vibrating the output end of the multi-mode fiber in free space. It should be possible to extend the time-averaging technique to other laser cooling and trapping applications which do not require instantaneous spatial smoothness, such as Zeeman slowers and dipole traps. The scheme, particularly when used in conjunction with BALs, could significantly increase the efficiency of many laser cooling and trapping experiments.

APPENDIX B

PID Feedback Control for Parallel Gridless DSMC

As the atom guide collision modeling code was developed, it was quickly realized that the computational load on a single processor was too burdensome. Early simulations, for example, took well over a month of wall-clock time, to even approach steady state. This is not a very helpful situation for needing simulation results to guide the experimental design. The primary method explored for decreasing the simulation runtime was that of parallel processing. It is widely used practice to divide a computational problem into smaller chunks which can then be spread out across a group of processors, each of which are then able to quickly return the results of their small bit of work. It is in this manner, that huge computational jobs are done, such as simulations for the space shuttle [86] and other satalites [87].

There are two main ingredients to implementing a code to efficiently run in a parallel environment. The first of these is the evenness of the distribution of the workload throughout each of the computational nodes, or CPUs. If one CPU is given a larger amount of work to do that many others, the simulation will have wasted time on each of the less used CPUs. In other words, the runtime will not be greatly improved because each of the other processors waiting on the one. The second ingredient to performing efficient parallel work is optimized, or rather minimized communication that must happen between processors. While a single (shared-memory) machine can easily move data around using very fast buses, a distributed machine must communicate via network protocols and wiring and is thus limited by network bandwidth. In the following sections, we will describe our method to include these two ingredients into the gridless atom guide code. It should also be noted that this parallel code was built using a parallel API known as MPI.

B.1 Parallel processing with Gridless DSMC

For simplicity, a system is assumed that can easily be divided into sections along only one dimension. For the sake of the atom guide experiment, this is a valid assumption along the direction of the main atomic flow. The computational space of the simulation is thus divided up into small regions along the longitudinal direction, each of which are then assigned to a single processor, as demonstrated by Fig. B.1.

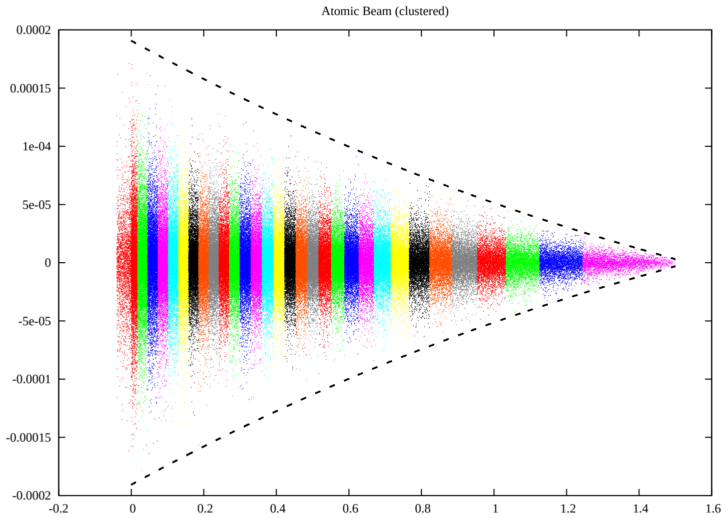

Figure B.1: The atomic beam in the simulation is divvied to different processors to balance the work load on each of the processors. The different colors in this figure represent particles that are simulated on various processors.

Because of the disconnect of the gridless DSMC algorithm to the geometry of the system, it is relatively easy to wrap a parallel management code around the existing DSMC code. In other words, each processor runs almost independently of the others, communicating needed information only at the end of each time step. Using the boundary mechanism, described in Sec. V.5.2.3.4, virtual boundaries are installed within each DSMC instance to represent the boundary between the domains of the CPUs. Particles that cross these boundaries during the move operation, are subsequently shuffled (via network communication) to the proper computational domain at the end of the time step. By ensuring that the length of any one computational domain, L, satisfies L $\gg \left(v_\parallel \Delta t\right)_{\mathrm{max}}$, the shuffling is limited to nearest neighbor communication. This simplifies the implementation and allows network traffic to be limited (as many neighboring nodes are often on the separate CPUs of the same dual processor machine). In addition, this allows a load balancing technique as describe later in Sec. B.1.2.

B.1.1 Domain Decomposition

Domain decomposition is the process by which the simulation space is divided up between processors. It is possible to use information of the whole distribution of the work in the system to divide properly and end up with a nicely distributed work load per CPU. Although the results of this process can be very good, the process itself is very intensive. For our parallel code, domain decomposition is therefore only used to initialize the work load for a group of processors. Small changes in each of the domains are then managed by a load balancing code, as described below.

As an illustration of our parallel code, consider a simple gas expansion problem: a thermal gas with a positive average velocity in one direction ($\langle v_\parallel \rangle = 1$ m/s) is allowed to freely expand. The domain decomposition is done in the direction of this non-zero velocity component. A minimum particles per CPU is specified such that only one CPU is allowed at $t = 0$, as shown at the first domain decomposition in Fig. B.2. (Fig. B.2 shows the assigned domains whereas Fig. B.4 shows the actual computational volume occupied by the simulated particles in each domain.) At approximately $t \approx 25$ ms, enough particles are in the simulation such that an additional processor can be added. The domain at $t \approx 25$ ms is evenly divided between the two active processors. The simulation then continues until the total particle count in the system can support yet another processor at $t \approx 35$ ms.

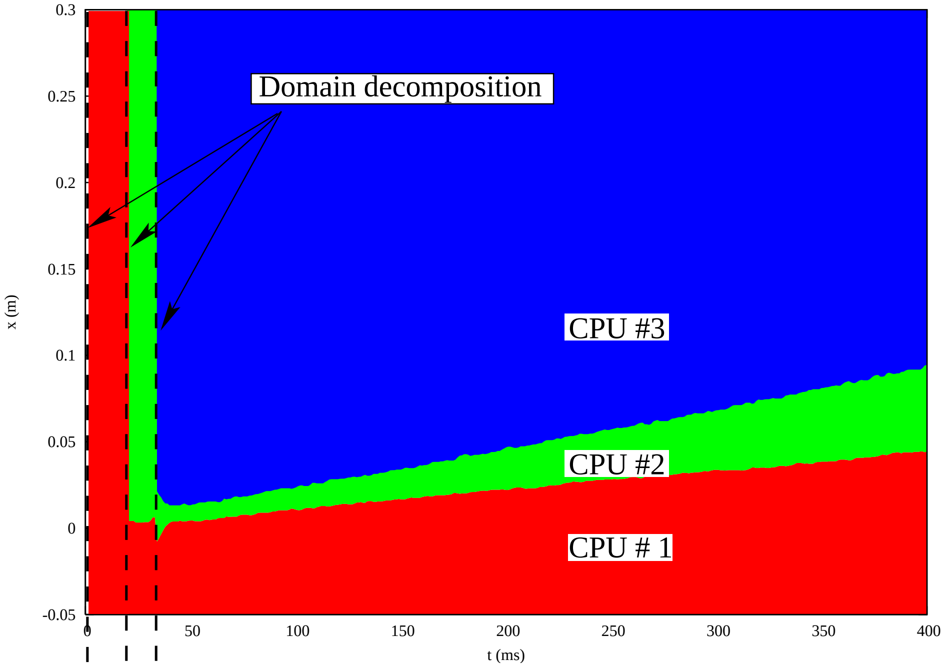

Figure B.2: The computational domain is divided up into sections which are assigned to specific processors. After global domain decomposition takes place, local shifts of CPU boundaries occur in order to perform locally controlled load balancing.

Currently, the code does not do anything beyond a linear re-distribution of the computational domain. The inefficiency of this simple method will become apparent when we discuss the results of the load balancing algorithm.

B.1.2 Load Balancing

The first attempt to load balance a parallel calculation could be to manually divide the work into approximately equally difficult portions. Though this may be the easiest approach, the results can hardly produce the best use of computational resources if the simulated system is dynamic, such as during the start-up phase of the atom guide. In light of the domain decomposition described in the previous section, this would be equivalent to keeping the domains statically allocated between domain decomposition events. One could even trigger additional decomposition events periodically to readjust the workload distribution. On the other hand, a method of realigning the domain boundaries during each time step could allow for the work load to continue to be evenly distributed across the active processors.

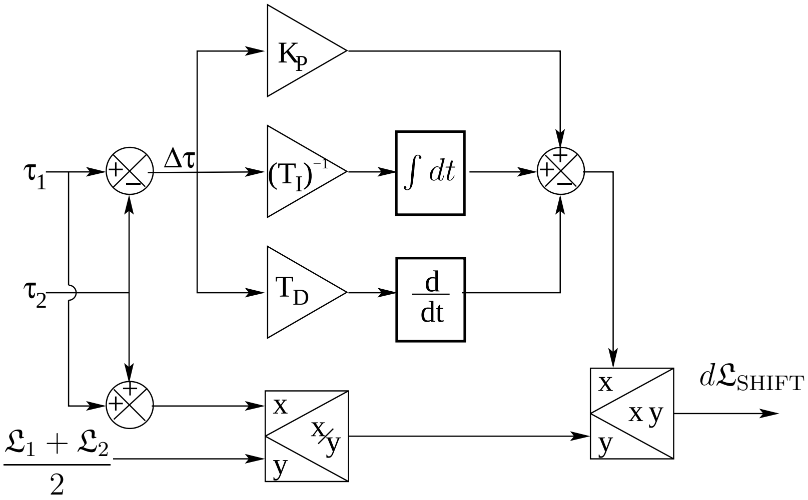

Figure B.3: A feedback control diagram describing the load balancing algorithm. The error signal is $\Delta\tau = \tau_1 - \tau_2$, where τ_1 and τ_2 are the computational times recorded on CPU 1 and 2 respectively. $\Delta\tau$ is used to derive a relative shift, $d\mathrm{L}_{\mathrm{SHIFT}}$, in the common boundary between CPU 1 and 2. CPU 1 and 2 then move the respective boundary by an amount $\pm d\mathrm{L}_{\mathrm{SHIFT}}$.

To provide for dynamic domain realignment, we resort to feedback control often used in electronic locking systems. A schematic for our control loop is shown in Fig. B.3. It is implicit in this process, that only two neighboring nodes communicate for a given realignment. We will denote these two nodes as CPU 1 and CPU 2. The error signal is defined as the difference between the computational times τ_1 and τ_2 as measured on CPU 1 and 2 respectively. Using a proportional, integral, and differential gain control (PID), a shift in the location of the common boundary, $d\mathrm{L}_{\mathrm{SHIFT}}$, is derived. Typically, PID control circuits need be optimized for each individual application. Likewise, it can be expected that the application of the PID to parallel processing will need to be tweaked for each type of simulation (type is defined by the combination of physical system, number of particles, number of CPUs, etc.). In addition, badly tuned PID circuits can result in wild oscillations that are detrimental to the efficacy of the parallel system. To avoid this, our simulated PID is usually tuned very weak, such that the settling time is much longer than for the optimized case. In practice, this means that a non-optimized domain decomposition to requires a significant time to become optimized. Typical values of our control parameters are $\mathrm{K_P} = 0.4$, $\mathrm{T_I} = 80$, and $\mathrm{T_D} = 1/80$. Following common procedure with the Message Passing Interface (MPI) library, the appropriate information is shared between CPU 1 and 2 such that the complete calculation of the boundary adjustment is done on each of the processors.

To continue the illustration of Sec. B.1.1, between each domain decomposition and after the last, the CPU–CPU boundaries evolve locally to produce an even work load among the active processors.

B.2 Proof in the pudding

As a more practical evaluation of this procedure, Fig. B.5, shows the computational time per CPU required for simulating the atom guide with twenty processors. At the beginning of the simulation, there are no particles and thus only one CPU is active. As more and more particles are added to the system, CPUs are made active and boundaries are allowed to evolve under the load-balancing PID control. The inset in Fig. B.5 shows a closeup of each domain decomposition. Oscillations from the settling time of the algorithm are also visible in this figure. About 0.3 s after the last decomposition, the parallel system evolves in a more smoothly, with the load

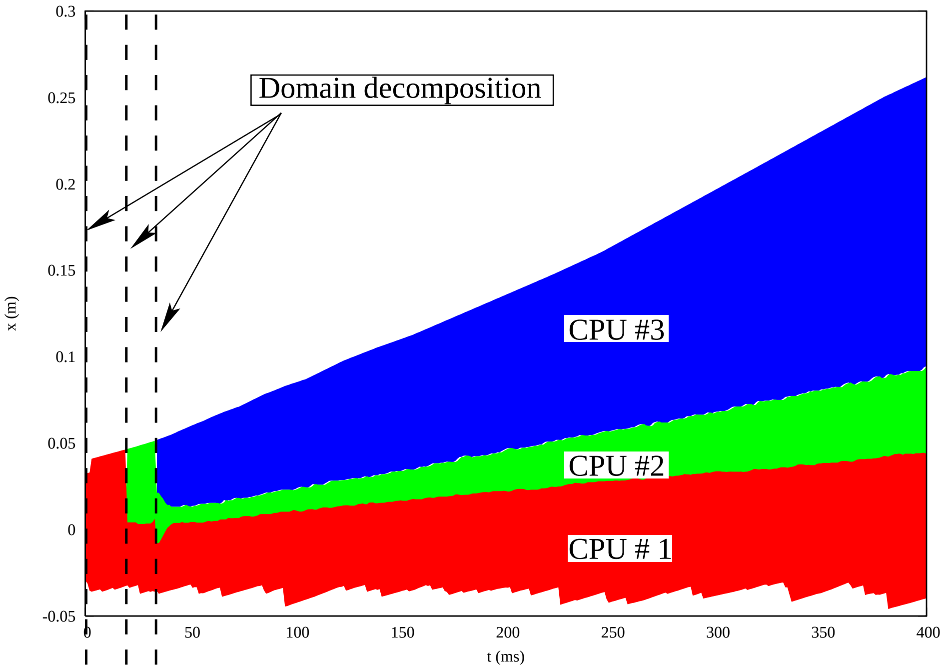

Figure B.4: Actual computational volume occupied by the simulated particles in each domain as a function of simulation time.

properly balanced between each of the twenty processors. Fig. B.6 also shows the particle number per processor. The wide range in particle numbers per CPU reflects the higher computational load for regions where collisions play a larger role as well as the integrator requiring more calculations due to higher field gradients.

B.3 Improvements

While an even particle redistribution function was easy to implement, the start-up noise could be dramatically decreased by using a smarter redistribution function. One such possible redistribution algorithm could first create a polynomial that represents a work-load distribution in the direction of the domain decomposition. This polynomial would be based upon, and pass through the values at each previously active node. Using this smooth polynomial, it would be possible to create a new nodal distribution such that the expected work per node is approximately even across all

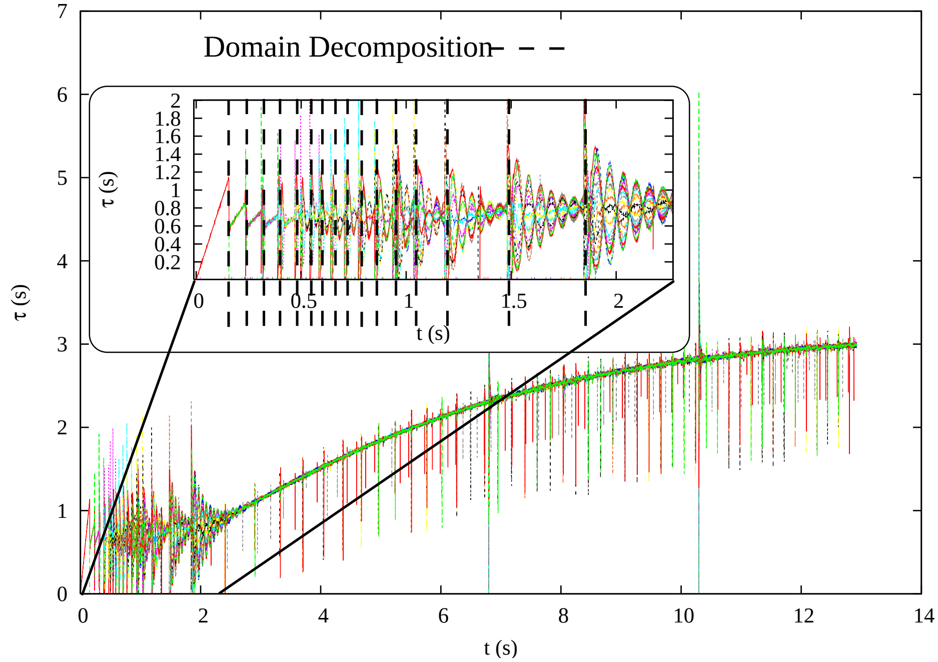

Figure B.5: Computational time per CPU for a 20 processor simulation.

newly activated nodes.

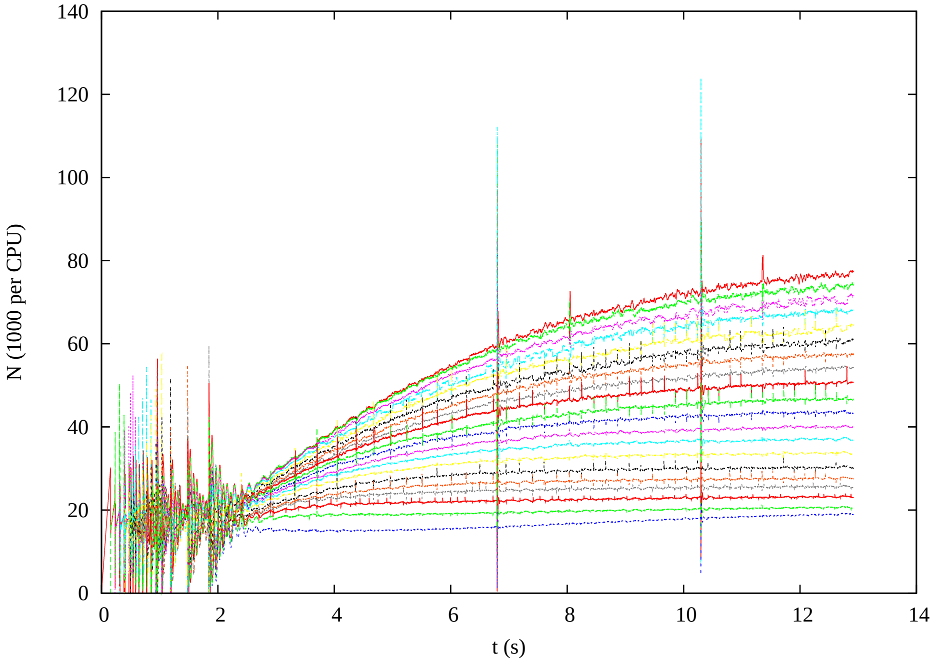

Figure B.6: Number of particles assigned to each of 20 processors.

BIBLIOGRAPHY

BIBLIOGRAPHY

[1] H. G. Dehmelt. Radio-frequency spectroscopy of stored ions. i. storage. *Adv. At. Mol. Opt. Phys.*, 3:53, 1967.

[2] C. E. Wieman, D. E. Pritchard, and D. J. Wineland. Atom cooling, trapping, and quantum manipulation. *Rev. Mod. Phys.*, 71:S253, 1999.

[3] W. D. Phillips, P. L. Gould, and P. D. Lett. Cooling, stopping, and trapping atoms. *Science*, 239(4842):877 – 83, 1988/02/19. ISSN 0036-8075.

[4] J. M. Doyle and B. Friedrich. Molecules are cool. *Nature*, 401:750–751, October 1999.

[5] J. Doyle, B. Friedrich, R. V. Krems, and F. Masnou-Seeuws. Quo vadis, cold molecules? *Euro. Phys. J. D*, 31:149–164, 2004. doi: 10.1140/epjd/e2004-00151-x .

[6] K. B. Davis, M.-O. Mewes, M. R. Andrews, N. J. van Druten, D. S. Durfee, D. M. Kurn, and W. Ketterle. Bose-Einstein condensation in a gas of sodium atoms. *Phys. Rev. Lett.*, 75(22): 3969, November 1995.

[7] M. H. Anderson, J. R. Ensher, M. R. Matthews, C. E. Wieman, and E. A. Cornell. Observation of Bose-Einstein condensation in a dilute atomic vapor. *Science*, 269(0):198, July 1995.

[8] C. C. Bradley, C. A. Sackett, J. J. Tollett, and R. G. Hulet. Evidence of Bose-Einstein condensation in an atomic gas with attractive interactions. *Phys. Rev. Lett.*, 75(9):1687, August 1995. *ibid.* **79**, 1170 (1997).

[9] W. Ketterle. RLE Currents **9**. Technical Report 1 (Spring 1997), Research Laboratory of Electronics at Massachusetts Institute of Technology, 1997.

[10] C. W. Gardiner, P. Zoller, R. J. Ballagh, and M. J. Davis. Kinetics of bose-einstein condensation in a trap. *Phys. Rev. Lett.*, 79:1793–1796, September 1997. doi: 10.1103/PhysRevLett.79.1793 .

[11] D. Kleppner. A beginner's guide to the atom laser. *Phys. Today*, 50:11–13, August 1997.

[12] H.-J. Miesner, D. M. Stamper-Kurn, M. R. Andrews, D. S. Durfee, S. Inouye, and W. Ketterle. Bosonic stimulation in the formation of a bose-einstein condensate. *Science*, 279:1005–+, February 1998.

[13] M.-O. Mewes, M. R. Andrews, D. M. Kurn, D. S. Durfee, C. G. Townsend, and W. Ketterle. Output coupler for Bose-Einstein condensed atoms. *Phys. Rev. Lett.*, 78(4):582, January 1997.

[14] I. Bloch, T. W. Hänsch, and T. Esslinger. Atom laser with a cw output coupler. *Physical Review Letters*, 82:3008–3011, April 1999. doi: 10.1103/PhysRevLett.82.3008 .

[15] E. W. Hagley, L. Deng, M. Kozuma, J. Wen, K. Helmerson, S. L. Rolston, and W. D. Phillips. A well-collimated quasi-continuous atom laser. *Science*, 283:1706–+, March 1999.

[16] Y. Shin, M. Saba, T. A. Pasquini, W. Ketterle, D. E. Pritchard, and A. E. Leanhardt. Atom interferometry with bose-einstein condensates in a double-well potential. *Physical Review Letters*, 92(5):050405–+, February 2004. doi: 10.1103/PhysRevLett.92.050405 .

[17] Y.-J. Wang, D. Z. Anderson, V. M. Bright, E. A. Cornell, Q. Diot, T. Kishimoto, M. Prentiss, R. A. Saravanan, S. R. Segal, and S. Wu. Atom michelson interferometer on a chip using a bose-einstein condensate. *Phys. Rev. Lett.*, 94(9):090405–+, March 2005. doi: 10.1103/PhysRevLett.94.090405 .

[18] Sebastian Fray, Cristina Alvarez Diez, Theodor W. Hansch, and Martin Weitz. Atomic interferometer with amplitude gratings of light and its applications to atom based tests of the equivalence principle. *Physical Review Letters*, 93(24):240404, 2004. doi: 10.1103/PhysRevLett.93.240404 .

[19] O. Garcia, B. Deissler, K. J. Hughes, J. M. Reeves, and C. A. Sackett. A condensate interferometer with long coherence time and large arm separation. *ArXiv Condensed Matter e-prints*, March 2006.

[20] J. Williams, R. Walser, C. Wieman, J. Cooper, and M. Holland. Achieving steady-state Bose-Einstein condensation. *Phys. Rev. A*, 57(3):2030, March 1998.

[21] Z. T. Lu, K. L. Corwin, M. J. Renn, M. H. Anderson, E. A. Cornell, and C. E. Wieman. Low-velocity intense source of atoms from a magneto-optical trap. *Phys. Rev. Lett.*, 77(16): 3331, October 1996.

[22] R. S. Williamson III, P. A. Voytas, R. T. Newell, and T Walker. A magneto-optical trap loaded from a pyramidal funnel. *Opt. Exp.*, 3(3):111–117, August 1998.

[23] D. E. Pritchard. Cooling neutral atoms in a magnetic trap for precision spectroscopy. *Phys. Rev. Lett.*, 51:1336–1339, October 1983. doi: 10.1103/PhysRevLett.51.1336 .

[24] A. L. Migdall, J. V. Prodan, W. D. Phillips, T. H. Bergeman, and H. J. Metcalf. First observation of magnetically trapped neutral atoms. *Phys. Rev. Lett.*, 54(24):2596 – 9, June 1985. ISSN 0031-9007. doi: 10.1103/PhysRevLett.54.2596 .

[25] J.-H. Choi, J. R. Guest, A. P. Povilus, E. Hansis, and G. Raithel. Magnetic trapping of long-lived cold rydberg atoms. *Phys. Rev. Lett.*, 95(24):243001–+, December 2005. doi: 10.1103/PhysRevLett.95.243001 .

[26] Marc-Oliver Mewes. *Bose-Einstein Condensation of Sodium Atoms.* PhD thesis, Massachusetts Institute of Technology, 1997.

[27] W. Ketterle and N. J. Van Druten. Evaporative cooling of trapped atoms. *Adv. At. Mol. Opt. Phys.*, 37:181, 1996.

[28] Harold J. Metcalf and Peter van der Straten. *Laser Cooling and Trapping.* Springer-Verlag New York, Inc., 1999.

[29] K. I. Lee, J. A. Kim, H. R. Noh, and W. Jhe. Single-beam atom trap in a pyramidal and conical hollow mirror. *Opt. Lett.*, 21(15):1177–1179, August 1996.

[30] E. L. Raab, M. Prentiss, Alex Cable, Steven Chu, and D. E. Pritchard. Trapping of neutral sodium atoms with radiation pressure. *Phys. Rev. Lett.*, 59(23):2631–2634, December 1987.

[31] P. Cren, C. F. Roos, A. Aclan, J. Dalibard, and D. Guéry-Odelin. Loading of a cold atomic beam into a magnetic guide. *Euro. Phys. J. D*, 20:107–116, July 2002. doi: 10.1140/epjd/e2002-00106-3 .

[32] C. F. Roos, P. Cren, T. Lahaye, J. Dalibard, and D. Guéry-Odelin. Injection of a cold atomic beam into a magnetic guide. *Laser Physics*, 13(4):605, July 2003. URL `http://www.phys.ens.fr/~dgo/0212147.pdf`.

[33] S. Weyers, E. Aucouturier, C. Valentin, and N. Dimarcq. A continuous beam of cold cesium atoms extracted from a two-dimensional magneto-optical trap. *Opt. Comm.*, 143:30, 1997.

[34] K. Dieckmann, R. J. C. Spreeuw, M. Weidemüller, and J. T. M. Walraven. Two-dimensional magneto-optical trap as a source of slow atoms. *Phys. Rev. A*, 58:3891, 1998.

[35] P. Berthoud, A. Joyet, G. Dudle, N. Sagna, and P. Thomann. A continuous beam of slow, cold cesium atoms magnetically extracted from a 2d magneto-optical trap. *Europhys. Lett.*, 41(2): 141, 1998.

[36] P. Berthoud, E. Fretel, and P. Thomann. Bright, slow, and continuous beam of laser-cooled cesium atoms. *Phys. Rev. A*, 60:R4241, 1999.

[37] J. Schoser, A. Batär, R. Löw, V. Schweikhard, A. Grabowski, Yu. B. Ovchinnikov, and T. Pfau. Intense source of cold rb atoms from a pure two-dimensional magneto-optical trap. *Phys. Rev. A*, 66(023410), 2002.

[38] B. K. Teo, T. Cubel, and G. Raithel. A slow and dark atom beam. *Opt. Comm.*, 212:307–315, 2002. doi: 10.1016/S0030-4018(02)02001-1 .

[39] B. K. Teo and G. Raithel. Loading mechanism for atomic guides. *Phys. Rev. A*, 63:031402(R), 2001. doi: 10.1103/PhysRevA.63.031402 .

[40] B. K. Teo and G. Raithel. Atom reflection in a tapered magnetic guide. *Phys. Rev. A*, 65(5): 051401–+, May 2002. doi: 10.1103/PhysRevA.65.051401 .

[41] T. Lahaye, Z. Wang, G. Reinaudi, S. P. Rath, J. Dalibard, and D. Guéry-Odelin. Evaporative cooling of a guided rubidium atomic beam. *Phys. Rev. A*, 72(033411):33411 − 1, September 2005. ISSN 1050-2947. doi: 10.1103/PhysRevA.72.033411 .

[42] M. Fauquembergue, J-F. Riou, W. Guerin, S. Rangwala, F. Moron, A. Villing, Y. Le Coq, P. Bouyer, and A. Aspect. Partially ferromagnetic eletromagnet for trapping and cooling neutral atoms to quantum degerneracy. *preprint, arXiv:cond-mat/0507129 v2*, July 2005.

[43] M. Vengalattore, R. S. Conroy, W. Rooijakkers, and M. Prentiss. Ferromagnets for integrated atom optics. *J. Appl. Phys.*, 95(8):4404–7, April 2004.

[44] W. Hänsel, J. Reichel, P. Hommelhoff, and T. W. Hänsch. Magnetic conveyor belt for transporting and merging trapped atom clouds. *Phys. Rev. Lett.*, 86(4):608, January 2001. doi: 10.1103/PhysRevLett.86.608 .

[45] Spencer E. Olson, Rahul R. Mhaskar, and Georg Raithel. Continuous propagation and energy filtering of a cold atomic beam in a long high-gradient magnetic atom guide. *Phys. Rev. A*, 73 (3):033622, March 2006. doi: 10.1103/PhysRevA.73.033622 .

[46] P. O. Schmidt, S. Hensler, J. Werner, T. Binhammer, A. Görlitz, and T. Pfau. Continuous loading of cold atoms into a ioffe-pritchard magnetic trap. *J. Opt. B*, 5:170–+, April 2003.

[47] K. E. Gibble, S. Kasapi, and S. Chu. Improved magneto-optic trapping in a vapor cell. *Opt. Lett.*, 17:526–528, April 1992.

[48] Johannes Schuster. *Stolawinen in einem Bose-Einstein-Kondensat.* PhD thesis, Universität Konstanz, 2002.

[49] R. Dum, P. Zoller, and H. Ritsch. Monte carlo simulation of the atomic master equation for spontaneous emission. *Phys. Rev. A*, 45:4879–4887, April 1992. doi: 10.1103/PhysRevA.45.4879 .

[50] R. R. Mhaskar, S. E. Olson, and G. Raithel. Open-channel fluorescence imaging of atoms in high-gradient magnetic fields. *Euro. Phys. J. D*, 41:221–227, February 2007. doi: 10.1140/epjd/e2006-00242-8 .

[51] T. Lahaye, J. M. Vogels, K. J. Günter, Z. Wang, J. Dalibard, and D. Guéry-Odelin. Realization of a magnetically guided atomic beam in the collisional regime. *Phys. Rev. Lett.*, 93(093003), August 2004. doi: 10.1103/PhysRevLett.93.093003 .

[52] G. A. Bird. *Molecular Gas Dynamics and the Direct Simulation of Gas Flows.* Oxford University Press, 1994.

[53] Josh Barnes and Piet Hut. A hierarchical $O(N \log[N])$ force-calculation algorithm. *Nature*, 324:446–449, December 1986. doi: 10.1038/324446a0 . URL `http://www.nature.com/nature/journal/v324/n6096/pdf/324446a0.pdf`.

[54] V. Springel, N. Yoshida, and S. D. M. White. GADGET: a code for collisionless and gasdynamical cosmological simulations. *New Astronomy*, 6:79–117, April 2001. doi: 10.1016/S1384-1076(01)00042-2 .

[55] Andrew J. Christlieb, R. Krasny, and J. P. Verboncoeur. A treecode algorithm for simulating electron dynamics in a penning-malmberg trap. *Comp. Phys. Comm.*, 164(1-3):306–310, December 2004. doi: 10.1016/j.cpc.2004.06.076 .

[56] G. A. Bird. Approach to translational equilibrium in a rigid sphere gas. *Phys. Fluids*, 6:1518, 1963.

[57] A. L. Garcia, J. B. Bell, W. Y. Crutchfield, and B. J. Alder. Adaptive mesh and algorithm refinement using direct simulation monte carlo. *J. Comp. Phys.*, 154:134–155, September 1999.

[58] J.-S. Wu, K.-C. Tseng, and F.-Y. Wu. Parallel three-dimensional dsmc method using mesh refinement and variable time-step scheme. *Comp. Phys. Comm.*, 162:166–187, October 2004. doi: 10.1016/j.cpc.2004.07.004 .

[59] Philippe Lacroute and Marc Levoy. Fast volume rendering using a shear-warp factorization of the viewing transformation. In *SIGGRAPH '94: Proceedings of the 21st annual conference on Computer graphics and interactive techniques*, pages 451–458, New York, NY, USA, 1994. ACM Press. ISBN 0-89791-667-0. doi: 10.1145/192161.192283 .

[60] Matthew Moore and Jane Wilhelms. Collision detection and response for computer animationr3. In *SIGGRAPH '88: Proceedings of the 15th annual conference on Computer graphics and interactive techniques*, pages 289–298, New York, NY, USA, 1988. ACM Press. ISBN 0-89791-275-6. doi: 10.1145/54852.378528 .

[61] Robert J. Renka. Algorithm 661: Qshep3d: quadratic shepard method for trivariate interpolation of scattered data. *ACM Trans. Math. Softw.*, 14(2):151–152, 1988. ISSN 0098-3500. doi: 10.1145/45054.214374 .

[62] L. Hernquist and N. Katz. TREESPH - a unification of SPH with the hierarchical tree method. *Astro. J. Supp. Series*, 70:419–446, June 1989.

[63] G. A. Bird. *Molecular Gas Dynamics.* Oxford University Press, 1976.

[64] Quanhua Sun. *Information preservation methods for modeling micro-scale gas flows.* PhD thesis, University of Michigan, 2003.

[65] I. Boyd. private communication, 2005.

[66] A. J. Christlieb. private communication, 2006.

[67] W. Petrich, M. H. Anderson, J. R. Ensher, and E. A. Cornell. Behavior of atoms in a compressed magneto-optical trap. *J. Opt. Soc. Am.*, 11:1332, 1994.

[68] Huang Wu and Christopher J. Foot. Direct simulation of evaporative cooling. *J. Phys. B*, 29: 321, 1996.

[69] E. Mandonnet, A. Minguzzi, R. Dum, I. Carusotto, Y. Castin, and J. Dalibard. Evaporative cooling of an atomic beam. *Euro. Phys. J. D*, 10(1):9–18, March 2000.

[70] T. Lahaye and D. Guéry-Odelin. Discrete-step evaporation of an atomic beam. *Euro. Phys. J. D*, 33:67–75, April 2005. doi: 10.1140/epjd/e2005-00007-y .

[71] D. W. Snoke and J. P. Wolfe. Population dynamics of a bose gas near saturation. *Phys. Rev. B*, 39:4030–4037, March 1989. doi: 10.1103/PhysRevB.39.4030 .

[72] C. R. Monroe, E. A. Cornell, C. A. Sackett, C. J. Myatt, and C. E. Wieman. Measurement of cs-cs elastic scattering at t=30 μk. *Phys. Rev. Lett.*, 70:414–417, January 1993. doi: 10.1103/PhysRevLett.70.414 .

[73] G. Raithel. Bulletin of the Research Corporation, Winter Issue. Technical report, Research Corporation, 1999.

[74] Stephan Wildermuth, Sebastian Hofferberth, Igor Lesanovsky, Elmar Haller, L. Mauritz Andersson, Sönke Groth, Israel Bar-Joseph, Peter Krüger, and Jörg Schmiedmayer. Microscopic magnetic-field imaging. *Nature*, 435:440, May 2005.

[75] J. M. McGuirk, G. T. Foster, J. B. Fixler, M. J. Snadden, and M. A. Kasevich. Sensitive absolute-gravity gradiometry using atom interferometry. *Phys. Rev. A*, 65:033608, February 2002.

[76] T. L. Gustavson, P. Bouyer, and M. A. Kasevich. Precision rotation measurements with an atom interferometer gyroscope. *Phys. Rev. Lett.*, 78(11):2046–2049, March 1997. doi: 10.1103/PhysRevLett.78.2046 .

[77] J. Schmiedmayer, M. S. Chapman, C. R. Ekstorm, T. D. Hammond, S. Wehinger, and D. E. Pritchard. Index of refraction of various gases for sodium matter waves. *Phys. Rev. Lett.*, 74 (7):1043–1047, February 1995.

[78] Y. Shin, C. Spanner, G.-B. Jo, T. A. Pasquini, M. Saba, W. Ketterle, D. E. Pritchard, M. Vengalattore, and M. Prentiss. Interference of bose-einstein condensates on an atom chip. *preprint, arXiv:cond-mat/0506464 v2*, July 2005.

[79] Mark A. Kasevich. Coherence with atoms. *Science*, 298:1363, November 2002.

[80] G. Zabow, R. S. Conroy, and M. G. Prentiss. Coherent matter-wave manipulation in the diabatic limit. *Phys. Rev. Lett.*, 92(18):180404, May 2004.

[81] F. Fatemi, M. Bashkansky, and S. Moore. Side-illuminated hollow-core optical fiber for atom guiding. *Opt. Exp.*, 13:4890–4895, 2005.

[82] A. Andalkar, S. K. Lamoreaux, and R. B. Warrington. Improved external cavity design for cesium d1 (894 nm) diode laser. *Rev. Sci. Instrum.*, 71:4029–4031, 2000.

[83] C. S. Adams and E. Riis. Laser cooling and trapping of neutral atoms. *Prog. Quant. Elec.*, 21 (1):1–79, 1997.

[84] C. E. Wieman and L. Hollberg. Using diode lasers for atomic physics. *Rev. Sci. Instrum.*, 62: 1–6, 1991.

[85] I. Shvarchuck, K. Dieckmann, M. Zielonkowski, and J. T. M. Walraven. Broad-area diode-laser system for a rubidium bose -einstein condensation experiment. *Applied Physics B*, 71:475–480, 2000.

[86] G. A. BIRD. Application of the direct simulation monte carlo method to the full shuttle geometry. In *AIAA and ASME, Joint Thermophysics and Heat Transfer Conference, 5th*, Seattle, WA, USA, June 1990.

[87] A. G. Rault and M. S. Woronowicz. Application of direct simulation monte carlo satelite contamination studies. *J. of Spacecraft and Rockets*, 32:392–97, 1995.

ABSTRACT

Long, High-Gradient Magnetic Atom Guide and Progress Towards an Atom Laser

by

Spencer E. Olson

Chair: Georg A. Raithel

The continuous injection and propagation of a cold atomic beam in a 1.7 m long high-gradient (up to 2.7 kG/cm) magnetic guide is demonstrated. Continuous injection is accomplished by side-loading a magnetic guide with atoms from a sequence of two modified magneto-optical traps. In the high-gradient portion of the guide, the guided atomic beam has a transverse temperature of 420 μK ± 40 μK, a longitudinal temperature of 1 mK, and an average velocity of order 1 m/s.

Essential for the characterization of this steady-state atomic beam, imaging methods compatible with the high field-gradients associated with this magnetic guide have been investigated and developed. By utilizing a probe laser tuned to an open transition, the fluorescence yield per atom is largely fixed throughout the trap volume, independent of the trapping field. This enables a reliable conversion of fluorescence images into atomic-density profiles.

Using a fixed radio-frequency (ν_{rf}) current coupled directly onto the guide wires, continuous and selective removal of atoms with a transverse energy exceeding $h\nu_{\mathrm{rf}}$ is demonstrated. This removal scheme is the essence of an rf filter, where the number of modes occupied by the atomic flow is reduced. Through sufficient rf-filtering, a near-single-mode guided atomic beam should be achievable, enabling basic atom-interferometric experiments. The extension of this fixed-frequency removal of atoms for continuous position-resolved evaporative cooling in a long magnetic guide is outlined.

Employing an innovative gridless technique for performing Direct Simulation of rarefied gas dynamics via Monte Carlo (DSMC), the evaporative cooling process in a guided atomic beam has been simulated. Both fixed-frequency as well as variable-frequency evaporative cooling layouts have been explored and the results of these simulations are presented. The implementation of this gridless technique is presented and its benefits are briefly outlined.

In parallel with the development of a continuous-wave atom laser, tools suited to manipulate cold atomic beams in atom guides have been explored. An atomic guide with a tunable aspect ratio, using rf-dressed state potentials, is presented.